Understanding the Structure and Properties of Self-Assembled Monolayers for Interfacial Patterning

Leslie A. Adamczyk

Dissertation submitted to the faculty of the Virginia Polytechnic Institute and State University in partial fulfillment of the requirements for the degree of

Doctor of Philosophy
In
Chemistry

Mark R. Anderson, Chair
John R. Morris, Co-Chair
Karen J. Brewer
Gary L. Long
James M. Tanko

May 28, 2009

Blacksburg, Virginia

Keywords: Self-Assembled Monolayers, Electrochemistry, Contact Printing, Electrochemical Impedance Spectroscopy, Defects, Patterns

Understanding the Structure and Properties of Self-Assembled Monolayers for Interfacial Patterning

Leslie A. Adamczyk

ABSTRACT

This dissertation describes the impact of defects on monolayer properties for self-assembled monolayers (SAMs) created by interfacial patterning methods. When forming a two-dimensional interfacial pattern with *n*-alkanethiols on gold, the desired electrochemical properties are those of a homogeneous, solution adsorbed monolayer. However, even well-ordered SAMs contain a small degree of defects, especially at domain boundaries where two nucleating domains converge. Patterning a surface creates user-defined domain boundaries within the monolayer, potentially having a significant impact on the properties of the interface. This dissertation investigates the effect that user-created domain boundaries have on the properties of a monolayer, as studied by electrochemical impedance spectroscopy.

Two patterning methods are investigated for creating user-defined domain boundaries: the soft lithography method of contact printing and site-selective reductive desorption. The electrochemical properties of homogeneous contact printed monolayers are measured and compared to those of monolayers prepared by solution adsorption. The contact printed monolayers are found to have dramatically different impedance behavior from the solution prepared monolayers, consistent with the contact printed monolayers having greater defect density. In addition, these studies show that the overall defect density depends on the concentration of the solutions used for contact printing.

In this work, simple patterns are created by contact printing a pattern onto the substrate and then backfilling the remaining gold substrate by solution adsorption. Backfilling with the same alkanethiol used to create the pattern generates a homogeneous monolayer; however, it is found that the contact printed/backfilled monolayer has an impedance intermediate between the homogeneous contact printed and the homogeneous solution adsorbed monolayer. This result suggests that the backfilling process also saturates the pinhole defects associated with the contact printed areas. In addition to exploring defects that arise from contact printing, simple patterns with user-defined defects, created by site-selective reductive desorption (SSRD), were also investigated. Following the backfill step, the impedance behavior of the SSRD produced patterns was similar to that of the impedance of the initial pattern before backfilling. This important result implies that the domain boundaries play the most important role in defining the overall impedance of the patterned interface.

Acknowledgments

My graduate experience at Virginia Tech was unique but very special thanks to the many people who have guided me along the way. Although my advisor Mark Anderson left the university after my second year, he continued to support me from afar. We had more scientific discussions over the internet, then we did when he was right next door. His belief in knowing that I would succeed without his constant presence gave me more confidence in my own abilities. He taught me how to be an "independent thinker", as he likes to say. I am so grateful for all his support and guidance along the way.

As my co-advisor, Prof. John Morris taught me how to get really excited about science. He included me as one of his own group members and helped develop my communication and presentation skills, among other things. John really cares about the success of his students and encourages them to reach higher. Prof. Gary Long was more than a committee member, he was a mentor and friend. Being his teaching assistant for several semesters, I learned how relate chemistry to the younger students. I appreciated that he frequently stopped by to say hello and check to see if I needed anything, especially in my last semester when I was alone on my floor. I want to thank Prof. Karen Brewer for her invaluable comments on my written documents and Prof. James Tanko for letting me know that I have "nothing to be nervous about". I certainly would not be where I am today without the assistance of my committee.

I was lucky enough to interact with most of the analytical graduate students in a group atmosphere. I got the best of both worlds being part of both a small (Anderson) and large (Morris) group. Wesley Sanders was a great coworker and one of the most motivated people in the world. Watching him work so hard made me work even harder to finish my degree. I especially want to thank Erika Borgerding, Erin Davis, and Lesley Owens for their continued friendship both in and outside the lab because everyone knows in order to stay sane in graduate school, you need to have a life outside the chemistry department. To the rest of the group members, thanks for listening to my electrochemistry talks and for the fun memories.

I wouldn’t be here without the support and encouragement from my family. They willingly agreed to call me Dr. Leslie for at least a month following my defense to my pleasure, and I love them more for it. I can’t thank Andy enough for being there for me during this whole adventure; our relationship has grown stronger through our time apart.

Table of Contents

List of Figures

List of Tables

Chapter 1

Introduction and Motivation

1.1 Self-Assembled Monolayers

Self-assembled monolayers (SAMs) have been used widely as model organic interfaces because of their ease and reproducibility of preparation. Historically, mercaptans (RSH) self-assemble on metallic surfaces to produce densely packed, well-ordered monolayer systems. Metals such as gold, silver, copper or palladium can be used as substrates for self-assembly; however, gold is the most common of the metal substrates used because of its availability, inertness, high binding affinity to mercaptans, and compatibility with many spectroscopic and electrochemical techniques.[1] This document will refer to a gold surface as the preferred substrate, unless otherwise stated. Spontaneous and fast adsorption of the mercaptan to the Au substrate occurs for all preparation methods including solution deposition, vapor deposition, and contact printing. In contact printing, an elastomeric stamp transfers the mercaptan to a substrate in a matter of seconds, rather than the conventional overnight adsorption from solution.[2]

The efficient packing of a Au(111) surface provides an atomically smooth platform for adsorption in which all the surface atoms are equivalent, thus making all the adsorption sites equivalent.[3] The sulfur atom of RSH adsorbs to the three-fold hollow site between gold atoms forming a $(\sqrt{3}\times\sqrt{3})R30°$ structure, where the sulfur atoms are spaced 4.98 Å from the next nearest neighbor. The hydrocarbon chains extend from the surface in an all-trans conformation and tilt ~30° from the surface normal. Figure 1.1 depicts the overlayer structure of adsorbed sulfur atoms on a Au(111) surface, as well as a schematic of the all-trans conformation of a self-assembled monolayer. This type of structural arrangement maximizes the attractive van der Waals interactions between alkane chains and minimizes the overall free energy of the system.[4, 5] Evidence of other structural configurations such as $c(4\times2)$ superlattices exist.[6] Maximum surface coverage or concentration of adsorbed molecules reaches 7.6×10^{-10} mol cm^{-2}.[7, 8] Deviations from this pseudo-crystalline structure arise from the disruption of lateral interactions due to either the introduction of functional groups along the alkyl chain or defects within the monolayer, such as domain boundaries.

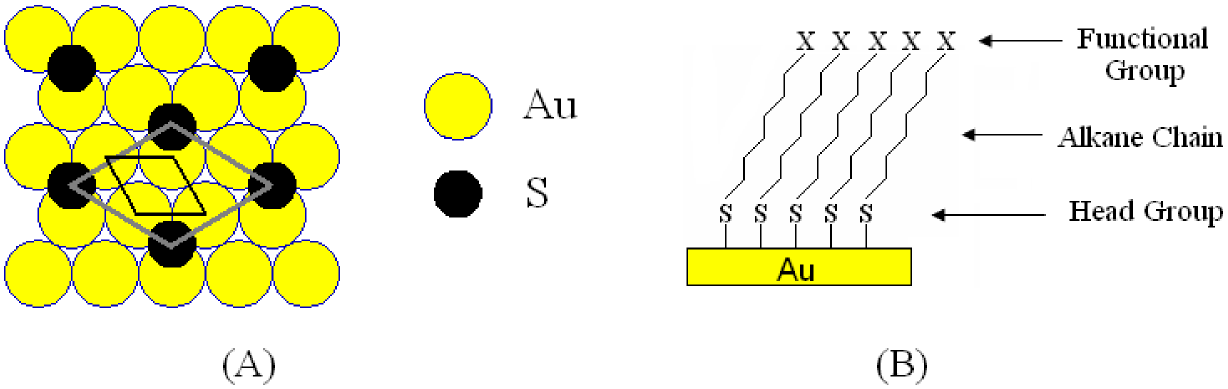

Figure 1.1 $(\sqrt{3}\times\sqrt{3})R30°$ structure of adsorbed mercaptans (A). Schematic of an adsorbed self-assembled monolayer on gold (B).

The monolayer-modified interface can be tailored for specific applications by altering the terminal functional group by standard synthesis techniques. For example, carboxylic acid-terminated SAMs have been used to introduce electrostatic interactions that allow adsorption of enzymes and polyelectrolytes.[9-11] The confinement of enzymes at a modified metal interface allows for surface-sensitive *in situ* measurements of conformational changes without detrimental direct metal-enzyme interactions that lead to complete unfolding of the enzyme.[11] Antibodies can be covalently attached to monolayer-modified surfaces and be used as biosensors.[12]

The adsorption of thiols to a metal surface is driven by two processes: i) the strong interaction of gold and sulfur (50 kcal mol^{-1}), and ii) the lateral van der Waals interactions (approximately 0.5 kcal mol^{-1} per methylene unit) between the hydrocarbon chains.[1] Adsorption of the mercaptan to form self-assembled monolayers can best be described by a Frumkin isotherm.[13] The Frumkin isotherm is a modification of the Langmuir isotherm that allows interactions between adsorbate molecules. The Langmuir model assumes a homogeneous surface (equivalent adsorption sites), the same adsorption mechanism for all adsorbates, and complete saturation of the surface in which only a monolayer forms.[13] The adsorption energy of a Frumkin isotherm is directly related to the surface coverage of the adsorbed species, Γ_i, as

$$\Delta G_i^0(Frumkin) = \Delta G_i^0(Langmuir) - 2g\Gamma_i \qquad \textbf{(1.1)}$$

where ΔG_i^0 is the electrochemical free energy of adsorption and g is the Frumkin interaction parameter, which expresses how increased coverage impacts the adsorption energy.[13] Positive g values represent attractive interactions between neighboring adsorbates, where a negative g parameter signifies repulsion.[13] The Frumkin interaction parameter provides a means to qualitatively investigate the lateral interactions between alkyl chains of self-assembled monolayers through electrochemical methods.[14]

Self-assembled monolayers prepared by solution adsorption of *n*-alkanethiols are known to form well-defined interfacial structures that have few defects.[15, 16] As such, interfaces modified by self-assembly of *n*-alkanethiols can be used to establish standard structure and properties for comparison to monolayers prepared by other modification procedures. Among these properties, electrochemical analysis shows that homogeneous SAMs prepared by solution adsorption of *n*-alkanethiols can act as an insulating barrier to electron transfer.[17] A completely insulating interface is representative of a monolayer with few structural defects and is characteristic of the well-ordered structure of the monolayer.

1.2 Defects in Self-Assembled Monolayers

1.2.1 Defects in the Substrate

Much of the work with SAMs has employed the use of polycrystalline gold; while these substrates have strong (111) texture because of the favorable lower surface energy, varying densities of gross structural defects exist.[1] The quality of the monolayer depends on the nature of the gold surface, therefore substrate defects contribute to defects within the monolayer. Vacancy islands, step edges, and intergrain boundaries are all defects within the metallic substrate.[6]

Vacancy islands are pit-like structures that differ in height by one or two gold atoms from the surface plane caused by the reconstruction of the gold layer during the assembly process.[1, 6, 18] Single atom vacancies grow into large pits due to nucleation of other vacancy sites. What may appear to be vast barren domains of gold are actually well covered areas of monolayer; however, due to the height difference, the vacancy islands image as dark spots in scanning tunneling microscopy.[6] Figure 1.2 schematically represents a vacancy island defect.

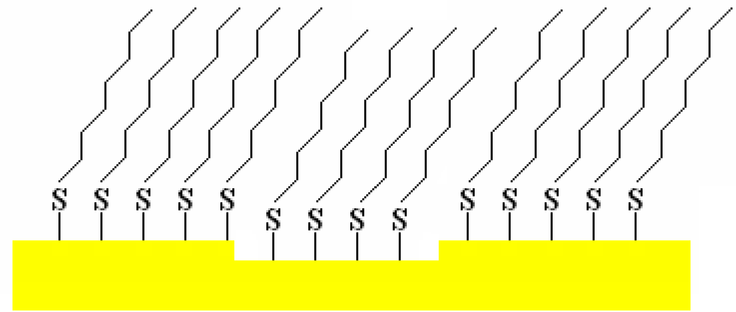

Figure 1.2 Schematic representation of a vacancy island defect in a self-assembled monolayer.

Step edges and intergrain boundaries occur naturally in polycrystalline gold substrates and even substrates with strong (111) texture. It is unfeasible for adsorbed species to be ordered at these regions due to the defects in the underlying metallic structure. These substrate defects disrupt the favorable lateral interaction of adsorbates, causing defects within the monolayer. Annealing processes can be used to limit the degree of these types of defects.[1]

1.2.2 Defects in the Monolayer

Imperfections in the metallic structure certainly cause defects in the commensurate adlayer, but monolayer defects also occur independent of the substrate. Monolayer defects include molecular vacancies, domain boundaries, and collapsed sites. These defects lead to incomplete adsorption of molecules and low surface coverage. At any defect site the lateral chain-chain interactions are disrupted forming less ordered monolayer structures. The density of defects can negatively affect the electrochemical properties of the modified interface, thus low monolayer defect densities are desired.

Molecular vacancies are described as absent alkanethiolate molecules, also called pinholes.[6, 18] Entire rows, either straight or zig-zag, of the overlayer may be missing; this typically occurs with short alkanethiols (n<12).[6] Defect sites also occur when alkyl chains are not fully extended, preventing further adsorption and creating areas of exposed bare gold. An example of a molecular vacancy can be seen in Figure 1.3. The most prominent molecular defects appear at domain boundaries.

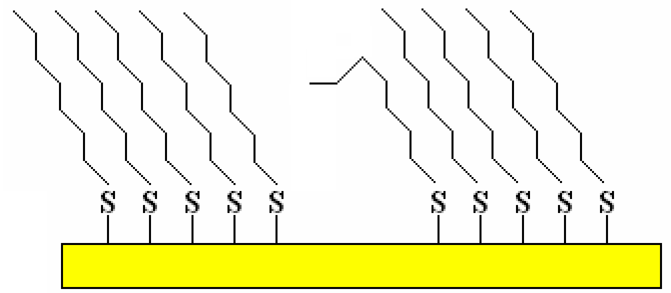

Figure 1.3 Schematic representation of a molecular defect in a self-assembled monolayer.

The self-assembly of mercaptans follows a nucleation mechanism; small groups of molecules adsorb to the substrate and grow into structured domains.[19] The space where two adjacent well-ordered domains meet is called a domain boundary.[1] Because the two domains may not be oriented in the same direction, the lateral interactions between domains are disrupted. Figure 1.4 schematically illustrates a domain boundary defect. Rotational domain boundaries form as the orientation of one domain morphs into a second positional orientation, and an offset in the lateral direction produces translational domain boundaries.[18] The weakened lateral interactions at domain boundaries leave areas of exposed Au substrate, which is of great concern for electrochemical applications because these sites contribute most to the electrochemical response of a monolayer-modified interface.[20] Domain boundaries are an intrinsic property of self-assembled monolayers and must be considered when forming complex interfacial structures.

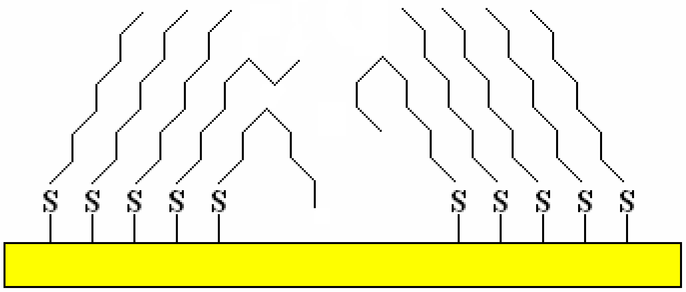

Figure 1.4 Schematic representation of a domain boundary defect in a self-assembled monolayer.

The Hutchison group has investigated the lateral interactions within a monolayer by using internal hydrogen bonding between amide containing alkanethiol molecules.[21-24] Their studies show greater stability for such layers because of the additional contribution of the buried hydrogen bonding to the van der Waals lateral interactions, whereas mixtures of these molecules and *n*-alkanethiols cause spontaneous phase separation .[21, 22] This work can be used to learn more about the domain boundaries and possible functionalities along the thiol chain that may increase the lateral interactions between phases.

Collapsed sites are regions of low thiol concentration along the interface where neighboring alkanethiol molecules are not ordered in the all-trans conformation, much like at domain boundaries.[25] The thiol molecules at these sites may in fact still protect the surface but not to the same degree as well-ordered domains. The film thickness at collapsed sites is less than at thiol-rich domains; this means molecules in solution can approach the electrode surface at a shorter distance, therefore collapsed sites can impact the electrochemical properties of monolayer-modified electrodes.[26]

1.3 Electrochemistry of Self-Assembled Monolayers

When performing electrochemistry on modified surfaces, the organosulfur molecules act as a blocking film such that charge cannot easily cross the metal-solution interface regardless of the applied potential.[13] An electrochemical cell has two key responses to slow electron transfer with applied potentials—resistance and capacitance. Both can be modeled as electric circuit elements and measured by electrochemical impedance spectroscopy. This technique relies on the structure of the electrode-solution interface, so discussion begins there.

In an electrochemical cell, application of potential causes excess charge to build on the metal electrode surface, and oppositely charged ions accumulate on the solution side of the interface forming an electric double layer at the interface. The Gouy-Chapman-Stern model[13] describes this phenomenon by combining two previous theories. The Helmholtz model[13] states that solvent molecules closest to the electrode surface are specifically adsorbed and form the inner Helmholtz plane (IHP) or Stern Layer. The solvated ions therefore can approach the electrode surface only to this defined inner layer distance. These nonspecifically adsorbed ions extend from the outer Helmholtz plane (OHP) to the bulk solution; this region is called the diffuse layer.[13] The Gouy-Chapman model did not assume a plane of closest approach nor provide a complete description of the electric double layer. The charge separation between the metal electrode and the OHP in an electrochemical cell is modeled by a capacitor in an electrical circuit.

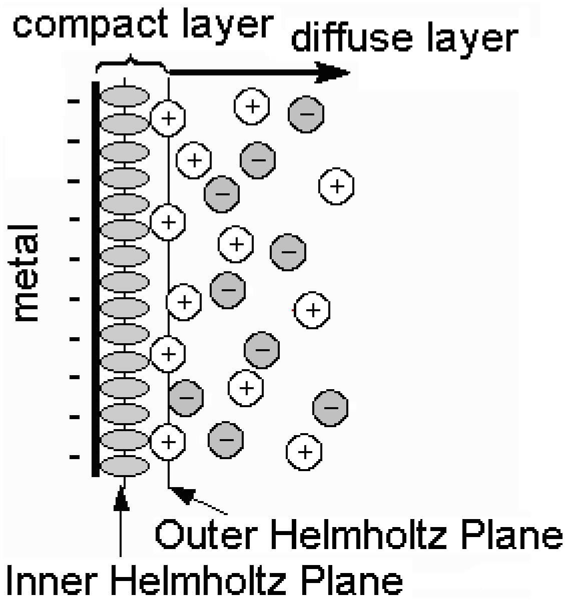

Figure 1.5 Representation of the electric double layer according to the Gouy-Chapman-Stern model.

A capacitor consists of two charged plates separated by a dielectric medium. Applying potential to one of the plates causes the accumulation of oppositely charged ions on the other and produces a charging current. Porter, Allara, and Chidsey showed that two factors can change the capacitance of a modified surface—the dielectric constant of the medium (ε) and the distance separating the charged plates (*d*).[15] Capacitance (C) is defined as

$$\mathrm{C} = \frac{\varepsilon_0 \varepsilon}{d}, \tag{1.2}$$

where ε_0 is the permittivity of free space. Film thickness of the SAM determines the interplate distance; increasing the alkyl thiol chain length consequently decreases the capacitance.[27] Porter et al. showed that for alkanethiol monolayers ($CH_3(CH_2)_nSH$) where $n \geq 9$, the surface is nearly impermeable, while shorter alkanethiols only partially act as dielectric barriers due to increased structural defects.[15]

Charge transfer at monolayer-modified electrodes occurs freely at defect sites and by electron tunneling mechanisms through thiol-rich domains.[20] It is the charge transfer at all types of defects that contribute most to the electrochemical response. At disordered regions, the redox probe in solution can approach the metal surface at shorter distances (i.e. a closer outer Helmholtz plane). The more defects present, the larger the electrochemical response. For some applications this could be detrimental because the response of the defects could overshadow the reaction of interest. Therefore, minimizing the influence of defects is critical for electrochemical applications.

1.4 Patterning Interfaces with Self-Assembled Monolayers

1.4.1 Coadsorption from Solution

Binary mixtures can be achieved by one of three adsorption methods: i) coadsorption of two thiol solutions (R-SH + R'-SH),[28, 29] ii) adsorption of asymmetric disulfides (R'SSR),[30, 31] or iii) adsorption of asymmetric dialkylsulfides (RSR').[1] A monolayer prepared by coadsorption of thiol mixtures does not necessarily reflect the mole fraction of thiol in solution or result in a homogeneously comprised film. Similar length alkyl chains (differing by 2 methylene units)[32] and asymmetric disulfides[31] are capable of forming homogenous films. However, alkyl chains differing by six or more carbons exhibit phase-separated domains, as do mixtures of terminally functionalized thiols. Higher mole fractions of preferentially adsorbed thiols can be attributed to the effects of chain length and functional groups. Over time, longer *n*-alkanethiols tend to dominate the relative ratio compared to the shorter alkanethiols because of the increased stabilizing lateral interactions.[33, 34]

The relative composition of the two component thiols of a mixed monolayer can be determined using reductive desorption. Because lateral interactions between the two species differ, a voltammogram shows two distinct peaks for each of the desorbed species.[35] Both Chidsey and Kakiuchi observed that reductive desorption is not random, but proceeds domainwise; the desorption begins at the defective domain boundaries while surrounding domains remain intact.[35, 36] By using ferrocene-terminated SAMs with *n*-alkanethiols, Chidsey provided a domain boundary model to describe the fast exchange of molecules at domain boundaries, whereas slower kinetics arise because interior molecules must diffuse to the boundaries in order for exchange to occur.[36]

Forming SAMs via coadsorption is the easiest way to control surface properties such as wettability[37] but allows the user no control over the created "pattern". Therefore, other techniques have been proposed to create well-defined regions of alkyl thiols on surfaces such as dip-pen nanolithography,[38] contact printing,[2, 39, 40] and site-selective reductive desorption.[41-44]

1.4.2 Contact Printing

The method of contact printing (CP) to pattern SAMs was first introduced by Kumar and Whitesides in 1993.[2] This is a dry process in which an elastomeric stamp facilitates the adsorption of alkanethiols on gold surfaces, some with features in the micrometer and sub-micrometer range.[45] Stamps can be used multiple times without the need to re-ink for quick fabrication of multiple substrates; deposition times vary from a few seconds to minutes[46] but remain much shorter than solution adsorption times, thus making this technique favorable.

The typical stamp is created by polymerizing dimethylsiloxane monomer on a master template with the negative of the desired features and allowing to cure as poly(dimethylsiloxane) or PDMS. The stamp is then peeled from the master, washed in ethanol, dried in a stream of N_2, and then "inked" with a 0.1-10 mM solution of thiol in ethanol.[2] The choice of solvent is important because PDMS has a Young's modulus of 1 MPa, making it susceptible to swelling and pattern distortion; it has been shown that ethanol only slightly swells PDMS by 2.5%.[47] After inking, the stamp is brought into direct contact with the gold substrate, where thiol transfers from the PDMS via multiple mass transport pathways.[47] Removal of the stamp after the desired amount of time reveals a patterned alkyl thiol surface. Figure 1.7 demonstrates the stamping process.

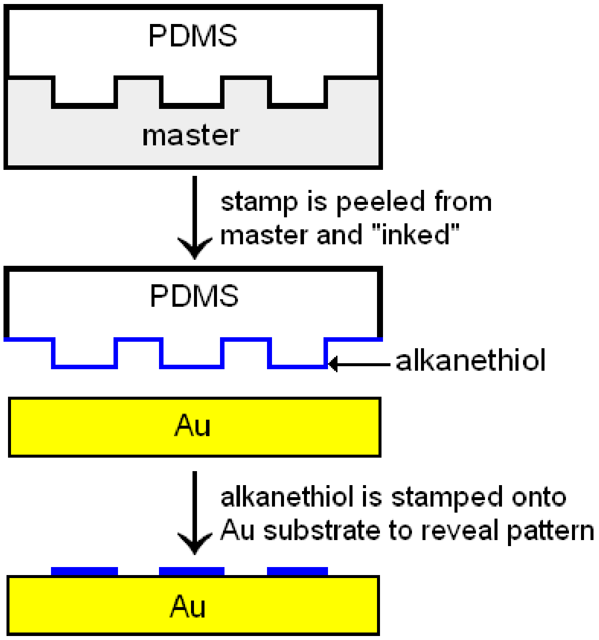

Figure 1.6 Scheme of the contact printing process.

The structure and properties of monolayers formed by contact printing have been frequently compared to solution-adsorbed SAMs.[48-52] Larsen *et al.* found that by using sufficiently concentrated *n*-dodecanethiol inking solution, printed monolayers were structurally indistinguishable from solution formed monolayers.[48] Similar results were found in a study by Fischer *et al*. using near edge x-ray absorption fine structure spectroscopy.[49] Losic *et al*. investigated the role of surface topography and ink concentration on the quality of monolayers formed by contact printing and from solution.[51, 53] As with the other studies, similar structure and qualities of contact printed *n*-hexadecanethiol SAMs were produced when using higher thiol ink concentrations.

1.4.3 Patterning via Probe Microscopy

Several probe microscopy techniques have been utilized to produce patterned monolayer structures by either creating positive or negative features across the interface using the scanning probe. The Mirkin group devised a new method of lithography called dip-pen nanolithography (DPN) where a sharp AFM tip dipped in thiol "ink" creates patterns by "writing" on a metallic "paper".[38] Serial motion parallel to the surface generates positive features of 100 nm in dimension,[38] but electrochemical means can reduce feature sizes down to 30 nm.[54] Zhang exploited the fact that electrochemical desorption initiates at domain boundaries in order to "whittle away" large alkyl thiol islands to smaller dimensions.[54, 55] This further demonstrates that without strong lateral interactions all around, adsorbed molecules are less stable and susceptible to desorption. Many examples of initial patterning and decoration exist for dip-pen nanolithography, including biologically active protein nanoarrays and deposition of dendrimers.[56, 57] Unlike most lithographic techniques, DPN produces positive features without complicated processing methods of chemical etching or photoresists.

Another probe microscopy method that does not involve photolithography to generate patterned surfaces is site-selective reductive desorption using scanning electrochemical microscopy

(SECM). SECM is used to create negative features in well-ordered monolayers by selective electrochemical reduction and subsequent removal of small domains of thiol.[43] This method differs from dip-pen nanolithography because negative features within the monolayer are produced instead of building positive thiol structures and the process occurs in solution phase. In either method, the exposed metallic substrate can be further modified with a different thiol molecule to make a mixed monolayer. Site-selective reductive desorption will be used to produce patterns within monolayers because scanning electrochemical microscopy was readily available for use, and SECM can also be used to image the electrochemical topography of the patterned surface.

1.5 Conceptual Basis of Dissertation

The focus of this dissertation involves the fundamental understanding of the extent to which interfacial patterns impact the overall behavior of monolayer-modified electrodes with specific interest in user-defined domain boundaries. Domain boundaries are an intrinsic property of self-assembled monolayers and are considered significant defects because they can extend over large distances (10s of Å).[18] We can study these defects by creating patterned monolayers in a controlled environment with a specified number of user-defined domain boundaries. In this case, the domain boundaries are 100s of μms in length which exaggerates their influence on the behavior.

The role of defects created during the patterning process is thoroughly examined within this dissertation. In most applications of patterned SAMs, the extent of defects does not greatly influence the average response of the system. However, defect sites do impact the electrochemistry of these interfaces, for they are considered as tiny electrodes within a modified surface where electron transfer occurs.[25] Because the surface will be patterned on the macroscopic scale, vast phase boundary defects may be introduced. In certain applications, it is imperative to minimize the defect influences so that the dominant contribution to the measured electron transfer current is not occurring at these sites; this affords one to gain a better understanding of the electron transfer mechanisms through SAMs.[36, 58]

The work herein primarily focuses on the contact printing patterning method. In Chapter 3, the stamping process is evaluated as to the quality of homogeneous monolayers formed. Parameters such as ink concentration, alkane chain length, and functionality are examined. Properties of contact printed monolayers are compared to the ideal solution adsorbed monolayers of the same thiol. Average structure and electrochemical behavior of the homogeneous contact printed monolayers are determined by reflection-absorption infrared spectroscopy and cyclic voltammetry. Electrochemical impedance spectroscopy (EIS) was used to estimate the charge transfer resistance of each monolayer and to describe the defect density using a microelectrode model. This study is the first time contact printed SAMs have been thoroughly evaluated by EIS.

Chapter 4 describes how introducing simple patterns onto the electrode interface impacts the impedance. Experiments using the print and backfill procedure are discussed in terms of the impact of "user-defined" domain boundaries according to charge transfer resistance values obtained using EIS. Binary patterns of homo- and heterogeneous mercaptans with one user-defined domain boundary are compared to more complex patterns which contain up to four user-defined domain boundaries. This chapter also presents a study into the backfill procedure and its role in defect density. The complex patterns are also imaged using scanning electrochemical microscopy.

Finally, Chapter 5 discusses creating patterns via site-selective reductive desorption using a scanning electrochemical microscope. This procedure brings new insight into the integral role defects have in the electrochemical behavior of modified interfaces. The dependence of probe-substrate separation distance and hydrocarbon chain length of *n*-alkanethiol on the size of desorbed areas is examined. Patterned monolayers were studied using electrochemical impedance. Scanning electrochemical microscopy was used to both generate interfacial patterns and image the surface based on electrochemical reactivity.

Chapter 2

Experimental Methods and Parameters

2.1 Introduction

This chapter describes the experimental methods used to prepare and characterize self-assembled monolayers on gold substrates. The preparation methods include contact printing and self-assembly from solution phase. The characterization techniques include reflection-absorption infrared spectroscopy (RAIRS), cyclic voltammetry (CV), reductive desorption (RD), electrochemical impedance spectroscopy (EIS), and scanning electrochemical microscopy (SECM). The general experimental parameters for each technique will be given in this chapter with further details to be discussed in subsequent chapters.

2.2 Chemicals

Alkanethiols including *n*-pentanethiol, *n*-octanethiol, *n*-dodecanethiol, 11-mercaptoundecanoic acid, and *n*-octadecanethiol were purchased from the Aldrich Chemical Company (Milwaukee, WI). Potassium hexacyanoferrate (II) trihydrate, potassium hexacyanoferrate (III), sodium phosphate monobasic monohydrate, and sodium phosphate dibasic heptahydrate were all purchased from Fisher Scientific Company (Pittsburg, PA). Potassium hydroxide was purchased from Sigma-Aldrich (St. Louis, MO). Poly(dimethylsiloxane) was purchased as brand name Sylgard 184 from Dow Corning (Midland, MI). All chemicals were analytical grade and were used without further purification. *n*-Alkanethiol solutions for monolayers were prepared in absolute ethanol . All other solutions were prepared with water that was deionized with an 18 MΩ Milli-Q ion exchange filter from Millipore Incorporated.

2.3 Substrate Preparation

2.3.1 Gold Substrates

2.3.1.1 Gold on Glass

Gold substrates were purchased from Evaporated Metal Films, Inc. (Ithaca, NY). These substrates are prepared with a 50 Å chromium underlayer and a 1000 Å layer of gold evaporated onto 1” x 1” glass. Prior to use, the gold substrates were cleaned in a 3:1 v/v mixture of concentrated sulfuric acid and 30% hydrogen peroxide, known as piranha solution, for 15 min. **Beware when using piranha solution as it is highly corrosive and reacts violently with organic materials.** After cleaning in piranha, the gold substrates were rinsed with deionized water and blown dry with a stream of nitrogen.

2.3.1.2 Gold Disk Electrodes

Gold disk electrodes with working area of 0.034 cm^2 were purchased from CH Instruments (Austin, TX). Prior to use, the electrodes were polished using 0.05 μm alumina grit, immersed in an ultrasonic bath for 1 minute, and then cleaned electrochemically by cycling the potential between -0.8 to 1.2 V at 0.1 V/s in the presence of a 0.10 M sulfuric acid solution.

2.3.2 Monolayer Preparation

2.3.2.1 Solution Adsorption

Monolayers were prepared by immersing the clean gold substrate in a 0.001 M *n*-alkanethiol solution for at least 18 hours at 25°C. The substrates were then rinsed in ethanol, followed by water, and dried in a stream of nitrogen gas prior to use.

2.3.2.2 Contact Printing

The poly(dimethylsiloxane) stamps (Sylgard 184) were prepared by thoroughly mixing a 10:1 ratio of base to curing agent, then allowing the PDMS mixture to cure for at least 24 hours at 25°C on an unpatterned glass surface. Freshly prepared stamps were rinsed with pure ethanol and dried under N_2 gas prior to loading the stamp with solutions of the *n*-alkanethiol. *n*-Alkanethiol concentrations of 0.001, 0.010 or 0.025 M in ethanol were applied to the PDMS stamps for 2 min, dried under N_2, and used immediately. The thiol was transferred onto the Au electrode by placing the PDMS stamp in contact with the Au substrate for 1 minute. The modified electrode was then rinsed in ethanol, water, and dried using nitrogen gas prior to experiments.

2.4 Reflection-Absorption Infrared Spectroscopy

2.4.1 Method

Reflection absorption infrared spectroscopy (RAIRS) not only yields valuable information about the vibrational properties and functional groups of the organosulfur molecules, but also qualitatively depicts the ordering of the molecules along the surface. When light of a specific frequency is reflected off a monolayer surface, the molecules will absorb light if the surface selection rule is obeyed. The surface selection rule states that only molecules with a change in dipole moment perpendicular to the surface will be IR active.[59] Alkanethiols adsorbed to a Au(111) surface have four absorption peaks in the 2800-3000 cm^{-1} region corresponding to both methyl and methylene symmetric and asymmetric stretching modes. A shoulder on the 2918 cm^{-1} peak arises from the Fermi resonance between the fundamental methyl symmetric stretch and overtones of asymmetric bending modes from the lower frequency region.[60] The peak position and peak shape from RAIRS will be used to describe the ordering of self-assembled monolayers on gold surfaces.

2.4.2 Conditions

Infrared measurements were conducted with a Nicolet Model 710 FTIR (Madison, WI) spectrometer using a liquid nitrogen cooled HgCdTe detector. The infrared beam was *p*-polarized using a Zn-Se wire grid polarizing filter (Cambridge Physical Sciences, IGP 228) and reflected onto the samples using a Spectra Tech (Stamford, CT) FT80 specular reflectance attachment at an incident angle of 80º. Spectra were referenced to a clean, gold substrate prepared as described in Section 2.3.1.1. Spectra were collected at 2 cm^{-1} resolution and 512 interferometer scans. Spectral data was acquired by Omnic (Version 3.0) software.

2.5 Cyclic Voltammetry

2.5.1 Method

A simple electroanalytical method to characterize self-assembled monolayers adsorbed onto gold substrates is cyclic voltammetry (CV). Cyclic voltammetry measures current as a function of potential applied to the modified substrate. The potential is varied linearly with respect to time using a triangular waveform, in which the potential is ramped from an initial potential at t_1 to a final potential at t_2; at this time the direction of potential scan is reversed in order to return to the initial potential at t_3. Figure 2.1 schematically illustrates the triangular waveform used in CV.

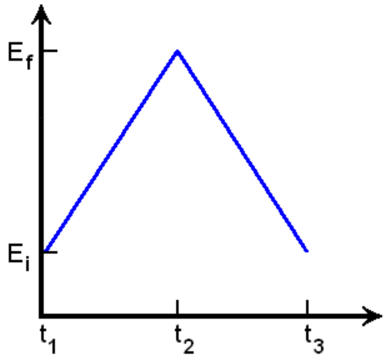

Figure 2.1 Triangular waveform used in cyclic voltammetry. E_f final potential, E_i initial potential, t_n time.

Several key characteristics of a voltammogram are used to define the heterogeneous kinetics of the observed reaction. For a reversible reaction as shown in Figure 2.2, the peak separation, ΔE_p, is independent of scan rate and equal to 59 mV/*n* (where *n* is the number of electrons transferred).[13] The ratio of peak currents, $i_{pc}/i_{pa} = 1$, also regardless of scan rate.[13] These qualities are indicative of fast kinetics. For irreversible kinetics, ΔE_p is greater than 250 mV/*n*. The larger the peak separation, the slower the kinetics of the reaction; this experimental result is used to describe the blocking characteristics of SAM-modified electrodes.

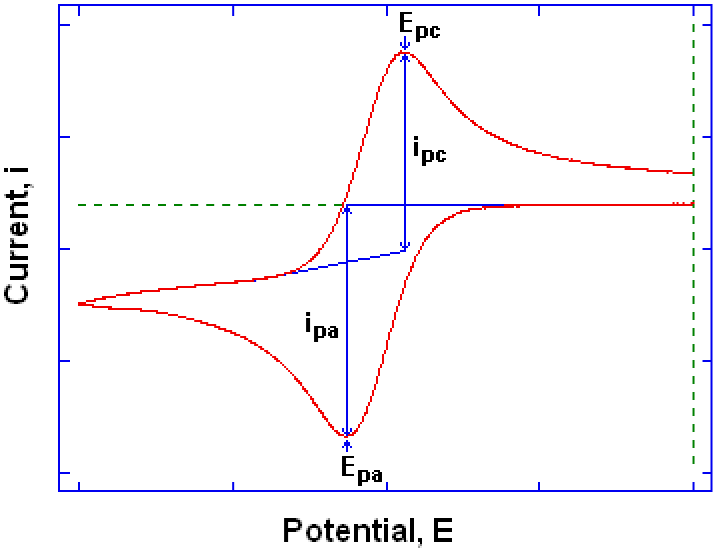

Figure 2.2 Typical cyclic voltammogram for a system with reversible kinetics. E_{pc} cathodic peak potential, E_{pa} anodic peak potential, i_{pc} cathodic peak current, i_{pa} anodic peak current.

2.5.2 Conditions

Cyclic voltammetry measurements were conducted with a CH Instruments model 604B potentiostat (Austin, TX). The potential was swept between -0.2 and 0.7 V versus a saturated Ag/AgCl reference electrode at a rate of 0.1 mV/s. The hexacyanoferrate (II/III) couple was used as the redox probe with a formal potential of 0.22 V vs. Ag/AgCl. Solutions of 0.005 M hexacyanoferrate (II/III) were made with 0.1 M KCl in 0.05 M phosphate buffer, pH 7. The phosphate buffer was prepared from 0.025 M sodium phosphate dibasic and 0.025 M sodium phosphate monobasic; the pH was adjusted to 7.0 using dilute sodium hydroxide while monitoring with a pH meter.

Two different electrochemical cells were used based on the type of gold substrate employed as the working electrode. The typical static three-electrode electrochemical cell was used for gold disk electrodes, Figure 2.3A.

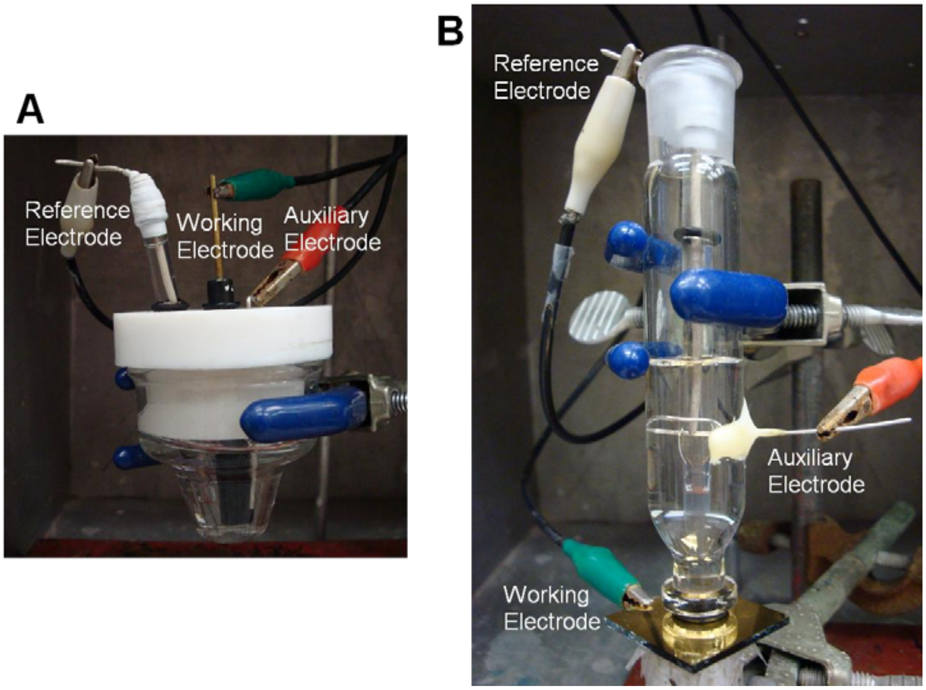

Figure 2.3 Electrochemical cells used for experiments with (A) gold disk electrodes and (B) gold on glass.

However, this apparatus cannot be used for gold on glass slides. A modified drop electrochemical cell similar to the one described by Chidsey was used instead, Figure 2.3B.[58] A platinum wire was fused into the glass cell as the auxiliary electrode, while the Ag/AgCl reference electrode was suspended above the gold slide. The glass cell was sealed to the gold slide with an o-ring. The surface area of the working electrode was determined by chronocoulometry to be 0.62 cm^2.

2.6 *Reductive Desorption*

2.6.1 Method

Reductive desorption is a linear sweep voltammetry technique in which a large negative overpotential is applied to the modified gold electrode. The gold-sulfur bond is reduced in a one-electron Faradaic process, causing the molecules to desorb from the surface.[8] This desorption allows for the surface coverage, Γ, to be determined by integrating the cathodic peak to determine the total charge, Q, required to desorb the molecules that comprise the monolayer, Figure 2.4. The total charge is related to the surface coverage by:

$$\Gamma = \frac{Q}{nFA}, \tag{2.1}$$

where Q is the amount of charge passed, n is the number of electrons involved in the electron-transfer process ($n = 1$ for presented material), F is the Faraday constant, and A is the geometric area of the electrode. Low surface coverage indicates less order within the system possibly due to deposition time and method, disruption of stabilizing lateral interactions, or high defect density.[46]

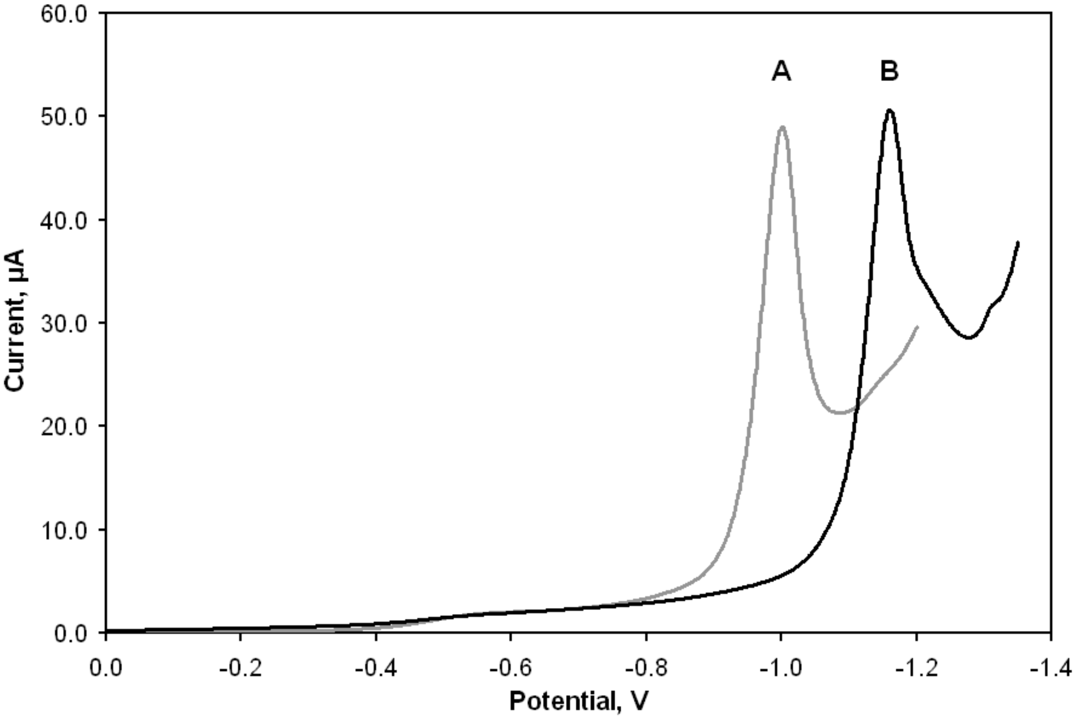

Figure 2.4 Reductive desorption of (A) *n*-octanethiol and (B) *n*-dodecanethiol on gold on glass substrates. Conditions: 0.5 M KOH, potential vs. Ag/AgCl.

Because the strong interaction between sulfur and gold is equivalent for each thiol molecule in the assembly, the energy required to break this interaction is also equal; however, not all self-assembled monolayer systems desorb at the same potential. Shifts in the desorption peak potential, E_p, arise from the energy differences of the lateral van der Waals interactions among the molecules that comprise the monolayer. Factors such as functionality and length of the alkyl chains have either positive or negative effects on E_p, as seen in Figure 2.4. The longer alkanethiol chain, *n*-dodecanethiol, desorbs at a larger negative overpotential because of the increased lateral interactions.

2.6.2 Conditions

Reductive desorption measurements were conducted with a CH Instruments model 604B potentiostat (Austin, TX) in 0.5 M potassium hydroxide (electronic grade). The potential was swept from 0 to -1.3 V versus a saturated Ag/AgCl reference electrode at a rate of 50 mV/s. All solutions were degassed with N_2 for 5 minutes prior to measurement.

2.7 Electrochemical Impedance Spectroscopy

2.7.1 Method

Impedance is simply the ability of a circuit to resist the flow of an alternating current (AC). When a direct current (DC) potential is applied to a circuit, resistors impede the flow of electrons, and capacitors act as open circuits; however, with an AC potential, capacitors can impact the impedance.[61] Simply, the contributions of all resistive circuit elements account for the total impedance, Z. Impedance can be mathematically expressed by Ohm's Law:

$$Z = E / I \;; \qquad \textbf{(2.2)}$$

where E is potential in volts (V) and I is current in amps (A).[13]

Electrochemical impedance spectroscopy (EIS) measures the response of an electrochemical cell to an applied AC potential as a function of frequency.[13, 61, 62] The measured current responds to the applied sinusoidal AC potential in two ways, with a phase shift and a change in amplitude.[62] Figure 2.5 schematically illustrates the current response of an electrochemical cell affected by impedance. A pure resistor changes the amplitude of the current response while being in-phase with the applied potential, where as the current response to an AC potential across a pure capacitor is 90º out-of-phase with no change in amplitude.[63]

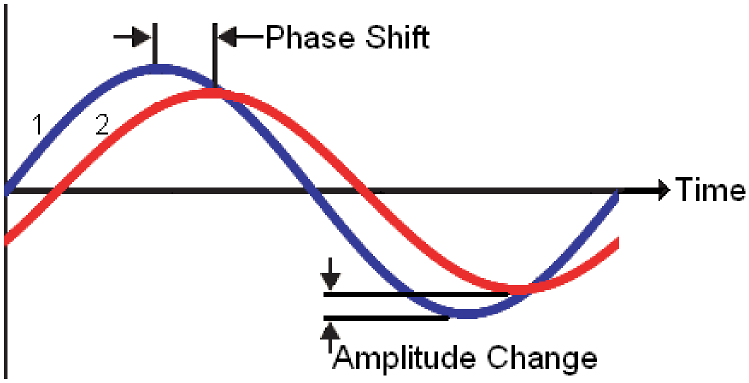

Figure 2.5 Illustration of phase shift and amplitude change between applied AC potential (1) and measured current (2) with respect to time during electrochemical impedance measurements.

The total impedance of a circuit can be represented by two components—the real component, Z', which describes the resistance, and the imaginary component, Z", which describes the combined capacitance and inductance. In Cartesian coordinates, impedance is expressed as

$$Z(\omega) = Z' + jZ'' \qquad \textbf{(2.3)}$$

where ω is the angular frequency, and *j* is the complex number $\sqrt{-1}$. A common way to graphically display impedance data is the complex impedance plot, also called a Nyquist plot, shown in Figure 2.6. The resistive or real component is plotted on the *x*-axis, and the capacitive or imaginary component is plotted on the *y*-axis. A system that has both resistive and capacitive contributions to the impedance yields the characteristic semi-circular shape. A disadvantage of the complex impedance plot is that it does not directly show the strict dependence on frequency, which increases from right to left as indicated. However, this format does allow for a simple graphical representation of how the system behaves.

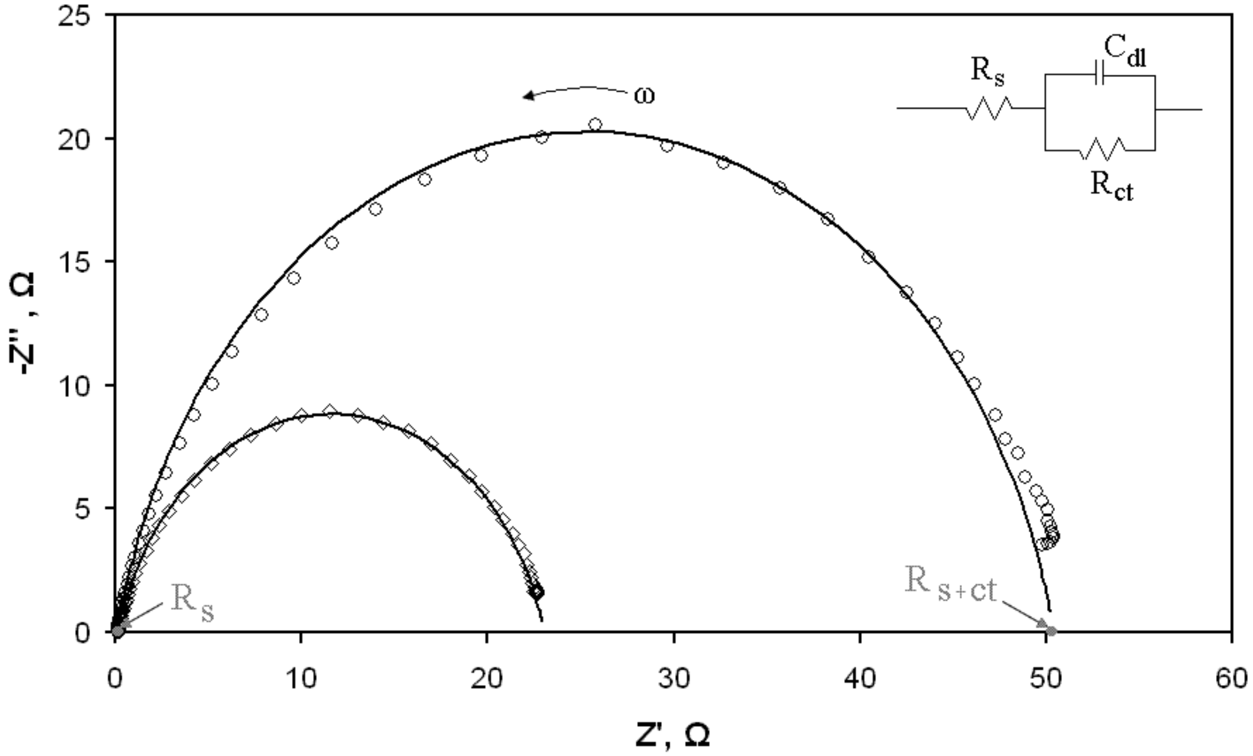

Figure 2.6 Complex impedance plots of two monolayer modified Au electrodes. Inset shows Randles equivalent circuit. Z" imaginary impedance, Z' real impedance, ω angular frequency, R_s solution resistance, R_{ct} charge transfer resistance, C_{dl} double layer capacitance.

An electrochemical cell can be modeled as a simple circuit using the Randles equivalent circuit, shown as the inset of Figure 2.6. The Randles circuit provides a means to equate the real, physical processes occurring in the electrochemical system to circuit elements. This model is used to represent coatings on surfaces, such as a SAM-modified electrode. The solution resistance, R_s, is the uncompensated resistance of the electrolyte solution between the working and reference electrodes. The monolayer coating acts as a capacitor, C, and is characterized by its thickness (*d*) and dielectric (ε). Capacitance is defined as

$$C = \frac{\varepsilon_0 \varepsilon}{d} \tag{2.4}$$

where ε_0 is the permittivity of free space. The resistance of the monolayer is the charge transfer resistance, R_{ct}, and can be estimated as the measured diameter of the semicircle in the complex impedance plot. Theoretical models of the Randles circuit are applied to the experimental data to estimate the resistive and capacitive circuit elements. The impedance responses in Figure 2.6 (open points) have been estimated using a nonlinear least squares fitting routine employing the Randles circuit model (solid lines).

There are two limiting cases at the frequency boundaries. At high frequencies the capacitive nature of the monolayer acts as a short circuit and only solution resistance, R_s, is observed. For the other extreme case, the "capacitor" acts as an open circuit at low frequencies, and both solution resistance and charge transfer resistance, $R_{ct,}$ are observed.[62] These resistive elements can be determined from the complex impedance plot as the *x*-intercepts indicated in Figure 2.6. With this visual representation of the circuit, it is easy to make qualitative assessments of monolayer integrity (*e.g.* the longer the diameter of the semicircle, the greater the resistance of the monolayer).

A graphical method to present impedance data that illustrates the electrochemical response as a function of frequency is called the Bode plot. The log of the frequency is plotted versus 1) log of the total impedance, |Z|, and 2) phase shift, φ. The Bode plots for an electrochemical cell equivalent to the Randles model are shown in Figure 2.7. In the log |Z| vs. log ω plot, the impedance of the resistive components appear as horizontal lines because resistors respond to applied potential independent of frequency.[62] The linear portion of this plot with slope of -1 is the typical impedance response of a capacitor, which varies with the inverse of the frequency.[62] The double layer capacitance can be estimated from this plot by extrapolating the line as indicated.[61] The phase angle shift of the applied voltage and the measured current response as function of frequency is presented by plotting -φ vs. log ω. At high and low frequency limits, the resistive contributions to the impedance dominate, and the phase angle is nearly zero because resistors do not change the phase angle.[61] Capacitive contributions to the impedance approach 90º, the phase angle of a pure capacitor. The Bode plot is advantageous when examination of the impedance response as a function of frequency is necessary.

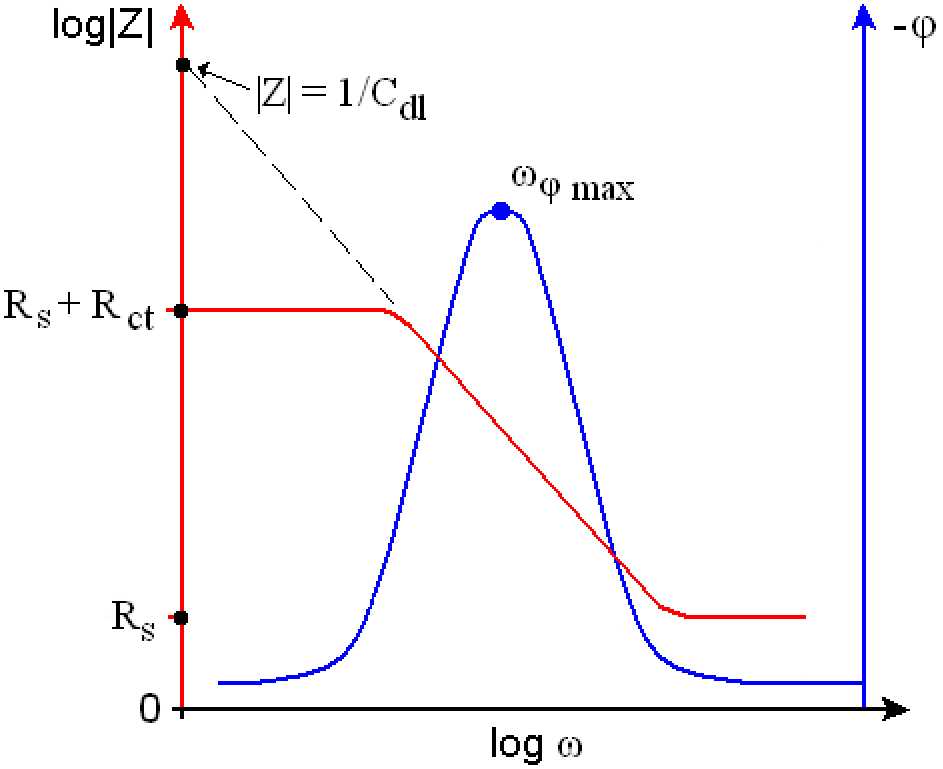

Figure 2.7 Bode plots of impedance. |Z| magnitude of total impedance, φ phase angle, ω angular frequency, R_s solution resistance, R_{ct} charge transfer resistance, C_{dl} double layer capacitance.

Both complex impedance plots and Bode plots have their advantages and disadvantages. Bode plots explicitly show the dependence of impedance on frequency, whereas complex impedance plots do not. For the electrochemical systems explored in this work, the magnitude of the charge transfer resistance is the most important feature; therefore, complex impedance plots are used to present the data.

2.7.2 Conditions

Electrochemical impedance measurements were conducted with a CH Instruments model 604B potentiostat (Austin, TX). Solutions used were the same as from cyclic voltammetry measurements, described in section 2.5.2. Measurements were performed by applying an AC potential having a 5 mV amplitude that is symmetric about the formal potential of the redox probe [0.2 V vs. Ag/AgCl for hexacyanoferrate (II/III)]. The frequency range was 1.0×10^5 Hz to 0.1 Hz. Quantitative estimates of the equivalent circuit elements were obtained by fitting the experimental data to a Randles equivalent circuit using the nonlinear least squares fitting routines provided by LEVM 7.0 (Solartron, written by James Ross Macdonald).

2.8 Scanning Electrochemical Microscopy

2.8.1 Method

Scanning Electrochemical Microscopy (SECM) is a type of scanning probe microscopy, but differs from its non-invasive counterparts in that an electrochemical reaction occurs at a microelectrode probe, and the measurement is performed in solution phase.[64, 65] A disk ultramicroelectrode (UME) usually made of a platinum wire with radius of 1 to 25 μm sealed in glass and polished serves as the probe.[65] The potential of both the probe and the gold substrate are controlled by a bipotentiostat. The probe is moved by either by inchworm actuators or piezo controllers.[44] A computer controls the position of the probe and records the observed current at each *xy* position. Figure 2.8 displays a schematic of the SECM apparatus.

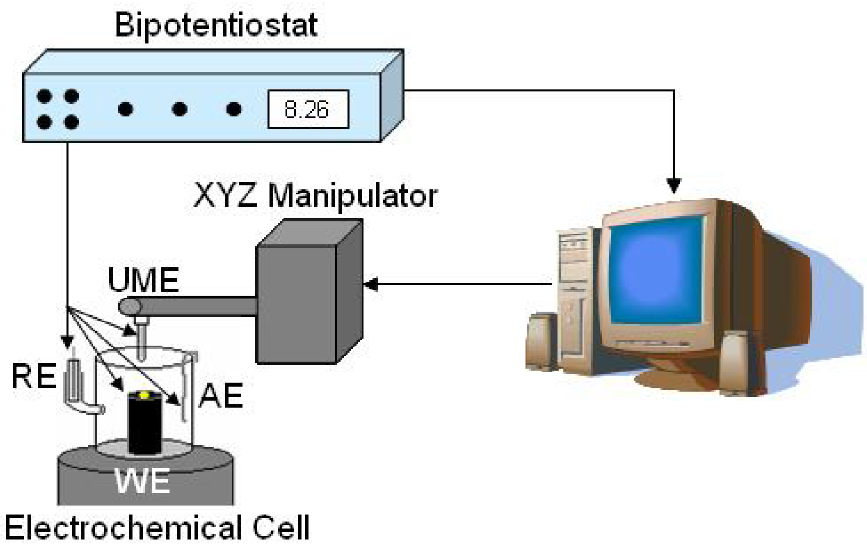

Figure 2.8 Schematic of scanning electrochemical microscopy apparatus. AE auxiliary electrode, RE reference electrode, UME ultramicroelectrode, WE working electrode.

The faradaic current response is monitored either by collection mode, where the probe potential is held constant, or feedback mode in which the properties of the substrate cause changes in the detected current.[64] In the generation/collection mode, products are electrogenerated at the substrate and detected at the probe. Both the probe current and substrate current are monitored simultaneously.[64] For feedback mode, a substrate will perturb the probe signal in a characteristic way for an insulating or conductive substrate to yield negative or positive feedback, respectively.[65] When the UME probe is far from the substrate, hemispherical diffusion occurs and a steady-state current, $i_{\mathrm{T},\infty}$, exists as

$$i_{\mathrm{T},\infty} = 4nFD_O C_O^* a \tag{2.5}$$

where D_O is the diffusion coefficient, C^*_O is the concentration of the electroactive species, and a is the probe radius.[64] As the distance between the substrate and probe becomes small, the current response can change in one of two ways. An insulating substrate will block diffusion of the electrochemical mediator species, R, from reaching the probe, which decreases the probe current,

i_T; this is called negative feedback. On the other hand, a conductive substrate causes an increase in probe current because the surface is able to regenerate R from the reaction product, O, at the probe creating a larger flux of R at the probe called positive feedback. Figure 2.8 illustrates the possible electrode responses measured in feedback mode.

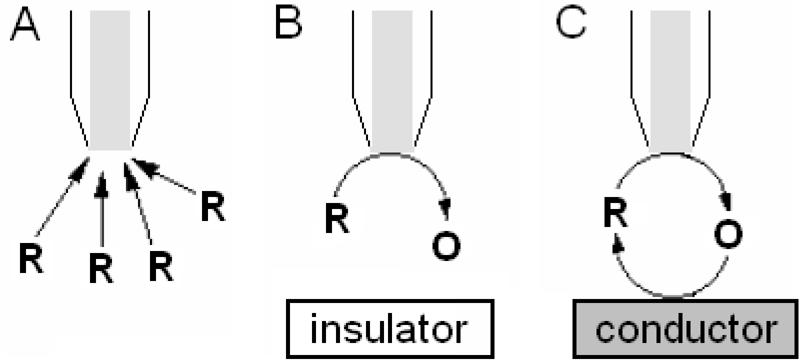

Figure 2.9 Illustration of current response in feedback mode when the probe is (A) far from the substrate or near (B) insulating and (C) conducting substrates. R reduced electrochemical mediator species, O oxidized electrochemical mediator species.

Characteristic approach curves are used to illustrate negative and positive feedback as in Figure 2.10. An approach curve is generated by moving the UME probe in the *z*-direction towards the surface and observing the perturbation in the steady-state current. In negative feedback, the current decreases at small probe-substrate distances due to the blocked diffusion of the electrochemical mediator to the UME probe. The portion of mediator near the UME is oxidized at the probe and diffusion of excess mediator is hindered by the insulating substrate. In positive feedback, however, the current increases at small probe-substrate distances. This occurs because the substrate can regenerate the original electrochemical mediator species, and the redox cycle can continue. An approach curve is performed prior to SECM imaging to aid in the placement of the UME probe at a reasonable *z*-height.

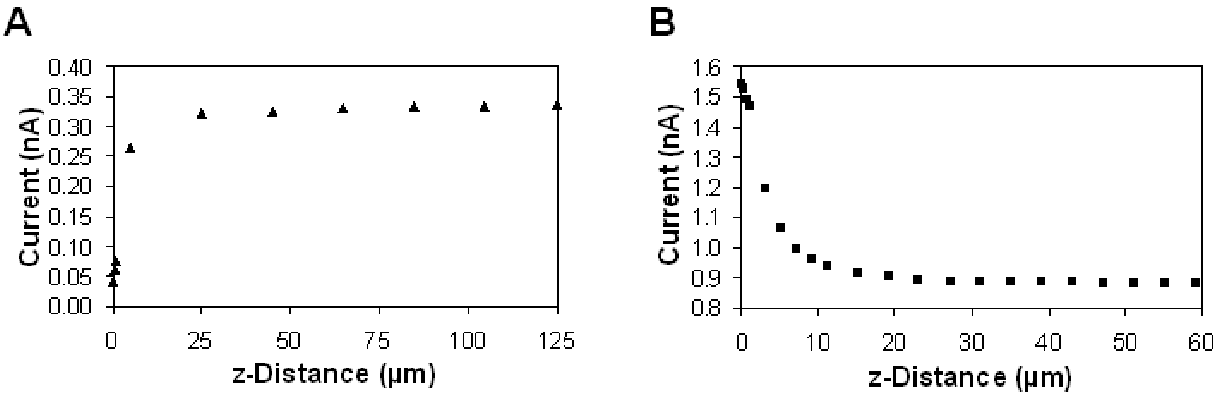

Figure 2.10 Approach curves generated over (A) insulating and (B) conducting substrates. SECM conditions: 10 µm Pt UME at 0.6 V vs. Ag/AgCl, Au disk electrode at -0.1 V vs. Ag/AgCl, 5 mM $K_4Fe(CN)_6$ in 0.1 M KCl.

The ability of SECM to distinguish between conducting and insulating regions allows for the topography of an electrochemical interface to be imaged by rastering the UME probe in the *xy*-plane at a constant height above the surface. Figure 2.11 demonstrates the capacity of SECM to distinguish between conductive and insulating regions. A commercially available multi-disk electrode array with 50 µm conductive disks was imaged by SECM. The hills (high current) are the conducting disks where positive feedback is measured, and the surrounding regions of low current result from the negative feedback measured when the UME probe is over the supporting insulator.

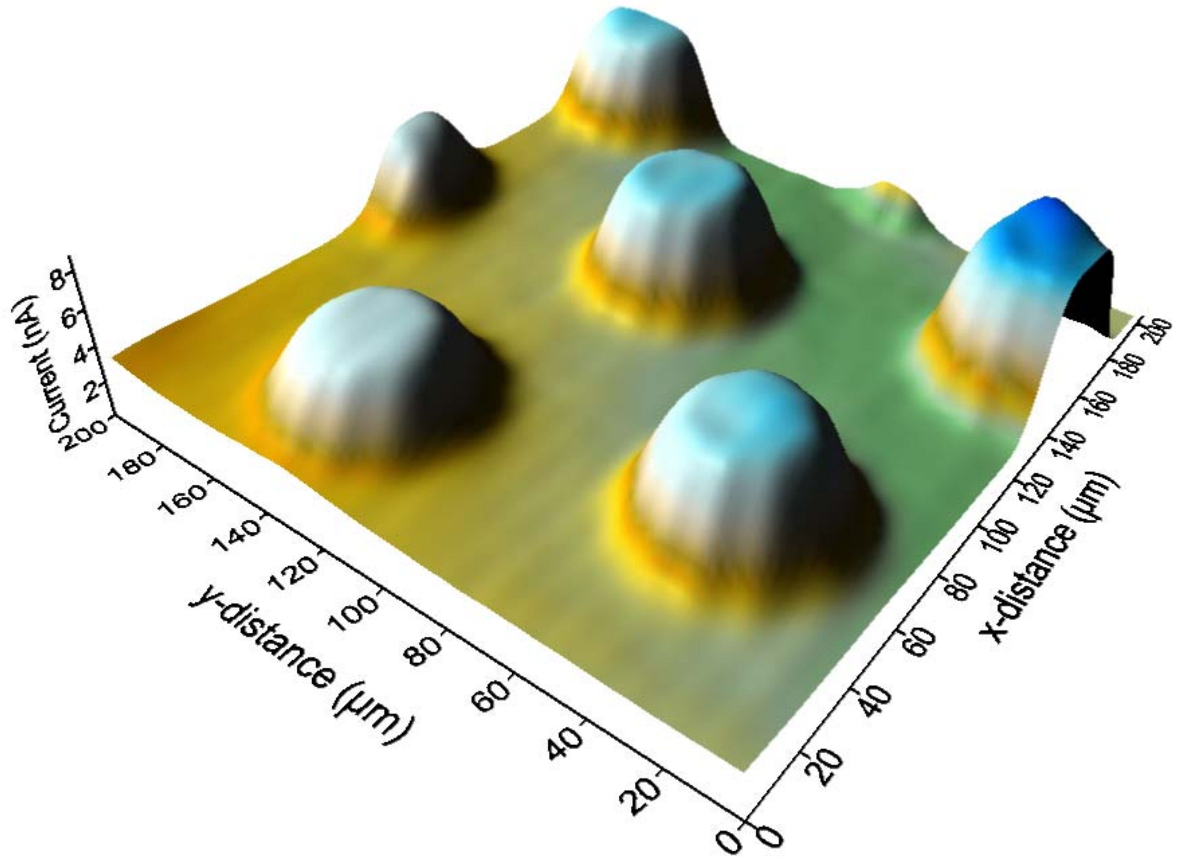

Figure 2.11 SECM 3D color map of a multi-disk electrode array with 50 µm conducting disks surrounded by insulating material.

2.8.2 Conditions

Potential bias to both working electrodes was applied using a Cypress Systems model 66-EI400 bipotentiostat (Chelmsford, MA). A 10 µm Pt ultramicroelectrode from CH Instruments (Austin, TX) was used as the SECM probe electrode, and a gold electrode was used as the modified substrate. Prior to use, the UME was polished in 0.05 µm alumina grit and held in an ultrasonic bath for 1 minute. Applied potentials were referenced to a Ag/AgCl reference electrode. A 0.005 M solution of hexacyanoferrate (II) in 0.1 M KCl and pH 7.0 phosphate buffer was used for SECM imaging. A solution containing only one-half of the redox couple is necessary for

SECM measurements, due to the mechanics of the technique. Feedback mode was used to image the topography of the substrates.

The SECM apparatus was constructed locally by a former group member using a Thorlabs Inc. (Newton, NJ) *xyz* platform equipped with Z600 series actuators operated in a closed loop configuration.[66] The initial *x*, *y*, and *z* positions of the ultramicroelectrode probe relative to the monolayer-modified Au substrate are established manually by visual inspection. The actuators are controlled during each scan with locally written software. The step resolution for this instrument is 40 nm, while the imaging resolution is equivalent to the size of the ultramicroelectrode probe (10 μm). After manual placement of the ultramicroelectrode, a program control records an approach curve and fixes the electrode position when the measured current has changed 50% from the bulk value. The SECM apparatus is contained in a Faraday cage to eliminate interferences, Figure 2.12.

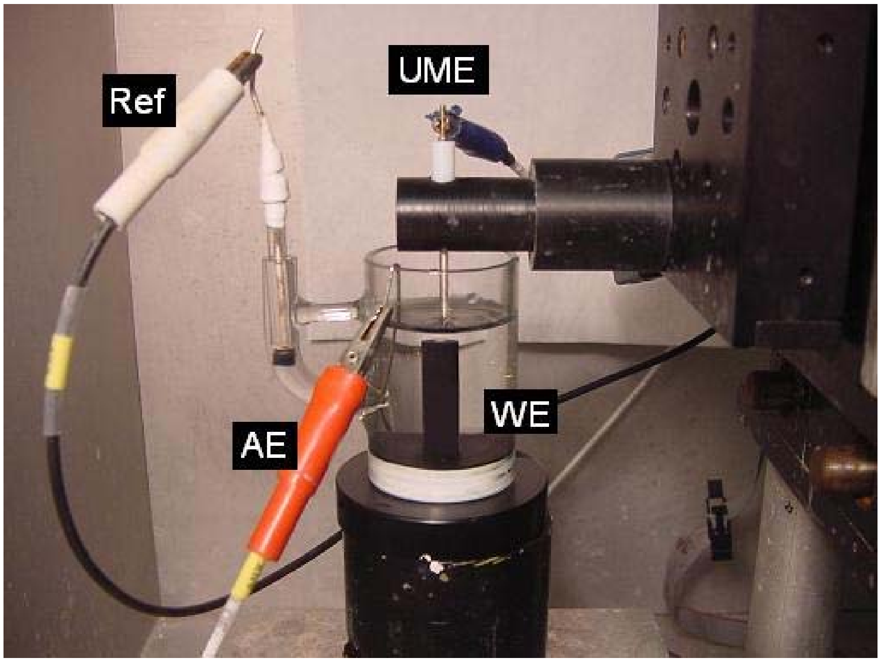

Figure 2.12 SECM apparatus and electrochemical cell design. AE, auxiliary electrode; Ref, reference electrode; UME, ultramicroelectrode probe; WE, Au working electrode.

Chapter 3

Characterization of Homogeneous Contact Printed Self-Assembled Monolayers

3.1 Introduction

The soft-lithography method of contact printing (CP) was investigated to determine the quality of monolayer formed by the printing process. Planar, featureless stamps were used to form homogeneous contact printed monolayers of *n*-alkanethiols and ω-substituted mercaptans. The contact printed monolayers were evaluated for structure, defect density, and permeability; these properties were then compared to those of monolayers prepared by solution adsorption. The main characterization technique was electrochemical impedance spectroscopy, with supporting results from cyclic voltammetry. This work is the first comparison study of contact printing and solution adsorbed SAMs using EIS to be reported.

It is important to have a fundamental understanding of how contact printed monolayers behave electrochemically before creating complex interfacial motifs. This knowledge will help to determine how the introduction of a pattern with user-defined domain boundaries will affect the overall properties of a modified interface. We must answer questions such as:

- Do contact printed monolayers have similar electrochemical behavior to solution adsorbed monolayers?
- Do contact printed monolayers have more defects than solution adsorbed monolayers?

- Does the patterning method contribute to the number of defects within the monolayer?
- How do these defects impact the overall properties of the monolayer?

While contact printing is a relatively new lithography method, it has been well documented within the literature and is by far one of the simplest and most accessible patterning methods. However, there are no established procedures regarding ink load time, stamp time, stamp pressure, and ink concentration to use when preparing contact printed monolayers. This fact makes it difficult to compare literature reports of contact printed monolayers. It has been reported that using ink concentrations greater than 0.02 M thiol form monolayers that are structurally indistinguishable from solution adsorbed monolayers.[48, 53] For these reasons, differing concentrations of thiol ink were examined in order to find the best conditions to make reproducible SAMs by contact printing.

3.2 Results and Discussion

3.2.1 n-Octadecanethiol

The comparison between solution adsorbed and contact printed monolayers began with *n*-octadecanethiol for several reasons. Within the literature, long alkanethiol chains are found to be well-ordered due to the favorable lateral interactions between the numerous methylene units. The interfacial structure and electrochemical behavior of such monolayers are well documented; therefore, any deviations from the expected behavior when preparing monolayers differently will be apparent. Long alkanethiols form dense structures which can be probed by infrared spectroscopy. The hydrocarbon chains also act as an insulator when adsorbed on an electrode; this property will be examined using CV and EIS.

Reflection absorption infrared spectroscopy (RAIRS) was used to evaluate the structural ordering within *n*-octadecanethiol self-assembled monolayers formed by contact printing and solution adsorption (Figure 3.1). The peak position of the asymmetric stretch of the methylene group ($CH_{2,as}$) is characteristic of the degree of ordering of the molecules within the monolayer. With a well-ordered monolayer, the $CH_{2,as}$ is found at approximately 2918 cm^{-1}.[16] Finding the $CH_{2,as}$ mode at this energy implies that the chains are fully extended in an all-trans conformation. The width of the peak is also characteristic of the extent of ordering of the monolayer; peak widths of 12 cm^{-1} or less are also characteristic of a well-ordered monolayer.

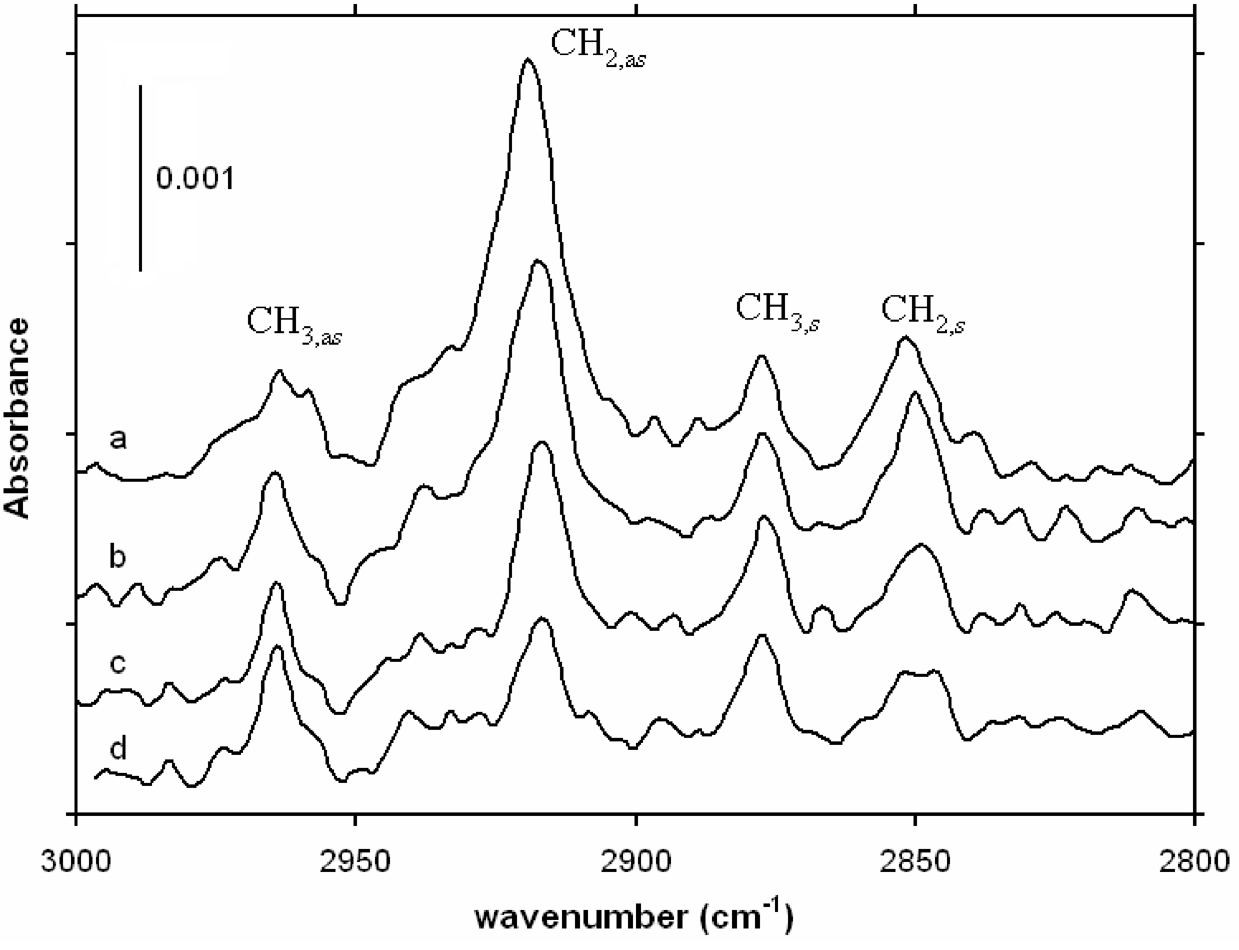

Figure 3.1 RAIR spectra of *n*-octadecanethiol self-assembled monolayers on gold. (a) 0.001 M contact printed, (b) 0.010 M contact printed, (c) 0.025 M contact printed, (d) 0.001 M solution adsorbed. Spectra are offset for clarity.

Summarized in Table 3.1 are the RAIRS data collected for *n*-octadecanethiol monolayers prepared by contact printing and solution adsorption. As the concentration of the *n*-octadecanethiol used to prepare the contact printed monolayer increases, the position of the $CH_{2,as}$ peak shifts to lower wavenumber and approaches the value found with the immersed SAM (2917 cm^{-1}). Even though the changes in the peak positions are within the uncertainty of the measurement (±2 cm^{-1}), the trend is consistent with literature reports and suggests that the average structural order of monolayers prepared by contact printing increases with increasing concentration of the *n*-octadecanethiol used to prepare the monolayer. A similar trend is observed with the peak width; e.g. the peak width approaches the value expected of a well-ordered monolayer with increasing ink concentration. From the RAIRS data, the 0.025 M *n*-octadecanethiol monolayer appears to be structurally indistinguishable from a monolayer formed by solution adsorption.

Concentration, Method	Frequency, cm^{-1} $CH_{2,as}$	FWHM, cm^{-1} $CH_{2,as}$	Peak Height Ratio $CH_{2,as}$:$CH_{3,s}$
0.001 M, CP	2919±2	15±2	3.6
0.010 M, CP	2918±2	14±2	3.0
0.025 M, CP	2917±2	12±2	1.6
0.001 M, Immersion	**2917±2**	**10±2**	**1.2**

Table 3.1 Summary of RAIRS data obtained for the antisymmetric methylene stretch ($CH_{2,as}$) of *n*-octadecanethiol monolayers formed by contact printing with varying ink concentrations and immersion methods. FWHM, full width at half-maximum.

Another experimental method for comparison of the monolayers is to evaluate the peak height ratio of the asymmetric methylene stretch ($CH_{2,as}$) to the symmetric methyl stretch ($CH_{3,s}$) from the RAIRS data. Figure 3.2 illustrates the direction of these dipole moments for an even numbered alkanethiol adsorbate. At full coverage, the adsorbed molecules tilt at ~30° relative to the surface normal. The absorption intensity of vibrations is a function of the component of the transition dipole moment perpendicular to the surface. If the $CH_{3,s}$ peak is weakly intense or not apparent in the spectrum, the molecules are likely tilting at a higher angle due to the fact that the transition dipole moment of the $CH_{3,s}$ stretch is more parallel to the surface, thus decreasing the intensity according to the surface selection rule.[67] At the same time, the dipole moment of the $CH_{2,as}$ stretch is more perpendicular to the surface and increases in intensity. As the concentration of ink is increased, the ratio of $CH_{2,as}$:$CH_{3,s}$ peak intensity decreases indicating the chains are positioned more upright. This result supports the idea that higher ink concentrations produce more complete monolayers with expected tilt angles.

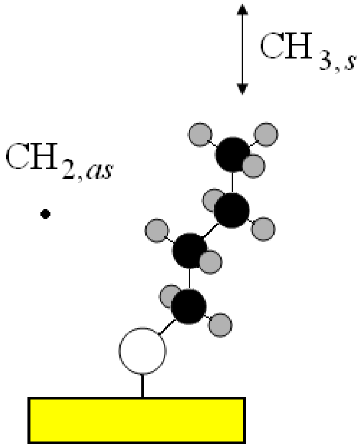

Figure 3.2 Schematic representation of the transitional dipole moments of $CH_{2,as}$ and $CH_{3,s}$ vibrational modes of a *n*-alkanethiol with even number of carbons adsorbed on a Au substrate and tilted at the idealized 30° from the surface normal. The transition dipole moment of the $CH_{2,as}$ stretch is ⊥ to the C-C-C plane, and transition dipole moment of the $CH_{3,s}$ stretch lies along the C-C bond.

Cyclic voltammetry provides additional qualitative evidence of the trend in the structural ordering of the monolayer. This data also provides an assessment of a film's ability to block the electron transfer process to a redox probe in the adjacent solution. As seen in Figure 3.3 the magnitude of the cyclic voltammetry peak current decreases with increasing *n*-octadecanethiol concentration. The monolayer prepared by contact printing with 0.025 M *n*-octadecanethiol has a similar shape and current response to that found with a monolayer formed by solution adsorption. This indicates that the monolayers prepared by these two methods have interfaces with qualitatively similar structures and properties. This result is in good agreement with the infrared spectroscopy data and with previous literature reports,[48, 49] and suggests that the contact printed monolayers prepared using higher concentrations are structurally similar to monolayers prepared by solution adsorption.

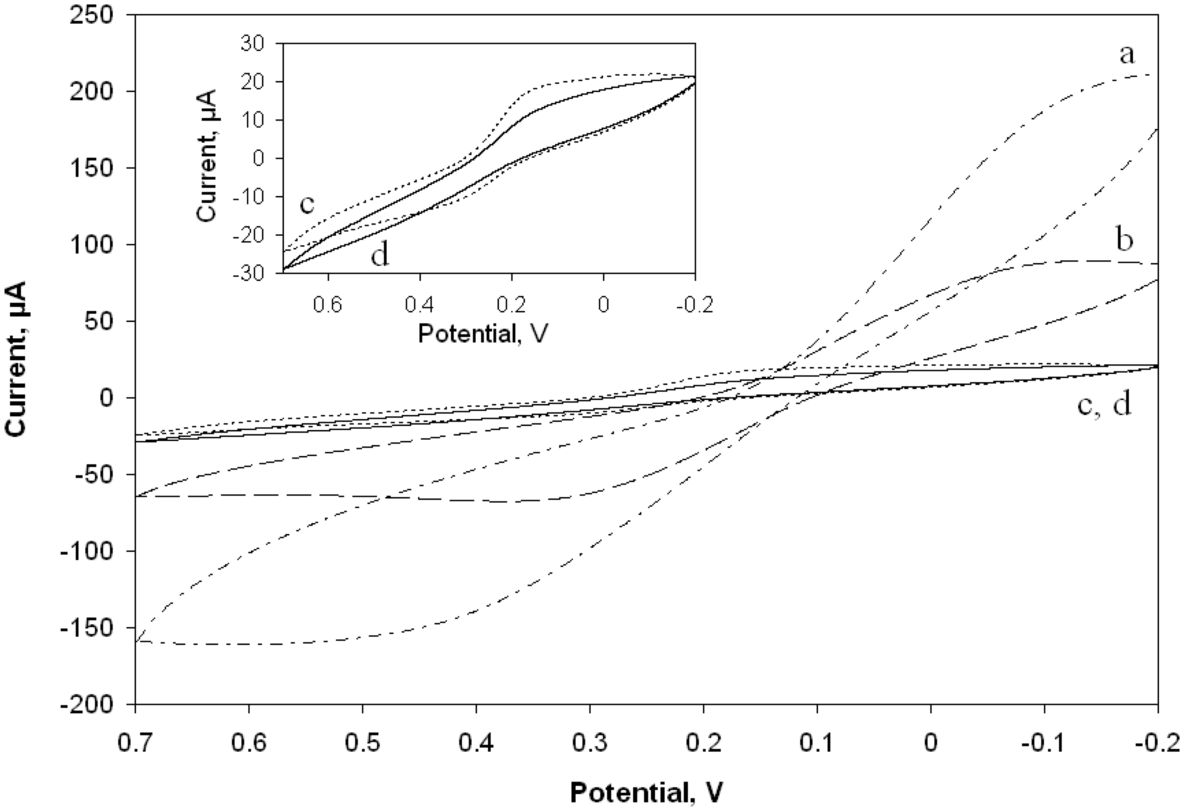

Figure 3.3 Current vs. Potential curves for cyclic voltammetry experiments for the oxidation of 0.005 M $Fe(CN)_6^{-4}$ solutions in aqueous 0.10 M KCl at gold electrodes modified by contact printing with (a) 0.001 M, (b) 0.010 M, and (c) 0.025 M *n*-octadecanethiol and by immersion in 0.001 M *n*-octadecanethiol solutions. The inset shows a magnified view of the current vs. potential response for monolayers (c) and (d). The cyclic voltammetry scan rate was 0.050 V/sec.

While the contact printed monolayer may be structurally similar to monolayers prepared by solution adsorption as evaluated by RAIRS and cyclic voltammetry, electrochemical impedance spectroscopy provides evidence that the two monolayer preparations result in different behaviors, even when forming the contact printed monolayers using high *n*-octadecanethiol concentrations. Figure 3.4 shows the complex impedance plots for *n*-octadecanethiol monolayers formed by contact printing using varying concentrations and by solution adsorption. As with the RAIRS and CV data, increasing the concentration of the *n*-octadecanethiol improves the quality of the monolayer as evidenced by the increase in charge-transfer resistance of the contact printed modified interface. This behavior is consistent with increasing order of the monolayer. Unlike the RAIRS and CV data, however, the charge transfer resistance of the 0.025 M contact printed *n*-octadecanethiol remains much lower than that of the solution formed *n*-octadecanethiol monolayer. As discussed by Fawcett, EIS is an electrochemical technique that is much more sensitive to the details of the interfacial properties than cyclic voltammetry.[68] From the EIS data it is apparent that contact printed monolayers, even those prepared from solutions with relatively high concentrations of *n*-alkanethiol, contain significantly more defects than monolayers prepared by solution adsorption.

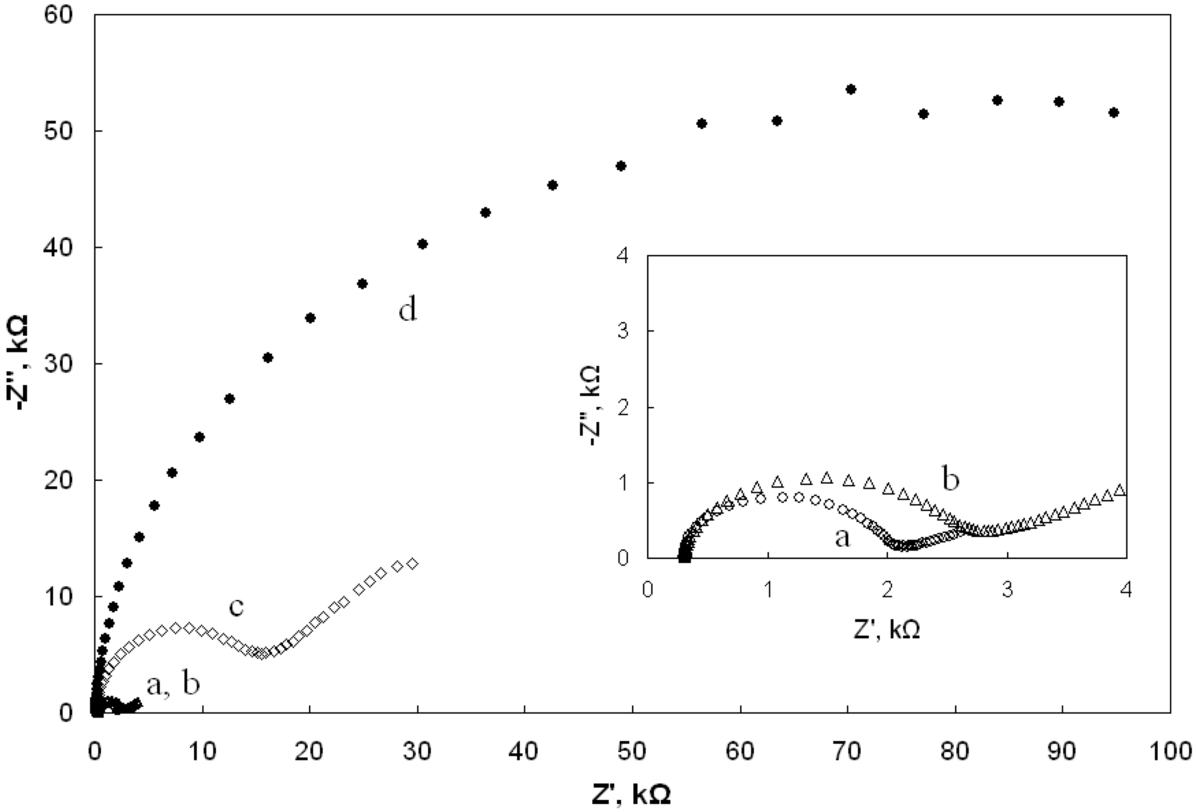

Figure 3.4 Complex impedance plots using 0.005 M $[Fe(CN)_6]^{-4/-3}$ redox probe at a gold electrode modified by contact printing with (a) 0.001 M *n*-octadecanethiol, (b) 0.010 M *n*-octadecanethiol, and (c) 0.025 M *n*-octadecanethiol and by immersion of the gold substrate in 0.001 M *n*-octadecanethiol solutions. The open circles (a) and the open triangles (b) overlap. The inset shows an expanded view of (a) and (b).

The apparent charge transfer resistance of a modified interface includes the contributions from the charge transfer resistances at defect sites (e.g. pinholes, domain boundaries, and/or collapsed sites) and thiol-rich domains.[69] For a well-formed monolayer, the contributions of the charge transfer resistances at defects are minimal and most of the charge-transfer occurs at the thiol-rich domains; consequently, the large impedance measured with the solution adsorbed *n*-octadecanethiol monolayer is characteristic of a monolayer with relatively few defects. The electron transfer rate at defects within the monolayer is much larger than within defect-free thiol domains; therefore, the apparent charge transfer resistance of a monolayer with a significant amount of defects will be dominated by the charge transfer resistance at these defects, which in turn produces small impedance values. For the series of *n*-octadecanethiol monolayers, the impedance results suggest that, even though the monolayers appear from the infrared spectroscopy and cyclic voltammetry data to be structurally similar, the contact printed monolayers are much more defective than the solution adsorbed monolayer.

Gold Substrate	**Concentration of Thiol, Method**	**R_s (Ω)**	**R_{ct} (kΩ)**	**C (μF)**
Gold on Glass	0.001 M, CP	307±2	1.42±0.01	6.46±0.06
	0.010 M, CP	309±2	2.04±0.02	5.17±0.07
	0.025 M, CP	189±7	17.7±0.1	3.91±0.13
	0.001 M, Immersion	193±6	98.8±4.5	3.95±0.17
Gold Disk Electrode	0.001 M, CP	150±3	63.8±0.7	1.52±0.04
	0.010 M, CP	156±5	313±7	1.17±0.03
	0.025 M, CP	158±7	750±17	1.34±0.01
	0.001 M, Immersion*	145±3	1480±29	0.96±0.01
	0.001 M, Immersion	155±1	11800±272	0.91±0.01

Table 3.2 Summary of fitted EIS data of *n*-octadecanethiol monolayers on gold substrates. *Adsorption time of 15 minutes.

The results presented above were all performed with substrates prepared by vapor depositing gold on glass slides. In an attempt to improve reproducibility, the gold substrate was replaced with a gold disk electrode. Errors associated with the drop electrochemical cell were thus eliminated. Impedance measurements of *n*-octadecanethiol monolayers on a gold disk electrode parallel the previous results, however the overall charge transfer resistance values were significantly higher (Table 3.2). This is due to the quality of the gold substrate and difference in cleaning preparations.

Estimates of the capacitance of the *n*-octadecanethiol monolayers support the conclusions drawn from the RAIRS analysis. It was discussed that lower ink concentrations used to form contact printed monolayers result in monolayers in which the methylene chains tilt at larger angles than the expected 30º from the surface normal. Capacitance is indirectly proportional to the distance separating the two charged plates; as the distance increases, capacitance decreases. This trend is apparent for the capacitance values of *n*-octadecanethiol monolayers seen in Table 3.2. As the concentration of thiol ink increases, the capacitance decreases indicating that the molecules are more upright. However, the density of interfacial defects within the monolayer can also contribute to the observed capacitance, for monolayers of high defect density have high capacitance. Defect density will be discussed fully in Section 3.2.5.

3.2.2 n-Dodecanethiol

A series of *n*-dodecanethiol monolayers were analyzed electrochemically in the same manner as the *n*-octadecanethiol monolayers described in the previous section. *n*-Dodecanethiol was chosen because it also forms well-ordered monolayers, similar to *n*-octadecanethiol. We wanted to examine several alkanethiols of varying chain length to determine if the same trends in the electrochemical behavior occur for contact printed monolayers prepared with the various alkanethiols.

Cyclic voltammetry was used to qualitatively evaluate the charge transfer resistance of *n*-dodecanethiol monolayers. The shape of the CV curve and the peak separation, ΔE_p, are used to compare the monolayers (Table 3.3). All contact printed layers had peak-shaped CV curves indicative of defect sites within the monolayer. The peak separation of CP-SAMs increases from 0.309 V to 0.473 V as the ink concentration increases. This result suggests that the quality of the film is dependent on ink concentration. This also follows the trend observed with the *n*-octadecanethiol CV curves. The immersion formed SAM had an exponential CV curve that signifies a well-formed layer in which electron transfer occurs by a tunneling mechanism through the film, Figure 3.5.[20]

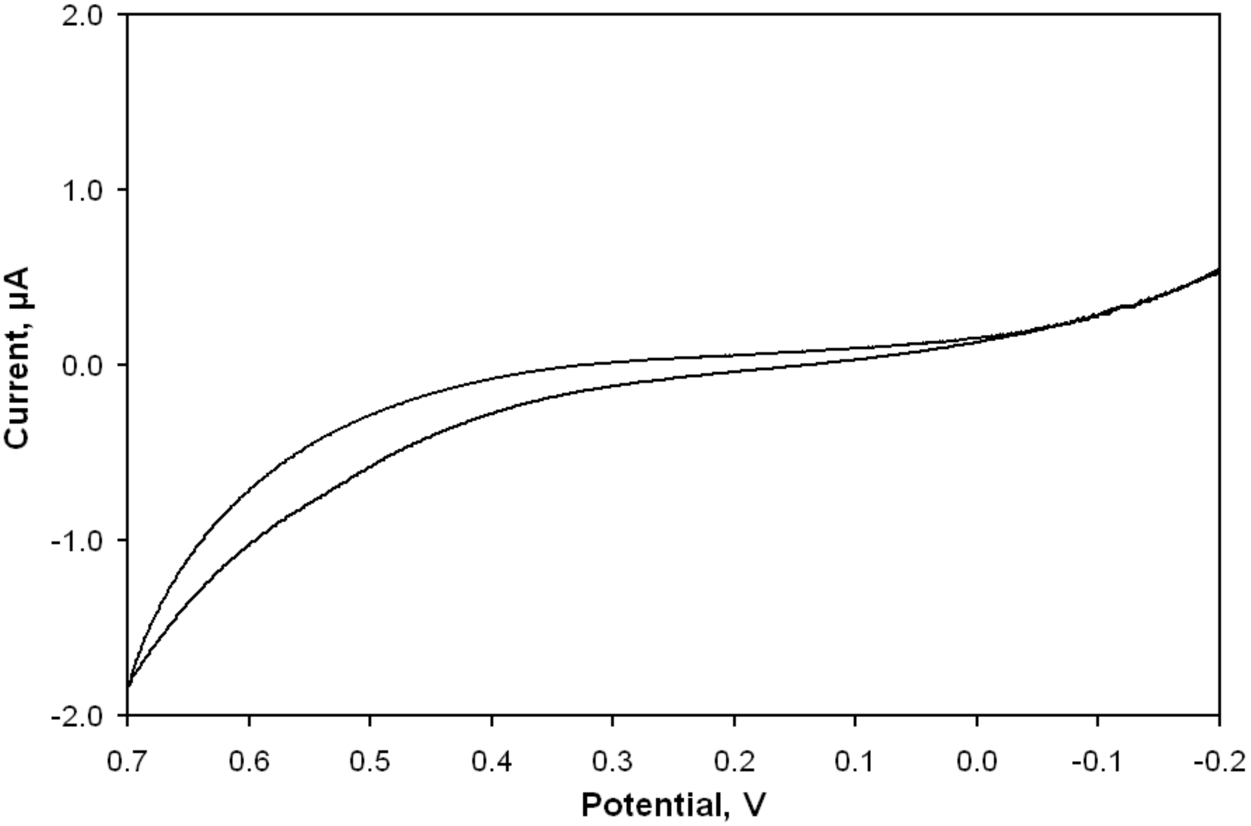

Figure 3.5 Current vs. Potential curve for cyclic voltammetry experiment for the oxidation of 0.005 M $Fe(CN)_6^{-4}$ solution in aqueous 0.10 M KCl at gold electrodes modified by immersion in 0.001 M *n*-dodecanethiol solutions. The cyclic voltammetry scan rate was 0.050 V/sec.

Concentration, Method	CV Curve	ΔE_p (V)
0.001 M, CP	peak-shaped	0.309
0.010 M, CP	peak-shaped	0.343
0.025 M, CP	peak-shaped	0.473
0.001 M, Immersion	exponential	--

Table 3.3 Summary of cyclic voltammetry (CV) data for *n*-dodecanethiol monolayers prepared by contact printing (CP) and immersion methods.

Unlike the *n*-octadecanethiol system, the 0.025 M contact printed and 0.001 M solution adsorbed *n*-dodecanethiol monolayers have different CV shapes. This was the first indication of a possible chain length dependence on the quality of films produced from contact printing. The mid-range - *n*-dodecanethiol monolayer does not have the extensive lateral interactions of the longer *n*-octadecanethiol, thus it cannot be as efficient in blocking electron transfer. If the contact printed monolayers have lower surface coverages, the hydrocarbon chains will tilt to more oblique angles to interact with neighboring chains.[70] A shorter alkane chain may possibly leave more areas of bare gold exposed at defect sites where charge transfer can occur freely. Charge transfer resistances of *n*-dodecanethiol monolayers were estimated from impedance measurements.

As with the *n*-octadecanethiol monolayers, complex impedance plots for monolayers of *n*-dodecanethiol prepared by contact printing demonstrate that increasing the ink concentration markedly improved the charge transfer resistance from 4.4 kΩ to 50.2 kΩ. Monolayers prepared by solution adsorption had a significantly larger charge transfer resistance (1.49 MΩ) than even the contact printed monolayer prepared from a solution 25-times more concentrated. Figure 3.6 and Table 3.4 summarize the impedance data.

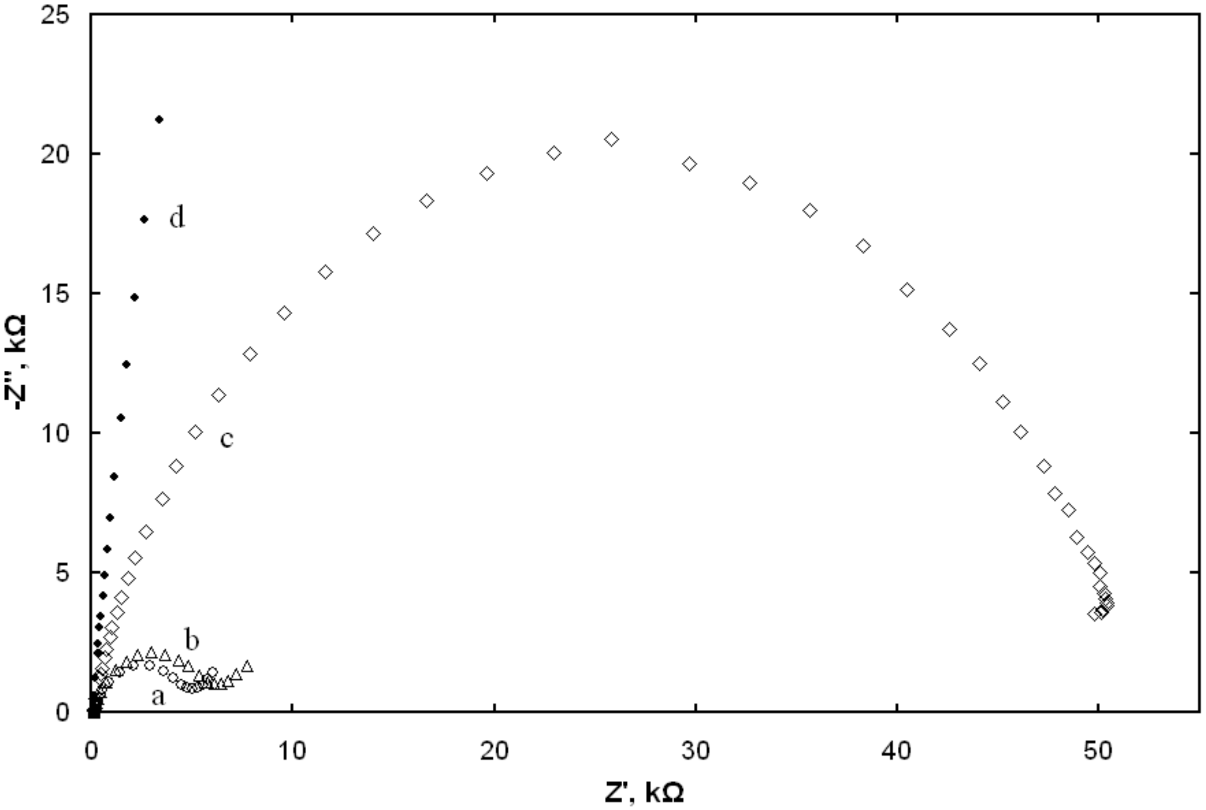

Figure 3.6 Complex impedance plots using 0.005 M $[Fe(CN)_6]^{-4/-3}$ redox probe at a gold electrode modified by contact printing with (a) 0.001 M *n*-dodecanethiol, (b) 0.010 M *n*-dodecanethiol, and (c) 0.025 M *n*-dodecanethiol and by immersion of the gold substrate in 0.001 M *n*-dodecanethiol solutions. Some data points have been excluded for clarity.

Concentration, Method	R_s (Ω)	R_{ct} (kΩ)	C_{dl} (µF)
0.001 M, CP	110±0	4.40±0.01	15.2±0.1
0.010 M, CP	110±1	5.44±0.04	16.1±0.3
0.025 M, CP	120±1	50.2±0.3	2.17±0.02
0.001 M, Immersion	120±2	1,490±32	1.52±0.02

Table 3.4 Summary of fitted equivalent circuit values of *n*-dodecanethiol monolayers prepared by contact printing (CP) and immersion methods.

The results of the estimated capacitance values of *n*-dodecanethiol monolayers generally follow those of *n*-octadecanethiol. The 0.001 M and 0.010 M contact printed SAMs have similar capacitance values at 15.2 and 16.1 µF, respectively. The slightly increased value for 0.010 M contact printed *n*-dodecanethiol does not directly follow the expected trend; this was somewhat irrelevant because the lower ink concentrations have very similar charge transfer resistances, thus it was expected that the capacitance values would be comparable. However, it was apparent that even at high ink concentration, the capacitance of 0.025 M contact printed *n*-dodecanethiol (2.17 μF) is larger than that found with monolayers prepared by solution adsorption (1.52 μF). The difference is characteristic of the structure of the monolayers at the interface and the increased presence of defects in contact printed SAMs.

3.2.3 n-Pentanethiol

After examining a very long chain alkanethiol and a mid-range alkanethiol, the next study considered monolayers formed from a short chain alkanethiol. *n*-Pentanethiol self-assembled monolayers are generally considered to be disordered because they lack sufficient lateral chain-chain interactions due to the small number of methylene units. *n*-Pentanethiol monolayers, therefore, have more facile charge transfer and have lower impedance. The characterization methods parallel those performed on the *n*-dodecanethiol monolayers.

Cyclic voltammetry measurements performed on *n*-pentanethiol monolayers prepared by contact printing and solution adsorption all produce peak-shaped curves. This result occurs because of the increased presence of defects in the short chain alkanethiol monolayer, independent of preparation method. Similar to the *n*-dodecanethiol monolayers, the peak separation of contact printed *n*-pentanethiol monolayers increases from 0.324 V to 0.504 V with increasing ink concentration used during preparation, Table 3.5. Qualitatively, the immersion formed *n*-pentanethiol monolayer blocks electron transfer better because it has the largest ΔE_p at 0.620 V. This is consistent with the previous findings from the studies with *n*-octadecanethiol and *n*-

dodecanethiol. The contact printed *n*-pentanethiol monolayers have more defects than the solution adsorbed monolayer because of the smaller peak separations.

Concentration, Method	CV Curve	ΔE_p (V)
0.001 M, CP	peak-shaped	0.324
0.010 M, CP	peak-shaped	0.485
0.025 M, CP	peak-shaped	0.504
0.001 M, Immersion	peak-shaped	0.620

Table 3.5 Summary of cyclic voltammetry (CV) data for *n*-pentanethiol monolayers prepared by contact printing (CP) and immersion methods.

The impedance results for the *n*-pentanethiol monolayers (Table 3.6) follow the same general trends observed with the *n*-octadecanethiol and *n*-dodecanethiol monolayers. The impedance increases with increasing concentration of *n*-pentanethiol used when preparing the contact printed monolayers; the monolayer prepared from a 0.025 M *n*-pentanethiol solution has the largest charge transfer resistance of the contact printed SAMs (10.7 kΩ). This charge-transfer resistance, however, is considerably smaller than the charge transfer resistance of the monolayer prepared by solution adsorption, 53.7 kΩ.

Concentration, Method	R_s (Ω)	R_{ct} (kΩ)	C_{dl} (µF)	Γ (nmol/cm^2)
0.001 M, CP	130±1	3.95±0.02	5.29±0.09	0.372
0.010 M, CP	130±1	7.42±0.04	2.45±0.05	0.581
0.025 M, CP	120±1	10.7±0.1	1.67±0.03	0.649
0.001 M, Immersion	120±3	53.7±0.8	1.19±0.04	0.866

Table 3.6 Summary of fitted equivalent circuit values and surface coverage measurements of *n*-pentanethiol monolayers prepared by the methods indicated. Resistance values in ohms, capacitance values in microfarads.

Unlike the longer alkanethiols, the 0.001 M solution adsorbed *n*-pentanethiol complex impedance plot has the typical semi-circular shape, Figure 3.7. This is because the *n*-

pentanethiol monolayer has fewer lateral interactions between methylene units, leading to more interfacial defects and decreasing the measured charge transfer resistance. Each of the *n*-pentanethiol layers exhibit a small Warburg impedance line. This arises at low frequency due to mass transfer effects.[13] Warburg lines typically occur when measuring the impedance of disordered systems.[9, 71, 72]

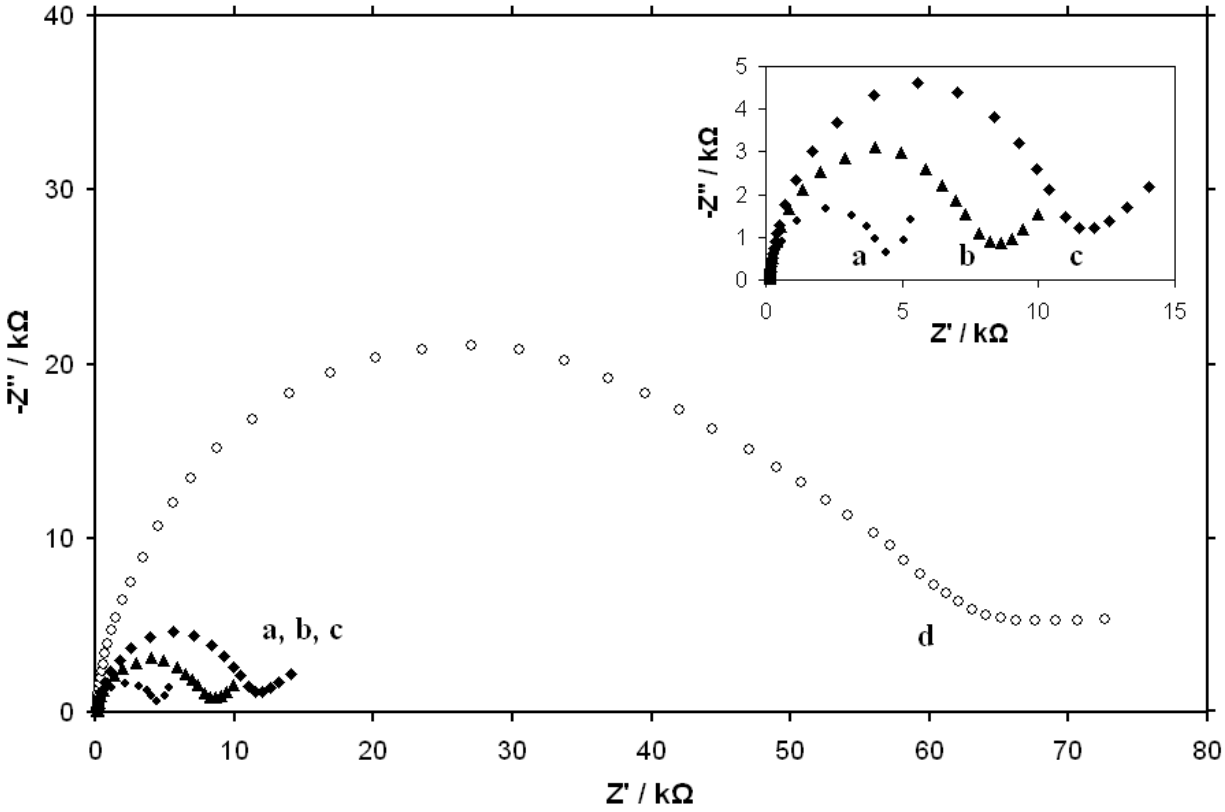

Figure 3.7 Complex impedance plots using 0.005 M $[Fe(CN)_6]^{-4/-3}$ redox probe at a gold electrode modified by contact printing with (a) 0.001 M *n*-pentanethiol, (b) 0.010 M *n*-pentanethiol, and (c) 0.025 M *n*-pentanethiol and by immersion of the gold substrate in 0.001 M *n*-pentanethiol solutions. The inset shows an expanded view of (a), (b), and (c). Some data points have been excluded for clarity.

Estimated capacitance values of *n*-pentanethiol monolayers are consistent with the trend presented with longer alkane chains. The contact printed *n*-pentanethiol monolayers decrease in capacitance from 5.29 to 1.67 μF with increasing ink concentration. As with the other systems, the higher ink concentrations improved the quality of the film, yet fell short of the capacitance observed for the solution adsorbed *n*-pentanethiol (1.19 μF). The higher capacitance values of the contact printed SAMs indicate the increased presence of defects and lower surface coverages.

Further evidence of the increased presence of defects in the contact printed *n*-pentanethiol SAMs arises from reductive desorption measurements. Reductive desorption is used to estimate the surface coverage of *n*-pentanethiol in the monolayer.[8] Because *n*-pentanethiol is a short chain alkanethiol with significantly decreased lateral interactions, the overpotential to desorb the chains fully was easily accessible unlike those of *n*-octadecanethiol and *n*-dodecanethiol. As with the previous findings, increasing the *n*-pentanethiol concentration used in contact printing yields more complete monolayers, as indicated by the trend in the surface coverage values (Table 3.6). The contact printed *n*-pentanethiol monolayers increase from 0.372 to 0.649 nmol/cm^2 when increasing the *n*-pentanethiol concentration from 0.001 M to 0.025 M; however, the highest coverage obtained with the contact printed monolayers (0.649 nmol/cm^2) remains lower than that found with the solution adsorbed monolayer (0.866 nmol/cm^2). These findings support the conclusion that contact printed monolayers, even with high ink concentrations, are not densely packed and have more defects than solution formed SAMs.

3.2.4 11-Mercaptoundecanoic Acid

The previous studies using *n*-alkanethiols found that the quality of self-assembled monolayer formed by contact printing depends on the concentration of the thiol solution used to ink the elastomeric stamp. Higher concentrations of thiol in the ink solution produced more complete monolayers with less defects. The following work determines the quality of monolayers formed by printing an ω-functionalized thiol, namely 11-mercaptoundecanoic acid (11-MUA). When placed in solutions of pH 7, the carboxyl group is deprotonatated and electrostatically repels a negatively charged redox probe.[73]

Cyclic voltammograms of 11-mercaptoundecanoic acid monolayers (Figure 3.8) continue to support the dependence of monolayer quality on thiol ink concentration. The CV of 0.001 M contact printed 11-MUA is peak-shaped with a peak separation of 184 mV. The large peak separation deviates from Nernstian behavior which indicates the presence of adsorbed molecules, however it is not a complete monolayer. Using concentrations of 0.010 and 0.025 M to print 11-MUA, the CV curves show only the anodic peak resulting in the oxidation of ferrocyanide, $Fe(CN)_6^{-4}$. This could be a result of the diffusion of newly oxidized ferricyanide, $Fe(CN)_6^{-3}$, away from the interface because of electrostatic repulsion. Cyclic voltammograms of the contact printed 11-MUA SAMs differ from the 0.001 M immersion formed monolayer. The exponential shape indicates a well-formed monolayer with minimal contributions to the observed current from the presence of defects. This result indicates that the functionality of an alkanethiol influences the quality of monolayer produced by contact printing.

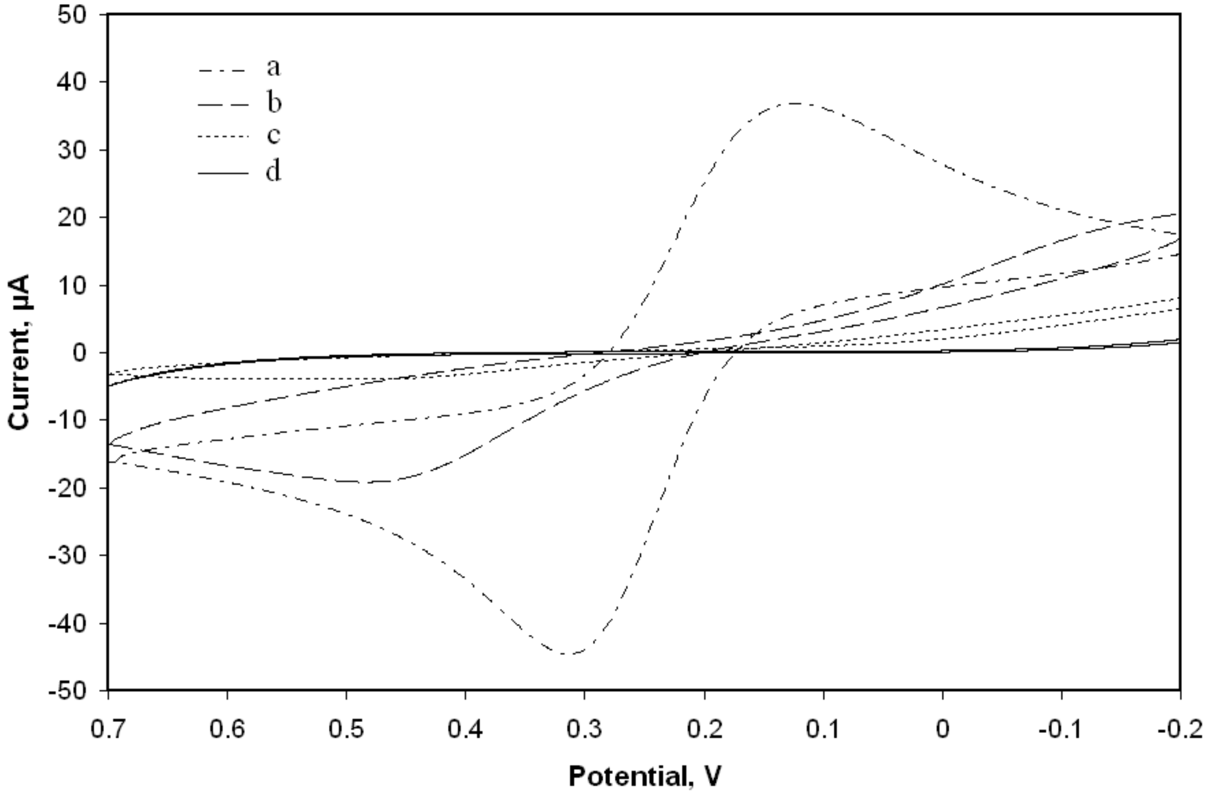

Figure 3.8 Current vs. Potential curves for cyclic voltammetry experiments for the oxidation of 0.005 M Fe(CN)$_6^{-4}$ solutions in aqueous 0.10 M KCl at gold electrodes modified by contact printing with (a) 0.001 M, (b) 0.010 M, and (c) 0.025 M 11-mercaptoundecanoic acid and by immersion in 0.001 M 11-mercaptoundecanoic acid solutions. The cyclic voltammetry scan rate was 0.10 V/sec.

Charge transfer resistance values were determined for self-assembled monolayers of 11-mercaptoundecanoic acid by fitting complex impedance plots. The equivalent circuit values are compiled in Table 3.7. Once more, increasing the concentration of thiol in the ink solution increases the observed charge transfer resistance. The impedance data of 0.001 M contact printed 11-MUA could not fit using the Randles circuit model; therefore estimates were made from the complex impedance plot. The data was difficult to fit because of the very low charge transfer resistance (650 Ω), and the presence of a large Warburg impedance line. A vast improvement in the charge transfer resistance was found with an 10-fold increase in the ink concentration at 21.5 kΩ, and it progressed to 106 kΩ using 0.025 M 11-MUA. Comparing these charge transfer resistances to the solution adsorbed SAM of 11-MUA (2.77 MΩ), it is apparent that the contact printed SAMs have a higher density of defects where electron transfer can occur freely. The magnitude of the charge transfer resistance for the 0.001 M 11-MUA solution adsorbed SAM is larger than R_{ct} for the equivalent monolayer using *n*-dodecanethiol (1.49 MΩ), a methyl terminated SAM of comparable chain length. The larger R_{ct} values of 11-MUA are a result of the electrostatic repulsion between the terminal carboxylate groups and the negative redox probe. Not only does the 11-MUA SAM insulate the electrode it also repulses the redox probe which in turn yields the high R_{ct} values observed.

Concentration, Method	**R_s (Ω)**	**R_{ct} (kΩ)**	**Fitted C_{dl} (μF)**	**Extrapolated C_{dl} (μF)**	**Γ (nmol/cm^2)**
0.001 M, CP	157§	0.650§	--	109	0.311±0.008
0.010 M, CP	130±3	21.5±0.3	4.21±0.16	4.89	0.619±0.033
0.025 M, CP	142±2	106±1	4.46±0.07	5.78	0.669±0.015
0.001 M, Immersion	153±2	2,770±110	2.78±0.03	3.04	0.767±0.028

Table 3.7 Summary of fitted equivalent circuit values and surface coverage measurements of 11-mercaptodecanoic acid monolayers prepared by the methods indicated. §Unable to fit data, values estimated from impedance plot.

Double layer capacitance values were estimated by two different procedures and are compiled in Table 3.7. The first was by using the non-linear least squares (NLLS) fitting program (labeled "Fitted C_{dl}"), the second was by interpretation of the Bode impedance plot ("Extrapolated C_{dl}"). As described in Section 2.7.1, the double layer capacitance can be found by extrapolation of the linear portion of the log Z vs. log F plot, where Z is the total impedance in ohms and F is the frequency in Hz. The double layer capacitance is found using the *y*-intercept and the following equation:

$$|Z| = \frac{1}{C_{dl}}. \qquad \textbf{(3.1)}$$

The second procedure was performed to yield qualitative estimates for all concentrations of the contact printed 11-MUA SAMs for a complete comparison. The values differ because the capacitance is determined from the fitted data using the NLLS analysis, not the experimental data. The capacitance of 0.001 M contact printed 11-MUA (109 μF) was expected to be significantly larger than the others due to the small R_{ct}. This is reasonable because the 0.001 M CP monolayer has a significant amount of defects which allows the redox probe to approach the electrode unhindered, decreasing the interplate distance, and in turn increasing the capacitance. As expected higher ink concentrations used for contact printed monolayers decreased the capacitance values. The capacitance of the 0.025 M contact printed monolayer (4.46 μF) continued to be larger than the solution adsorbed SAM (2.78 μF) just like with the *n*-alkanethiols. The discrepancy in the decline of capacitance for contact printed monolayers with increasing 11-MUA ink concentrations is due to the non-ideal behavior of monolayer modified interfaces as capacitors.[74] Either way, it is apparent that contact printed ω–functionalized monolayers exhibit higher capacitance, indicating a higher degree of defects.

Reductive desorption measurements were obtained with 11-MUA monolayers, unlike *n*-dodecanethiol, because the bulky terminal carboxyl group destabilizes the monolayer and prevents densely packed structures.[75] Reductive desorption measurements of 11-MUA monolayers reveal analogous findings to those of *n*-pentanethiol. Contact printed SAMs of 0.001 M 11-MUA have very low surface coverages at 0.311 nmol/cm^2, which is less than 50% of the expected value for a full monolayer. The maximum surface coverage for a contact printed SAM (0.669 nmol/cm^2) was obtained using a 0.025 M 11-MUA ink solution; however, this value was still less than the surface coverage of an immersion formed SAM of 11-MUA (0.767 nmol/cm^2).

It has been proposed that self-assembled monolayers of 11-mercaptoundecanoic acid are not configured in the hexagonal ($\sqrt{3} \times \sqrt{3}$)$R30°$ structure, but rather a double-row adlayer.[76] Others have seen this type of behavior for functionalized SAMs in which hydrogen bonding between the headgroups was the predominant factor.[77] While the hydrogen bonding may occur during deposition, when placed into pH 7 buffered solution the interfacial carboxyl group deprotonates.[73] The resulting electrostatic repulsion between the terminal groups also impacts the overall structure. The 0.001 M contact printed 11-MUA monolayer was the poorest formed monolayer of all those evaluated; this result implicates that higher concentrations of thiol ink are necessary to form more complete monolayers of ω-functionalized alkanethiols. The functional group may play a pivotal role in quality of monolayer formed.

3.2.5 Determination of Defect Density Using the Finklea Analysis

The previous discussions provide evidence that contact printed self-assembled monolayers have more interfacial defects than monolayers formed by solution adsorption. Electrochemical impedance spectroscopy was the most sensitive of the characterization methods to the influence of these defect sites. The results showed that the impedance of contact printed monolayers was consistently lower than the impedance of solution adsorbed monolayers, indicating an increased presence of defects which lowers the charge transfer resistance. This data can be used to estimate the defect density of the prepared monolayers.

Amatore *et al.* developed a model for describing an array of microelectrodes[78], which has since been applied to estimating defect size, density, and distribution of monolayer-modified electrodes.[25, 26, 69, 71, 79] In this model it is assumed that the pinholes are 1) disk-shaped and 2) evenly distributed throughout the monolayer.[69, 78] The surface coverage θ can be estimated as

$$\theta = 1 - \frac{\sigma_w}{m - \sigma_w}, \tag{3.2}$$

where σ_w is the Warburg coefficient and m is the slope at high frequency from a Z' vs. $\omega^{-1/2}$ plot of the modified electrode.[71] The Warburg coefficient is determined in the same manner, but the slope is derived from the low frequency response of a bare Au electrode. Amatore's model holds for surface coverages close to 1 ($\theta > 0.9$).

The defects, or pinholes, within a self-assembled monolayer have been described as an array of microelectrodes due to the fact that tiny areas of bare gold are exposed between vast regions of insulating material (i.e. the monolayer).[25] The pinhole fraction is expressed as

$$1 - \theta = \frac{r_a^2}{r_b^2}, \tag{3.3}$$

where r_a is the pinhole radius and r_b is the distance between pinholes as in Figure 3.9.

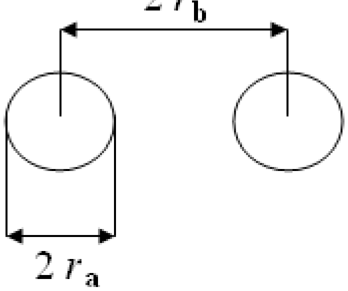

Figure 3.9 Illustration of pinhole model, where r_a and r_b are the radius of the pinholes and separation distance, respectively.

The transition radial frequency q is determined from the maximum in the Z” vs. $\omega^{-1/2}$ plot as

$$\omega = \frac{q}{2}, \tag{3.4}$$

where ω is the angular frequency. The transitional frequency is then used to directly estimate the pinhole radius, r_a, in the equation:

$$q = \frac{D}{0.36 r_a^2}, \tag{3.5}$$

where D is the diffusion coefficient of the redox couple (7.6 x 10^{-6} cm^2 s^{-1}).[80] Equation 3.3 is used to find the distance between pinholes.

The size and density of the defects are estimated for the contact printed alkanethiol monolayers using the Amatore model[78] as described by Finklea.[25] These data are summarized in Table 3.8. Similar to the findings of Diao,[69] we find that the pinhole radii do not change significantly for the contact printed monolayers prepared using different solution concentrations. The distance between defects, however, changes dramatically. For the contact printed *n*-octadecanethiol monolayers prepared with 0.025 M ink solutions, the defects are spaced at 26.5 μm. This is compared with a spacing of 7.3 μm for contact printed monolayers prepared with 0.010 M *n*-octadecanethiol, and 5.9 μm for 0.001 M contact printed *n*-octadecanethiol. This result suggests that monolayers prepared by contact printing using higher concentration solutions have fewer defects, generally consistent with the RAIRS and CV data. Based on the trend in the impedance data, we anticipate that monolayers of *n*-octadecanethiol prepared by solution adsorption would have even greater spacing of the defects. This deduction, however, is inconsistent with the conclusion based on infrared and cyclic voltammetry data that contact printed monolayers using higher concentrations solutions are structurally similar to monolayers prepared by solution adsorption. The infrared spectroscopy and cyclic voltammetry measurements provide an average of the interfacial structure and behavior, whereas the impedance measurement is sensitive to the effects of all types of defects and highlights the structurally differences between preparation methods.

Concentration (M) of thiol, and preparation method	r_a (µm)	r_b (µm)
0.001 M *n*-octadecanethiol, CP	1.27	5.94
0.010 M *n*-octadecanethiol, CP	1.39	7.25
0.025 M *n*-octadecanethiol, CP	3.00	26.5
0.001 M *n*-octadecantiol, Immersion	--	--
0.001 M *n*-dodecanethiol, CP	2.23	10.9
0.010 M *n*-dodecanethiol, CP	2.72	13.6
0.025 M *n*-dodecanethiol, CP	3.63	49.8
0.001 M *n*-dodecanethiol, Immersion	--	--
0.001 M *n*-pentanethiol, CP	1.50	12.8
0.010 M *n*-pentanethiol, CP	1.39	16.9
0.025 M *n*-pentanethiol, CP	1.39	20.3
0.001 M *n*-pentanethiol, Immersion	3.00	63.4
0.001 M 11-MUA, CP	0.71	2.21
0.010 M 11-MUA, CP	3.00	27.1
0.025 M 11-MUA, CP	9.50	117
0.001 M 11-MUA, Immersion	--	--

Table 3.8 Summary of the estimated pinhole radii, r_a, and pinhole separation distance, r_b, for the different preparation conditions of monolayers of *n*-octadecanethiol, *n*-dodecanethiol, *n*-pentanethiol, and 11-mercaptodecanoic acid (11-MUA).

We were unable to quantitatively estimate the defect size and density of the solution-adsorbed monolayers because the large impedance of the *n*-octadecanethiol monolayer prevented sufficient definition in the complex impedance plot to apply the Finklea model. The determination of the transitional frequency from the -Z" vs. $\omega^{-1/2}$ is nearly impossible because there is no clearly defined maximum. Figure 3.10B demonstrates this difficult issue. The inability to use this model for immersion formed *n*-octadecanethiol monolayers is similar to the conclusion of Diao *et al.* who also find that the Finklea model fails for monolayers formed by solution adsorption for more than a couple of hours.[69]

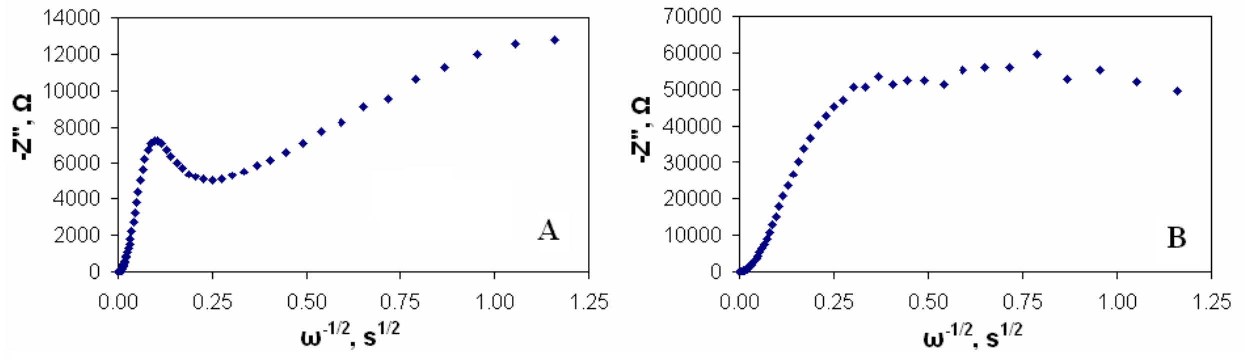

Figure 3.10 –Z" vs. $\omega^{-1/2}$ plots obtained at *n*-octadecanethiol modified gold electrodes in 0.005 M $Fe(CN)_6^{-4/-3}$ solutions in aqueous 0.10 mole/L KCl. Electrodes were modified by (A) contact printing with 0.025 M *n*-octadecanethiol and (B) immersion of the gold substrate in 0.001 M *n*-octadecanethiol solutions.

As with the *n*-octadecanethiol monolayers, the size of the defects does not change significantly with changes in the concentration of the solution used for the contact printing (2.23 µm to 3.63 µm). However, the distance between the defects increases as the concentration of the solution used to prepare the monolayers increases (10.9 µm to 49.8 µm). Again, we were unable to apply the Finklea model to estimate the average size and density of defects for the solution adsorbed *n*-dodecanethiol monolayer because of the high impedance measured for these monolayers.

In order to directly compare the defect density of contact printed and solution adsorbed monolayers, a short chain alkanethiol was examined. The Finklea method of quantifying the defect size and distribution was applied to the *n*-pentanethiol monolayers and the results are compiled in Table 3.8. As with monolayers prepared with *n*-octadecanethiol and *n*-dodecanethiol, the calculated pinhole radius is relatively constant (~1.4 µm) for each of the contact printed *n*-pentanethiol monolayers, while the pinhole separation increases for the monolayers prepared using higher concentration solutions (changing from 13 μm to 20 μm). Although larger than those prepared by contact printing, the complex impedance plot of solution adsorbed *n*-pentanethiol has sufficient definition to allow estimation of the size and density of the monolayer defects using the Finklea method. From this analysis, we find that the pinholes are spaced much further away than found with the contact printed monolayer prepared with 0.025 M solution (63 μm for the solution adsorbed monolayer compared with 20 μm for the contact printed monolayer). Comparing the quantitative estimates of defect size and density, it is clear that the size of the defects stays relatively constant for alkanethiol monolayers regardless of the preparation method, but the density of the defects changes with the different preparation conditions.

The pinhole analysis for 11-mercaptoundecanoic acid monolayers differs from the alkanethiol monolayers in pinhole diameter, yet the same general trend in defect density is observed. The size of the pinholes in contact printed 11-MUA monolayers clearly increases with increased ink concentration used to print (0.71 μm for 0.001 M, 3.00 μm for 0.010 M, and 9.50 μm for 0.025 M); the pinhole radius of alkanethiol monolayers were relatively constant. The pinhole separation distance grows more rapidly with higher concentrations of thiol ink than the alkanethiols—an increase from 2.21 μm to 117 μm for 11-MUA compared with 10.9 μm to 49.8 μm for *n*-dodecanethiol. We believe that the terminal carboxylate group of 11-mercaptoundecanoic acid monolayers is the reason for the observed differences. The pinhole analysis results reflect the significant changes in charge transfer resistance observed for the contact printed 11-mercaptoundecanoic acid monolayers. The charge transfer resistance of

0.001 M contact printed 11-MUA was very low (650 Ω), and the pinhole data confirms the high defect density with small pinholes spaced closely together. The 0.025 M contact printed monolayer showed high impedance with a charge transfer resistance of 106 kΩ; the defects are large yet sparsely distributed. The high pinhole radius is likely due to the presence of collapsed sites in the monolayer where lower charge transfer occurs more readily than at well-ordered domains. Like with *n*-dodecanethiol and *n*-octadecanethiol solution adsorbed monolayers, the pinhole analysis could not be applied to solution adsorbed 11-mercaptoundecanoic acid because of the high impedance.

3.3 Conclusions

Although infrared spectroscopy and cyclic voltammetry suggest that using relatively high concentrations of *n*-alkanethiols produces monolayers that are structurally similar to those prepared by 24-hour solution adsorption, impedance spectroscopy clearly shows that monolayers prepared by contact printing have a higher density of defects than those prepared by solution adsorption. Using the Finklea model, the size and separation of defects are determined for *n*-octadecanethiol, *n*-dodecanethiol, and *n*-pentanethiol monolayers. For *n*-alkanethiol monolayers prepared with each of these mercaptans, the size of the defects stays relatively constant regardless of the preparation conditions. The distance between defects increases as the concentration of the *n*-alkanethiol used to prepare the contact printed monolayers increases. With even the highest concentration of *n*-alkanethiol used, however, the spacing between defects is still smaller than found with monolayers prepared by solution adsorption. The pinhole analysis for monolayers of 11-mercaptoundecanoic acid follow the same general trend in defect density with slight deviations due to electrostatic repulsion between the terminal group and redox probe in solution.

Self-assembled monolayers form well-ordered systems because of the two-step adsorption process. It is believed that the monolayers form initially by nucleation, followed by growth of adjacent groups of ordered domains of *n*-alkanethiols until they coalesce, forming domain boundaries.[18, 81] These domain boundaries are potentially defects that may influence the electrochemical behavior of the modified interface. The quick adsorption is followed by a long period of reorganization in which defect sites move and group together, and this process decreases the density of defects along the modified interface. Low concentrations of *n*-alkanethiol are used during the immersion method to allow for this reorganization.[1] Decreasing the adsorption time, therefore, increases the defects present at the interface because it does not allow enough time for the monolayer reorganization. This behavior was demonstrated by Diao.[69] Because of the shortened time frame used when forming the monolayers by contact printing, reorganization of the molecules that comprise the monolayer does not occur; therefore, the monolayer structure does not have the opportunity to reorganize in order to minimize the defects present along the interface.

The ability of *n*-alkanethiol monolayers to passivate interfaces is an attractive property of self-assembled monolayers that many want to leverage when generating modified interfaces that are purposefully patterned over large areas. When forming interfacial patterns, *n*-alkanethiol molecules are frequently used to create vast domains where the interface is passivated so that other regions of the pattern can isolate the interfacial activity to specific locations along an interface. When using contact printing to generate these patterns, however, the EIS results suggest these *n*-alkanethiol domains are not as defect-free as previously believed.

Chapter 4

Characterization of Patterned Contact Printed Self-Assembled Monolayers

4.1 Introduction

When forming a 2-dimensional interfacial pattern by adsorption of alkanethiols onto gold substrates the desired electrochemical properties of the modified interface are those of a homogeneous, solution adsorbed monolayer. However, even the most well-ordered self-assembled monolayers contain a small degree of defects, especially at domain boundaries where two nucleating thiol domains converge. Patterning an interface increases the number of defects within the monolayer by purposefully creating domain boundaries. If these domain boundaries are large enough, the activity of these areas can dominate the electrochemical response. The work presented in this chapter describes the electrochemical behavior of patterned, contact printed self-assembled monolayers.

In Chapter 3, study of homogeneous contact printed monolayers revealed that high concentrations of thiol ink (0.025 M) produced films of the best quality (i.e. high charge transfer resistance, smaller defect density, etc.). For this reason, simple 2-dimensional interfacial patterns were formed by contact printing 0.025 M *n*-dodecanethiol in the desired motif, followed by placing the substrate in 0.001 M thiol solution to backfill any unmodified gold. Backfilling partial patterns is the most commonly used procedure to create heterogeneously patterned surfaces. However, there is recent work that employs stamping a substrate sequentially with different thiols in which adsorbates are selectively replaced by the newly printed molecules; this process is called microdisplacement printing.[82] The work presented in this chapter investigates if backfill molecules saturate defects within contact printed portions of the modified substrate.

Patterning an interface introduces yet another type of defect, termed the user-defined domain boundary, where printed domains converge with adsorbed domains of backfilled molecules. These areas are of considerable interest because they occur over a macroscopic range and impact the electrochemical properties of patterned interfaces. The effect of increased user-defined domain boundaries on the electrochemical response was examined.

Results from the homogeneous contact printed monolayers showed that electrochemical impedance spectroscopy was the most sensitive measure of the influence of defects. In this chapter, electrochemical impedance spectroscopy is used to evaluate patterned contact printed monolayers. Scanning electrochemical microscopy was also employed to image domain boundaries and heterogeneous patterned surfaces.

4.2 Experimental Details

4.2.1 Preparation of Binary Patterned Self-Assembled Monolayers

A poly(dimethylsiloxane) stamp was prepared using procedures from Section 2.3.2.2. The planar stamp was loaded with 0.025 M *n*-dodecanethiol solution for 2 minutes, dried under a stream of nitrogen, and used immediately. The stamp was positioned so that only half of the gold substrate was in direct contact with the stamp (Figure 4.1). The half-printed substrate was rinsed in ethanol, water, and dried with nitrogen gas.

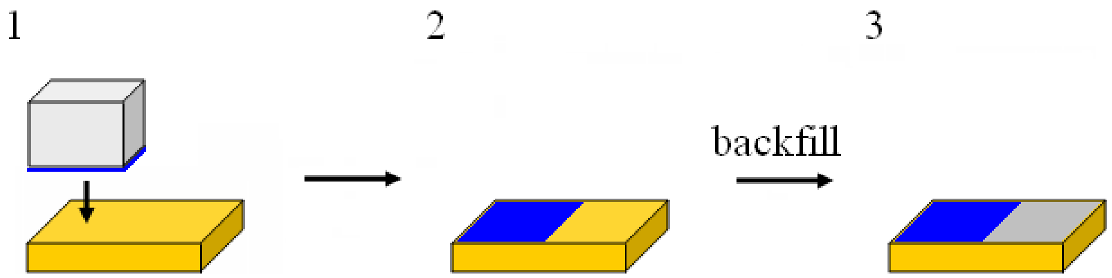

Figure 4.1 Scheme of the stamping process to create binary patterns with one user-defined domain boundary. The inked stamp of poly(dimethylsiloxane) is brought into contact with approximately half of a clean gold surface (1). The stamp is removed to reveal a half contact printed surface (2). The substrate is then placed in a backfill solution to modify the remaining gold (3). The user-defined domain boundary is the region where the contact printed portion meets the solution adsorbed domain.

The partially contact printed substrate (Figure 4.1, step 2) was then placed into a 0.001 M solution of either *n*-dodecanethiol or 11-mercaptoundecanoic acid for 15 minutes in order to backfill the remaining unmodified gold (Figure 4.1, step 3). The substrate was rinsed in ethanol, water, and dried prior to experiments.

The binary patterned monolayers (contact printed *n*-dodecanethiol/backfilled *n*-dodecanethiol and contact printed *n*-dodecanethiol/backfilled 11-mercaptoundecanoic acid) were compared to homogeneous solution adsorbed monolayers of *n*-dodecanethiol or 11-mercaptoundecanoic acid, respectively. Clean gold substrates were immersed in 0.001 M solutions of *n*-dodecanethiol or 11-MUA for 15 minutes, rather than the typical 18-24 hours. These short adsorption time monolayers are used in a direct comparison to the binary patterned monolayers formed by contact printing with 15 minute backfill time. The substrates were then rinsed in ethanol, followed by water, and dried in a stream of nitrogen gas prior to use.

4.2.2 Backfill Homogeneous Contact Printed n-Dodecanethiol Self-Assembled Monolayers

4.2.2.1 Backfill with *n*-Dodecanethiol

n-Dodecanethiol monolayers were prepared according to the procedures of Section 2.3.2.2 by using a 0.025 M *n*-dodecanethiol ink concentration. The stamp was contacted to the entire area of the gold substrate for 1 minute; the substrate was rinsed with ethanol, water, and dried with nitrogen gas. The contact printed monolayer was initially characterized by electrochemical measurements. The substrate was then rinsed and dried before placement in a 0.001 M solution of *n*-dodecanethiol for 15 minutes. The substrate was rinsed in ethanol, water, and dried prior to further characterization experiments.

4.2.2.2 Backfill in Pure Ethanol

n-Dodecanethiol monolayers were prepared according to Section 4.2.2.1. Briefly 0.025 M *n*-dodecanethiol was contact printed onto a clean gold substrate, then immersed in pure ethanol for 15 minutes. The monolayer was characterized before and after backfill modification.

4.2.2.3 Backfill with 11-Mercaptoundecanoic acid

As in the previous section, 0.025 M *n*-dodecanethiol contact printed monolayers were prepared according to Section 4.2.2.1. After initial characterization, the printed substrates were rinsed, dried, and placed into a 0.001 M solution of 11-mercaptoundecanoic acid for 15 minutes. The substrates were treated as previously described prior to experiments.

4.2.3 Preparation of Multi-Line Patterned Self-Assembled Monolayers

A master for stamp creation was prepared by ink-jet printing straight lines approximately one pixel apart onto a sheet of overhead paper. PDMS was allowed to cure for 2 days on the printed overhead master. The raised ink generated negative features on the stamp face (Figure 4.2, 1) which left facets of bare gold exposed when printed (Figure 4.2, 2). The stamps and monolayers were then prepared according to Section 2.3.2.2 with a *n*-dodecanethiol ink concentration of 0.025 M. The multi-line patterned *n*-dodecanethiol SAM was then placed in a 0.001 M solution of either *n*-dodecanethiol or 11-mercaptoundecanoic acid for 15 minutes to backfill any unmodified gold (Figure 4.2, 3).

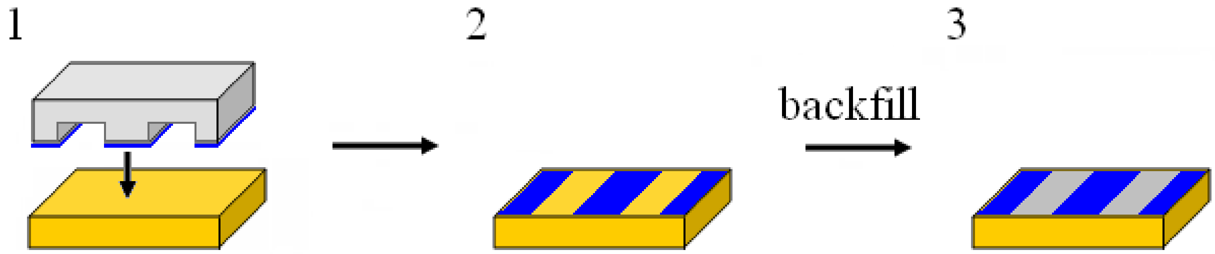

Figure 4.2 Scheme of the stamping process to create multi-line patterns with four user-defined domain boundaries. The stamp was inked and brought into contact with the gold (1). The patterned substrate (2) was rinsed and dried before placement into a backfill solution to modify any unprinted gold (3).

The multi-line patterned SAMs were compared to the binary patterned SAMs. While the binary patterned SAM has only one user-defined domain boundary, the multi-line patterned SAM has three to four, depending upon placement of the stamp on the substrate during monolayer preparation.

4.2.4 Experimental Conditions of Electrochemical Measurements

4.2.4.1 Electrochemical Impedance Spectroscopy

Electrochemical impedance measurements were conducted in solutions of 0.005 M $[Fe(CN)_6]^{-3/-4}$ or $[Ru(NH_3)_6]^{+2/+3}$ in 0.1 M KCl buffered to pH 7. Measurements were performed by applying an AC potential having a 5 mV amplitude that is symmetric about the formal potential of the redox probe (0.2 V vs. Ag/AgCl for $[Fe(CN)_6]^{-3/-4}$ or -0.2 V vs. Ag/AgCl for $[Ru(NH_3)_6]^{+2/+3}$). The frequency range was 1.0×10^5 Hz to 0.1 Hz. Quantitative estimates of the equivalent circuit elements were obtained by fitting the experimental data to a Randles equivalent circuit using the nonlinear least squares fitting routines provided by LEVM 7.0.

4.2.4.2 Reductive Desorption

Reductive desorption measurements were conducted in 0.5 M potassium hydroxide. The potential was swept from 0 to -1.3 V versus a saturated Ag/AgCl reference electrode at a rate of 50 mV/s. All solutions were degassed with N_2 for 5 minutes prior to measurement.

4.2.4.3 Scanning Electrochemical Microscopy

Images were obtained in either 0.005 M $[Fe(CN)_6]^{-4}$ or 0.005 M $[Ru(NH_3)_6]^{+3}$ in 0.1 M KCl and pH 7.0 phosphate buffer. Using ferrocyanide the bias potentials were 0.6 V and -0.1 V for the platinum ultramicroelectrode and gold substrate, respectively. The ruthenium hexaammine redox probe required bias potentials of -0.5 V and 0.0 V for the platinum and gold electrodes, respectively. Potentials are referenced to a Ag/AgCl reference electrode. Images were obtained in feedback mode.

4.3 Results and Discussion

4.3.1 Effect of One User-Defined Domain Boundary

A binary patterned monolayer of contact printed *n*-dodecanethiol/backfilled *n*-dodecanthiol was qualitatively compared to a homogeneous contact printed *n*-dodecanethiol SAM and a solution adsorbed monolayer of *n*-dodecanethiol using electrochemical impedance spectroscopy, Figure 4.3. A patterned monolayer prepared using the same thiol was used to determine how the introduction of a single user-defined domain boundary impacts the characteristic electrochemical behavior independent of factors associated with making mixed monolayers. Mixed monolayers of two or more differing thiol molecules have been shown to change the interfacial properties because of chain length mismatches or end group functionality.[36, 60, 83] In order to eliminate these issues and focus only on the effect of user-defined domain boundaries, we decided to prepare the binary patterned monolayer by contact printing *n*-dodecanethiol and backfilling with *n*-dodecanethiol. From the complex impedance plots it is evident that the impedance response of the binary patterned *n*-dodecanethiol monolayer lies between the two homogeneous standards. The binary patterned SAM is directly compared to a solution adsorbed monolayer with an immersion time of just fifteen minutes. We wanted the deposition times to be consistent for the direct comparison of the monolayers prepared by different methods. Actually, the shortened deposition time for the solution adsorbed *n*-dodecanethiol monolayer does not negatively affect the quality of the monolayer because the charge transfer resistance (1.64 MΩ, Table 4.1) is similar to a *n*-dodecanethiol monolayer formed in solution for 24 hours (1.49 MΩ, Table 3.4). The shape of each of the plots indicate that the *n*-dodecanethiol monolayers efficiently block electron transfer at the interface. As with other highly insulating surfaces, the complex impedance plots of the binary patterned and solution adsorbed SAMs are not complete semi-circles due to the lower limitation of frequencies evaluated.

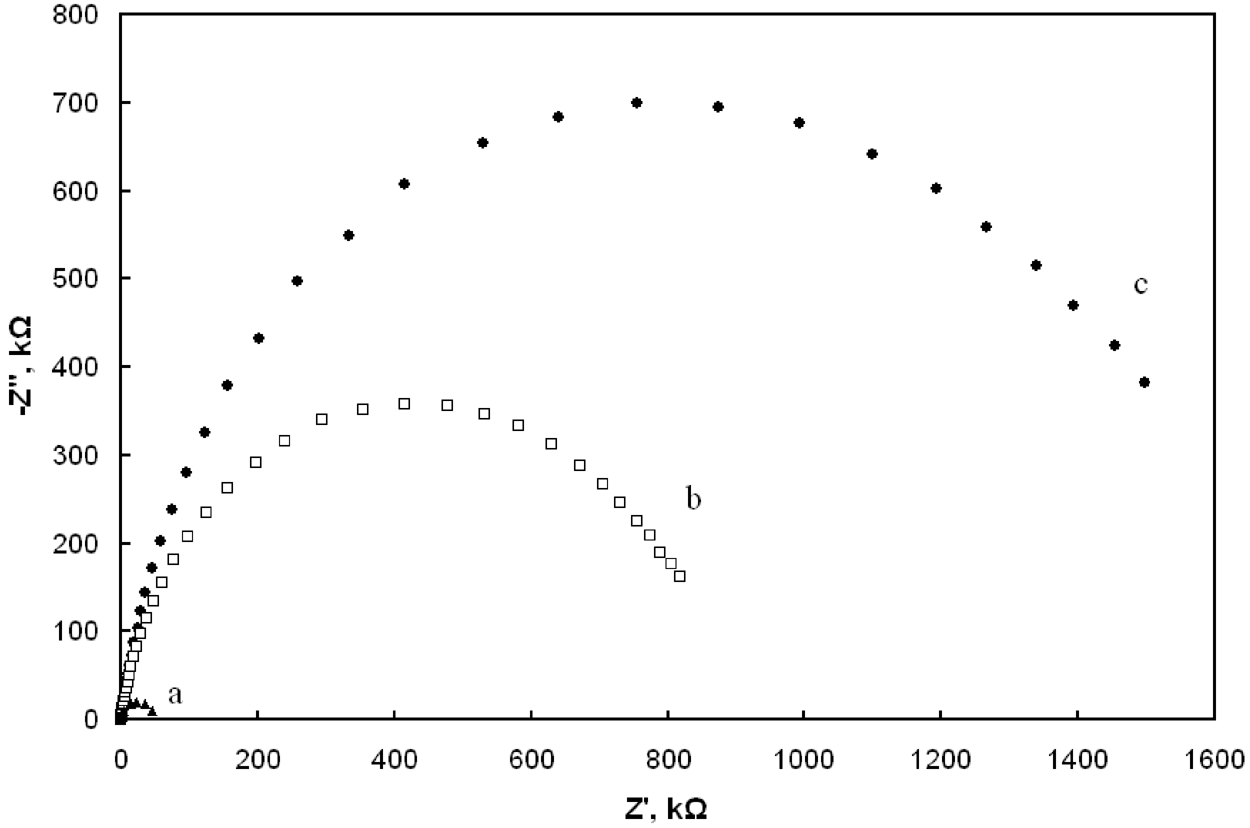

Figure 4.3 Complex impedance plots of (a) 0.025 M homogeneous contact printed *n*-dodecanethiol, (b) 0.025 M contact printed *n*-dodecanethiol + 0.001 M backfilled *n*-dodecanethiol binary pattern, and (c) 0.001 M adsorbed *n*-dodecanethiol. The redox probe was 0.005 M $[Fe(CN)_6]^{-4/-3}$.

Values from a theoretical equivalent circuit were fit to the experimental data for the binary patterned monolayers, and for monolayers prepared by standard contact printing and solution immersion are compiled in Table 4.1. These values indicate that the binary *n*-dodecanethiol monolayer is more similar to the solution adsorbed monolayer than to the contact-printed monolayer. While the binary *n*-dodecanethiol SAM has a charge transfer resistance of 855 kΩ (nearly 20 times larger than the homogeneous contact printed monolayer of 50.2 kΩ), it is only half as resistive as the immersion formed SAM (R_{ct} of 1,640 kΩ). The charge transfer resistance of the binary patterned SAM can vary due to the extent of the electrode area printed with *n*-dodecanethiol during sample preparation. A larger portion of contact printed *n*-dodecanethiol on the electrode would decrease the charge transfer resistance of a binary patterned SAM because of the increased defect density in the contact printed domain. It was shown in Chapter 3 that homogeneous contact printed SAMs have more defects and lower charge transfer resistance than solution adsorbed monolayers. In a second trial, the intermediate charge transfer resistance of a binary patterned *n*-dodecanethiol SAM was confirmed with a R_{ct} of 741 kΩ (data not shown), which is similar to the reported R_{ct} = 855 kΩ here.

Concentration Thiol, Method	**R_s (Ω)**	**R_{ct} (kΩ)**	**C_{dl} (μF)**
0.025 M *n*-dodecanethiol, CP	119±1	50.2±0.3	2.17±0.02
Binary Pattern of *n*-dodecanethiol	151±1	855±4	1.05±0.01
0.001 M *n*-dodecanethiol, Immersion	148±1	1,640±10	0.99±0.01

Table 4.1 Summary of fitted equivalent circuit values of binary patterned and standard *n*-dodecanethiol monolayers.

Double layer capacitance values decrease as the component of immersion formed *n*-dodecanethiol domains increases. The contact printed *n*-dodecanethiol monolayer has a capacitance of 2.17 μF, a value that is twice as large as the value for both the binary patterned monolayer (1.05 μF) and the immersion formed monolayer (0.99 μF); this result suggests the contact printed *n*-dodecanethiol monolayer has more interfacial defects than solution adsorbed monolayers as discussed in Section 3.2.2. The high charge transfer resistance and low capacitance values of the binary patterned and immersion formed SAMs indicate that their structures are more densely packed than the pure contact printed monolayer. The capacitance values also highlight the fact that the binary patterned *n*-dodecanethiol SAM is more structurally similar to the immersion formed monolayer than to the contact printed monolayer.

The Finklea analysis of pinhole size and distribution is not reported for the binary patterned *n*-dodecanethiol SAMs because of the large charge transfer resistance values observed. As with the solution adsorbed monolayers of long alkyl chain length, the model is not applicable for these well-ordered monolayers.[69] From this finding, we can infer that backfilling a patterned monolayer effectively decreases defect density by the saturation of pinholes within the contact printed domains with incoming solution molecules. The effects of the backfill procedure will be discussed in further detail in Section 4.4.

One would expect that the charge transfer resistance of an interfacial structure consisting of half contact printed *n*-dodecanethiol and half solution adsorbed *n*-dodecanethiol to have characteristics of both standard homogeneously prepared monolayers. Looking at the complex impedance plots, we do see this behavior from the binary SAM created by the combination of the two preparation methods. Even with the possibility of pinhole saturation during backfilling, the effect of the user defined domain boundary is apparent. The charge transfer resistance of the binary *n*-dodecanethiol SAM remains lower than the solution adsorbed standard. The more intricate a pattern, the more likely the resulting monolayers will contain significant defects. As high defect density is considered undesirable, the quality of patterned contact printed monolayers used for electrochemical applications is of great concern.

4.3.1.1 Binary Pattern of n-Dodecanethiol and 11-Mercaptoundecanoic Acid

One of the advantages of contact printing is the controlled introduction of functionalized thiols into predetermined regions across the interface. We wanted to understand how functionality affects a patterned mixed monolayer. This work studied the electrochemical properties of a binary patterned mixed-monolayer prepared by contact printing *n*-dodecanethiol and backfilling with 11-mercaptoundcanoic acid (see Figure 4.1 for the preparation process). As in Section 4.3, the binary patterned mixed SAM was compared to standard homogeneous monolayers using electrochemical impedance spectroscopy, Figure 4.4. The complex impedance plots of homogeneous contact printed *n*-dodecanethiol (Figure 4.4a) and solution adsorbed 11-mercaptoundecanoic acid (Figure 4.4c) were used for comparison.

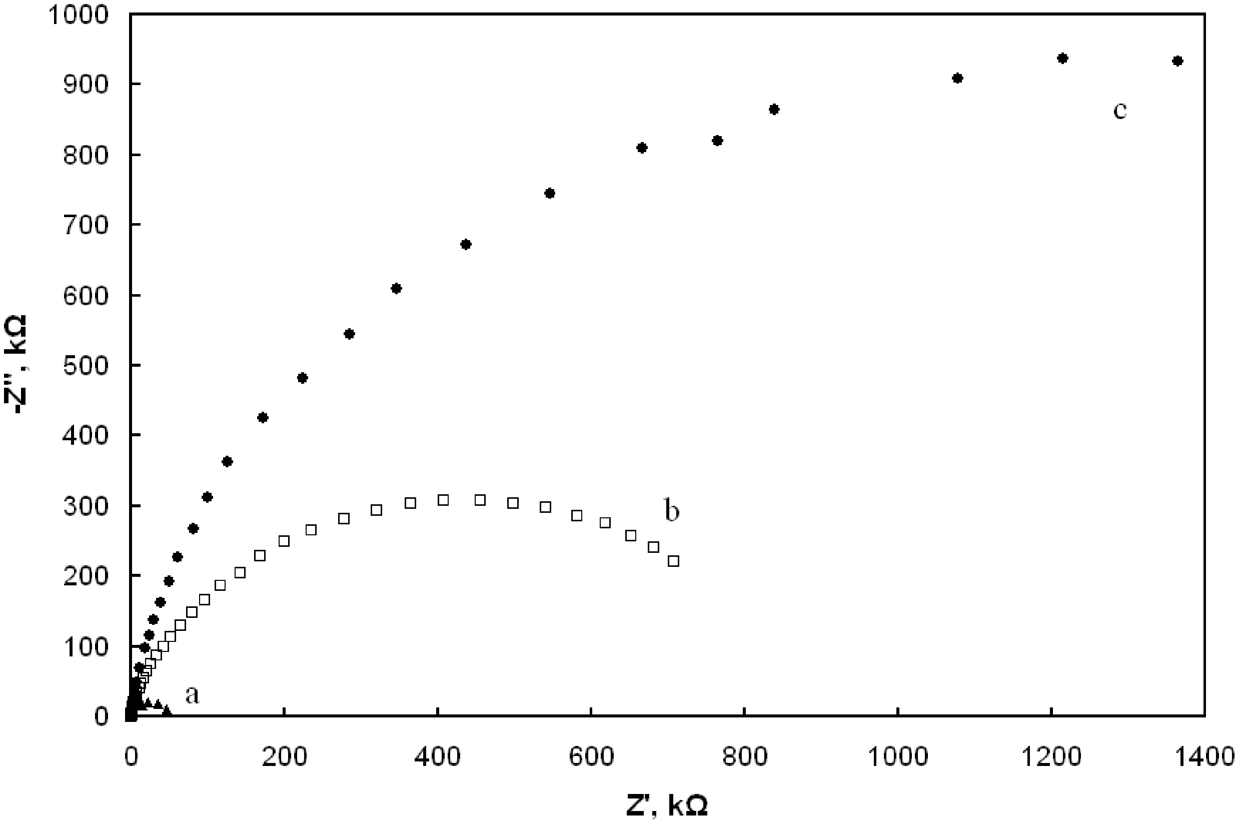

Figure 4.4 Complex impedance plots of (a) 0.025 M homogeneous contact printed *n*-dodecanethiol, (b) 0.025 M contact printed *n*-dodecanethiol + 0.001 M backfilled 11-mercaptoundecanoic acid binary pattern, and (c) 0.001 M adsorbed 11-mercaptoundecanoic acid. The redox probe was 0.005 M $[Fe(CN)_6]^{-4/-3}$.

The complex impedance plots of Figure 4.4 indicate that each monolayer, regardless of preparation, blocks electron transfer efficiently as demonstrated by the semicircular shape and lack of a Warburg impedance line at low frequency. The charge transfer resistance of 0.001 M solution adsorbed 11-mercaptoundecanoic acid is due to a combination of the insulating behavior of the alkyl chain and the electrostatic repulsion of the negative redox probe by the carboxylate terminal group in pH 7 solution used during the experiment. Like the binary *n*-dodecanethiol SAM of Section 4.2, the *n*-dodecanethiol/11-mercaptoundecanoic acid binary patterned SAM has a charge transfer resistance intermediate between the two homogeneous standards.

Summarized in Table 4.2 are the quantitative estimates of the equivalent circuit values fit to the above monolayers using the Randles model. Similar to the results of Chapter 3, the R_{ct} value of a fifteen minute solution adsorbed 11-mercaptoundecanoic acid monolayer is slightly greater than that of *n*-dodecanethiol prepared under the same conditions (2,000 kΩ compared to 1,640 kΩ, respectively). The higher impedance of 11-mercaptoundecanoic acid is attributed to electrostatic repulsion, as previously described. Immersion formed 11-mercaptoundecanoic acid is 2.5 times more resistive than the binary patterned *n*-dodecanethiol/11-mercaptoundecanoic acid monolayer with R_{ct} of 772 kΩ. This result concurs with the binary patterned *n*-dodecanethiol monolayer of the previous section: binary patterned monolayers are intermediate of the two homogeneous standard self-assembled monolayers.

Concentration Thiol, Method	**R_s (Ω)**	**R_{ct} (kΩ)**
0.025 M *n*-dodecanethiol, CP	119±1	50.2±0.3
Binary Pattern *n*-dodecanethiol/11-MUA	159±5	772±19
0.001 M 11-MUA, Immersion	148±1	2,000±23

Table 4.2 Summary of fitted equivalent circuit values of binary patterned and standard *n*-dodecanethiol and 11-mercaptoundecanoic acid monolayers.

Possible reasons for the lower charge transfer resistance of binary patterned *n*-dodecanethiol/11-mercaptoundecanoic acid versus binary patterned *n*-dodecanethiol are 1) a larger portion of the electrode was printed with *n*-dodecanethiol or 2) the phase separation at the user-defined domain boundary was significant. The former is a reasonable explanation because the area of contact printed *n*-dodecanethiol varied between trials due to a lack of mechanical reproducibility during printing. It was shown in Chapter 3 and here that well-organized monolayers of *n*-dodecanethiol present smaller impedance than those of 11-mercaptoundecanoic acid. A binary patterned monolayer of *n*-dodecanethiol/11-mercaptoundecanoic acid with a larger component of contact printed *n*-dodecanethiol would have a smaller charge transfer resistance than if the component ratios were reversed. The latter reason of phase separation is more complicated.

Phase separation of adsorbates into their homogeneous domains is noted when the components differ vastly in alkyl chain length and terminal group polarity when coadsorbed from solution.[84-86] In contrast, Kakiuchi et al. and Arnold et al. found that molecules of similar chain length but that differ in the ω-terminal group do not exhibit sizeable phase separation.[87, 88] *n*-Dodecanethiol and 11-mercaptoundecanoic acid differ in chain length by one methylene unit, therefore the resulting monolayers most likely would not exhibit phase separation if coadsorbed from solution. However, by contact printing *n*-dodecanethiol on half the electrode surface and backfilling with 11-mercaptoundecanoic acid we have generated a phase boundary that extends across the interface. In Section 4.2, it was evident that the user-defined domain boundary affected the overall impedance of the binary patterned *n*-dodecanethiol SAM, thus it is also believed to be a cause of the observed low charge transfer resistance of the binary patterned *n*-dodecanethiol/11-mercaptoundecanoic acid SAM here. A phase boundary that extends over the entire interface is a gross defect that allows the redox probe in solution access to the underlying gold electrode and yields low charge transfer resistance.

4.3.2 Effect of Backfilling Homogeneous Contact Printed Self-Assembled Monolayers

The work presented in section 4.3.1 showed that binary patterned self-assembled monolayers created by the combination of contact printing and backfill by solution adsorption have properties intermediate to that of homogeneous monolayers. From the electrochemical impedance spectroscopy results, it appeared the binary SAMs more closely resembled the behavior of solution adsorbed monolayers. It was also proposed that during the backfilling process, defects within the contact printed domains were saturated by the backfill molecules. Within this section, we investigate how the backfill solution impacts the overall electrochemical response.

4.3.2.1 Contact Printed *n*-Dodecanethiol in *n*-Dodecanethiol

The first method to determine if backfill molecules saturate pinhole defects within contact printed domains was to contact print a gold substrate and backfill with the same alkanethiol. Figure 4.3 illustrates the complex impedance plots of a 0.025 M homogeneous contact printed *n*-dodecanethiol monolayer (a) and the same monolayer after subsequently placing the electrode in 0.001 M *n*-dodecanethiol (b). While each film efficiently blocks electron transfer as evidenced by the semi-circular shape of the complex impedance plot, it is unmistakable that placing the contact printed substrate into a backfill solution of *n*-dodecanethiol increased the charge transfer resistance. Since alkanethiol molecules typically adsorb onto a gold surface within the first 100 seconds when immersed in solution,[89] it can be deduced that any unmodified gold, presented as defects within the contact printed monolayer, would be saturated by backfill molecules. In fact, Cimatu and Baldelli provide evidence using sum frequency generation microscopy that contact printed areas of alkanethiol molecules contain other molecules deposited during backfilling process.[90-92] The shortened backfill adsorption time of 15 minutes is sufficient to fill those defect sites. As the defect density is reduced, the monolayer structure appears more densely packed.

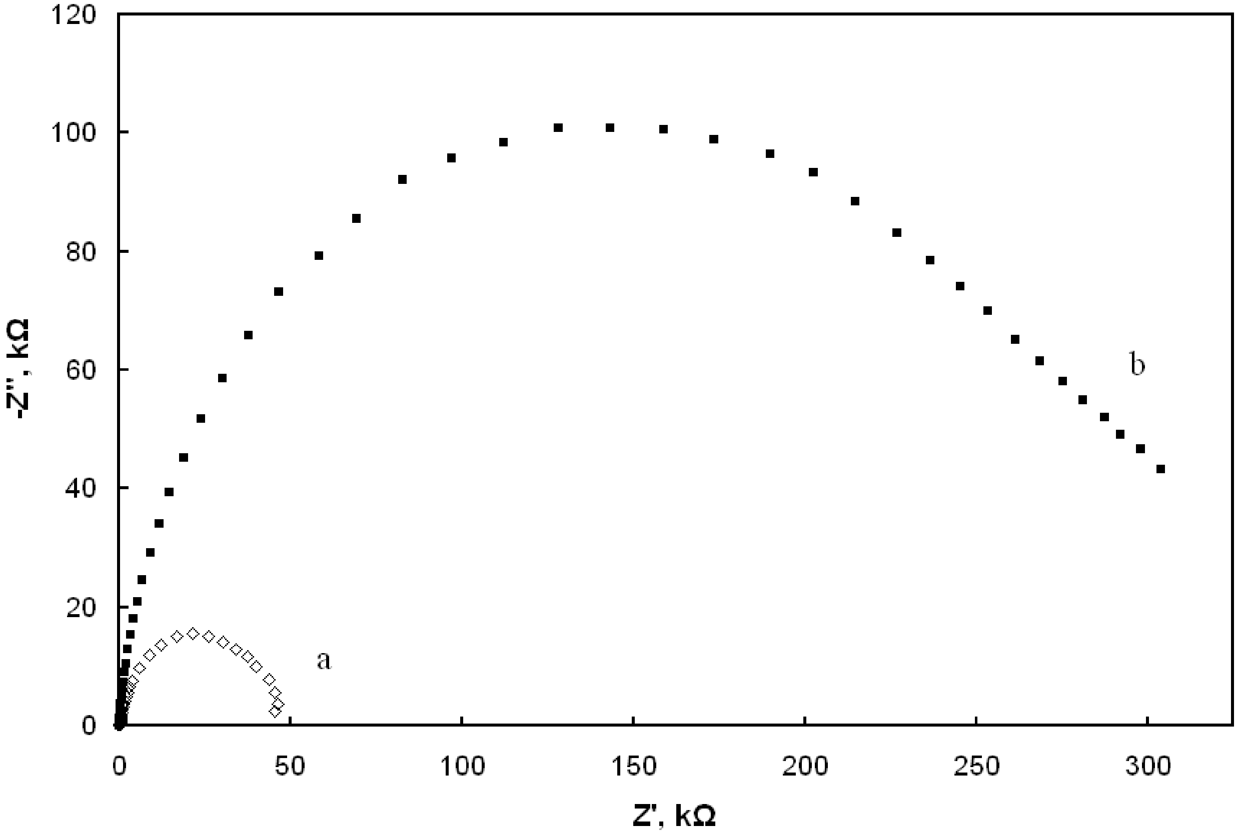

Figure 4.5 Complex impedance plots of (a) 0.025 M homogeneous contact printed *n*-dodecanethiol and (b) 0.025 M homogeneous contact printed *n*-dodecanethiol monolayer of (a) backfilled in 0.001 M *n*-dodecanethiol. The redox probe was 0.005 M $[Fe(CN)_6]^{-4/-3}$.

Equivalent circuit values fit to the impedance for the above monolayers are summarized in Table 4.3. The charge transfer resistance improved from 43.4 kΩ to 265 kΩ after backfilling in 0.001 M *n*-dodecanethiol. Estimates of the double layer capacitance support that denser monolayer structures are formed during backfilling by the observed decrease in capacitance. Contact printed *n*-dodecanethiol monolayers have a capacitance of 2.17 μF, whereas the capacitance of backfilled *n*-dodecanethiol is 1.07 μF. The more densely packed the monolayer, the larger the dielectric medium distance, and thus the smaller the capacitance.

Concentration Thiol, Method	**Assessment**				
	R_s (Ω)	**R_{ct} (kΩ)**	**C_{dl} (μF)**	**r_a (μm)**	**r_b (μm)**
0.025 M *n*-dodecanethiol, CP	150±2	43.4±0.5	2.17±0.06	3.30	56.1
0.025 M *n*-dodecanethiol, CP backfilled in 0.001 M *n*-dodecanethiol	155±3	265±4	1.07±0.02	7.12	214
0.001 M *n*-dodecanethiol, Immersion	148±1	1,640±10	0.99±0.01	18.6	565

Table 4.3 Summary of fitted equivalent circuit values and estimates of pinhole radius (r_a) and separation distance (r_b) of contact printed and backfilled *n*-dodecanethiol monolayers.

Defect density was quantified by application of the Amatore/Finklea analysis method to the impedance data. The 0.025 M contact printed *n*-dodecanethiol SAM was estimated to have pinholes of 3.30 μm radii separated by a distance of 56.1 μm; these values agree closely with those of chapter 3 for an equivalently prepared monolayer. The Finklea model works best for pinhole radii less than 10 μm and separation distances under 100 μm.[25] The pinhole estimates of the backfilled *n*-dodecanethiol monolayer and solution adsorbed monolayers are very large and almost inconceivable; however they are still useful for this discussion. The pinhole radius of backfilled *n*-dodecanethiol roughly doubles in size to 7.12 μm, and the pinhole separation distance increases by a factor of four to 214 μm. The large pinhole radius is most likely due to the increased effect of collapsed sites, rather than actual pinholes of exposed gold substrate.[26, 93] The significant increase in pinhole separation suggests a reduction of defect density. The size and spacing of pinhole defects in solution adsorbed *n*-dodecanethiol along with the high charge transfer resistance describe a monolayer essentially defect-free. Again, the large pinhole radius is due to collapsed sites within the monolayer. The change in defect density of the contact printed monolayer after backfill suggests restructuring of the monolayer during the backfill process.

4.3.2.2 Contact Printed *n*-Dodecanethiol in Pure Ethanol

The results of homogeneous contact printed *n*-dodecanethiol monolayers backfilled with *n*-dodecanethiol lead to a new question: are pinhole defects simply saturated or does the liquid environment allow the monolayer more mobility for possible interfacial restructuring? To determine if the monolayers reorganize during the backfilling process, homogeneous contact printed *n*-dodecanethiol substrates were placed into a solution of pure ethanol without any thiol present. The hypothesis is that the contact printed molecules become more mobile in the ethanol solution and have the opportunity to restructure. The two-step adsorption mechanism of mercaptans to gold begins with the initial quick adsorption, which occurs within the first 100 seconds,[34] followed by a slow second step where the monolayer consolidates and reduces defects.[81] Without any additional thiol present in the backfill solution, the monolayer can only perform the second step of the adsorption mechanism. Weakly bound thiolate molecules may desorb from the surface and either remain dissolved or readsorb in a more favored position. Reorganization of the contact printed monolayer would increase the area of exposed gold substrate and consequently decrease the observed charge transfer resistance.

Complex impedance plots of contact printed *n*-dodecanethiol before and after backfilling in pure ethanol are shown in Figure 4.4. Experimental results substantiate the proposed idea that contact printed thiolates reorganize when placed in a backfill solution by the decrease in charge transfer resistance. Pertinent values from the impedance data are summarized in Table 4.4, in which two separate experiments were averaged. The charge transfer resistance decreased by an average of 66.6 kΩ, indicative of higher density of defects. In fact, the pinhole radius of contact printed *n*-dodecanethiol decreases from 4.24 μm to 1.85 μm, and the pinhole separation distance changes from 101 µm to 38.6 µm. The sharp decrease in charge transfer resistance could also be attributed to loss of weakly bound *n*-dodecanthiolate molecules, most likely at defect sites, as the same phenomena occurs for solution deposited SAMs (data not shown).

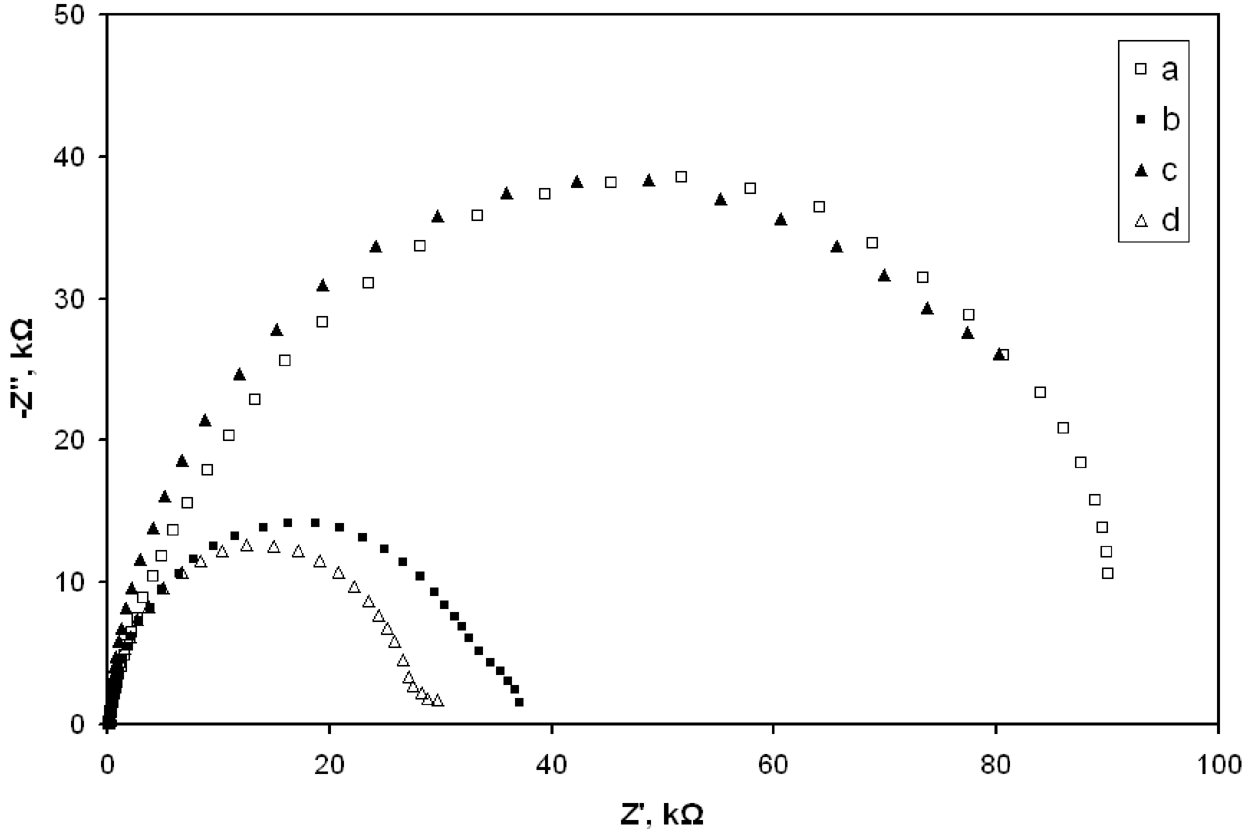

Figure 4.6 Complex impedance plots of (a,c) 0.025 M homogeneous contact printed *n*-dodecanethiol and (b,d) 0.025 M homogeneous contact printed *n*-dodecanethiol monolayer of (a and c, respectively) placed in pure ethanol. EIS conditions: 0.005 M $[Fe(CN)_6]^{-4/-3}$ in 0.1 M KCl of pH 7 at a potential 0.2 V vs. Ag/AgCl.

Concentration Thiol, Method	**Assessment**		
	R_{ct} (kΩ)	**r_a (µm)**	**r_b (µm)**
0.025 M *n*-dodecanethiol, CP	98.0±1.5	4.24±0.87	101±1
0.025 M *n*-octadecanethiol, CP backfilled in pure ethanol	31.4±4.9	1.85±0.28	38.6±4.2

Table 4.4 Summary of charge transfer resistance, pinhole radius (r_a), and pinhole separation distance (r_b) of contact printed *n*-dodecanethiol monolayers before and after placement in pure ethanol. Reported values are the average and standard deviation of two separate experiments.

4.3.2.3 Contact Printed *n*-Dodecanethiol in 11-Mercaptoundecanoic Acid

Reductive desorption was used to determine the extent to which backfill molecules saturate defects within contact printed films. This is accomplished by selective desorption of the backfill molecules. Homogeneous contact printed monolayers of *n*-dodecanethiol were placed in a backfill solution of 11-mercaptoundecanoic acid. Electrochemical impedance spectroscopy was used to measure charge transfer resistance before and after backfilling, and surface coverage of 11-MUA was determined by reductive desorption.

EIS measurements reveal an increase in total impedance after the 0.025 M contact printed *n*-dodecanethiol monolayer was placed in 0.001 M 11-mercaptoundecanoic acid for backfilling. The positive change in charge transfer is indicative of further adsorption of thiol at the electrode interface. This result supports those of Section 4.3.2.1 where backfill molecules were found to permeate the contact printed monolayer. The charge transfer resistance of homogeneous contact printed *n*-dodecanethiol increases from an average of 55±7 kΩ to 130±25 kΩ after backfilling. The difference in charge transfer varied from sample to sample; this was expected due to the variability in the quality of the initial contact printed film. It could also be due in part to the replacement of *n*-dodecanethiolate molecules with 11-mercaptoundecanoic acid; this explanation is discussed in detail later.

Even though *n*-dodecanethiol and 11-mercaptoundecanoic acid have essentially the same hydrocarbon chain length, the monolayers are desorbed from the gold surface at different potentials. 11-mercaptoundecanoic acid desorbs at a more positive potential due to the electrostatic repulsion of the carboxylate terminal groups in basic solution.[75] This unfavorable interaction makes it possible to selectively desorb 11-mercaptoundecanoic acid monolayers at an accessible overpotential; monolayers of *n*-dodecanethiol do not exhibit reduction peaks within the potential window examined. Figure 4.7 displays reductive desorption voltammograms of pure *n*-dodecanethiol (a) and 11-mercaptoundecanoic acid imbedded within contact printed *n*-dodecanethiol (b) being removed from a gold surface. The selective desorption of 11-mercaptoundecanoic acid yields a good estimate of the extent to which backfill molecules saturate defect sites.

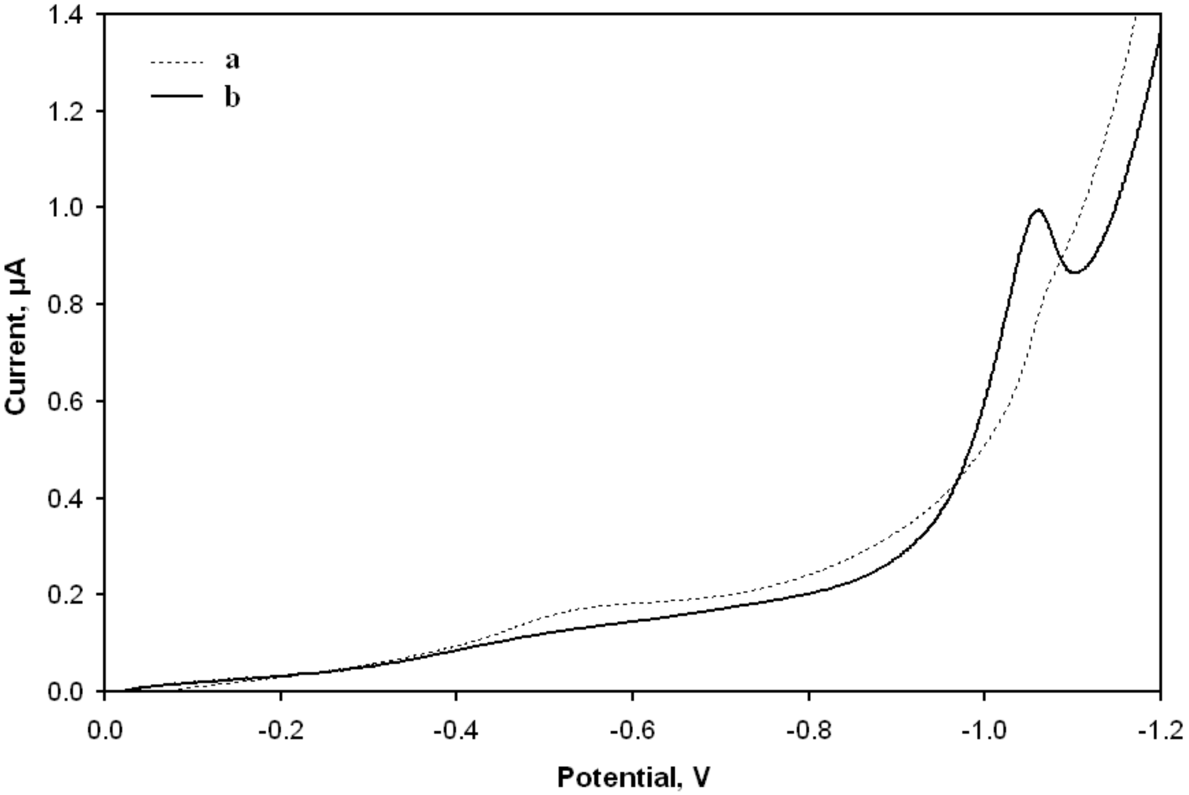

Figure 4.7 Linear sweep voltammograms of the reductive desorption of (a) *n*-dodecanethiol and (b) backfilled 11-mercaptoundecanoic acid within a contact printed *n*-dodecanethiol monolayer in deaerated solutions of 0.5 M KOH. Potential vs. Ag/AgCl, scan rate 0.05 V/sec.

Integration of the desorption current reveals that an average of 0.062±0.010 nmol/cm^2 11-mercaptoundecanoic acid molecules adsorb within a contact printed *n*-dodecanethiol monolayer. That is roughly 8% of a full 11-mercaptoundecanoic acid monolayer having a surface coverage of 0.786 nmol/cm^2. These measurements reflect the adsorption of 11-mercaptoundecanoic acid at defect sites and the possibility of the unavoidable exchange of printed *n*-dodecanethiolate by 11-mercaptoundecanoic acid during the backfill procedure. Xing *et al.* studied the displacement of pure *n*-dodecanethiol SAMs by 11-mercaptoundecanoic acid in solution by following the evolution of capacitance measured from EIS.[89] They found significant mixing of the thiols occurred after 24 hours and that the *n*-dodecanethiol monolayer had nearly been completely replaced by 11-mercaptoundecanoic acid after 144 hours.[89] While Xing's study considered the displacement over long times, it could be possible that mixing occurs for our system within the first 15 minutes. Chapter 3 provided evidence that contact printed monolayers contain more defects than solution adsorbed monolayers. Because of the large amount of defects within contact printed films, the lateral interactions between adjacent chains are weakened making them more susceptible to exchange. Further studies are needed to understand the exchange rate of contact printed thiols by backfill molecules.

4.3.3 Effect of Multiple User-Defined Domain Boundaries

Applications of contact printed self-assembled monolayers intend to have complex interfacial structures with many user-defined domain boundaries. Therefore, it was prudent to study the effect of these additional macroscopic domain boundaries. Binary contact printed patterns (with one user-defined domain boundary) were compared to contact printed patterns with four user-defined domain boundaries. The complex pattern was established by printing lines of *n*-

dodecanethiol on a gold substrate and backfilling with *n*-dodecanethiol. Details of master fabrication and monolayer preparation were discussed previously in Section 4.2.3.

4.3.3.1 Multi-Line Pattern of *n*-Dodecanethiol and *n*-Dodecanethiol

A multi-line pattern of *n*-dodecanethiol and *n*-dodecanethiol was compared to a binary pattern of the same by electrochemical impedance spectroscopy. The complex impedance plots are shown in Figure 4.8. Both patterned SAMs have larger impedances than a homogeneous contact printed *n*-dodecanethiol SAM (50.2 kΩ); as discussed earlier, backfill molecules saturate defect sites within the contact printed domains and increase the charge transfer resistance of patterned SAMs. The multi-line pattern with four user-defined domain boundaries (Figure 4.8 b) exhibits a much smaller impedance than the binary pattern with one user-defined domain boundary (Figure 4.8 a). The quantitative estimate of the charge transfer resistance of the multi-line pattern is 232 kΩ, a value which is nearly four times smaller than the binary pattern at 855 kΩ (Table 4.5). This result indicates that more complex interfacial structures have an increased presence of defects that impact the observed charge transfer resistance.

Quantitative estimates of the values of the double layer capacitance also support an increased amount of defects with complex interfacial patterns. The C_{dl} of binary patterned *n*-dodecanethiol (1.05±0.01 μF) almost reaches the limiting value of pure solution adsorbed *n*-dodecanethiol (0.99±0.01 μF). However, the double layer capacitance of the multi-line pattern is 2.60±0.10 μF. While the binary pattern has a capacitance similar to that of a densely packed monolayer, the significantly higher capacitance is most likely due to areas of exposed gold substrate at defect sites where the redox probe can approach the substrate uninhibited by the molecules that comprise the monolayer.

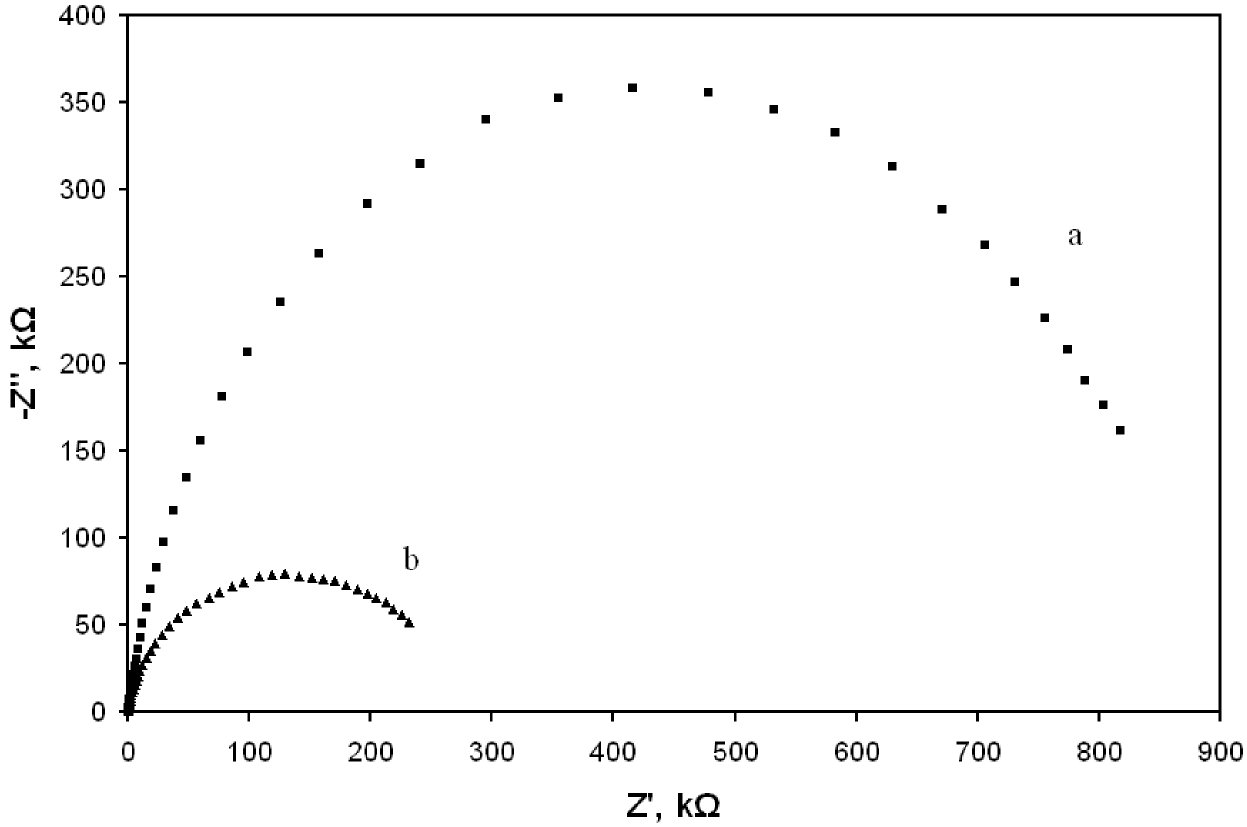

Figure 4.8 Complex impedance plots of patterned *n*-dodecanethiol monolayers with (a) one and (b) four user-defined domain boundaries. EIS conditions: 0.005 M $[Fe(CN)_6]^{-4/-3}$ in 0.1 M KCl of pH 7 at a potential of 0.2 V vs. Ag/AgCl.

Concentration Thiol, Method	**R_s (Ω)**	**R_{ct} (kΩ)**	**C_{dl} (μF)**
Multi-Line Pattern of *n*-dodecanethiol	134±7	232±7	2.60±0.10
Binary Pattern of *n*-dodecanethiol	151±1	855±4	1.05±0.01

Table 4.5 Summary of fitted equivalent circuit values of multi-line and binary patterned *n*-dodecanethiol monolayers.

The impact of increased user-defined domain boundaries is evident by the difference in charge transfer resistance of binary and multi-line patterned *n*-dodecanethiol self-assembled monolayers. The prepared monolayers only differ by the number of user-defined domain boundaries, thus the contributing factor to the difference in the charge transfer resistance is the varying degree of macroscopic domain boundaries. While the backfill molecules adsorb at areas of unmodified gold, they cannot compensate for the vast domain boundaries created by the contact printed pattern. We believe these domain boundaries are the defect sites that contribute most to the observed charge transfer. The more user-defined domain boundaries, the lower the experimental charge transfer resistance. While backfilling for longer periods of time may alleviate the impact of these domain boundaries, the risk of losing the integrity of the distinctly defined regions increases. This finding answers the question of what role patterning an interface has on generating defects: patterning an interface introduces more defects within the monolayer structure.

4.3.4 Imaging Patterned Self-Assembled Monolayers

Scanning electrochemical microscopy was used to image the multi-line patterned self-assembled monolayers. Figure 4.9 displays an SECM image showing distinct regions of contact printed *n*-dodecanethiol (low current, -3 nA to -4 nA) and unmodified gold substrate (high current, -5 nA). The contact printed *n*-dodecanethiol regions yield negative feedback and a decrease in current, whereas the unmodified gold regions provide positive feedback with an increase in current.

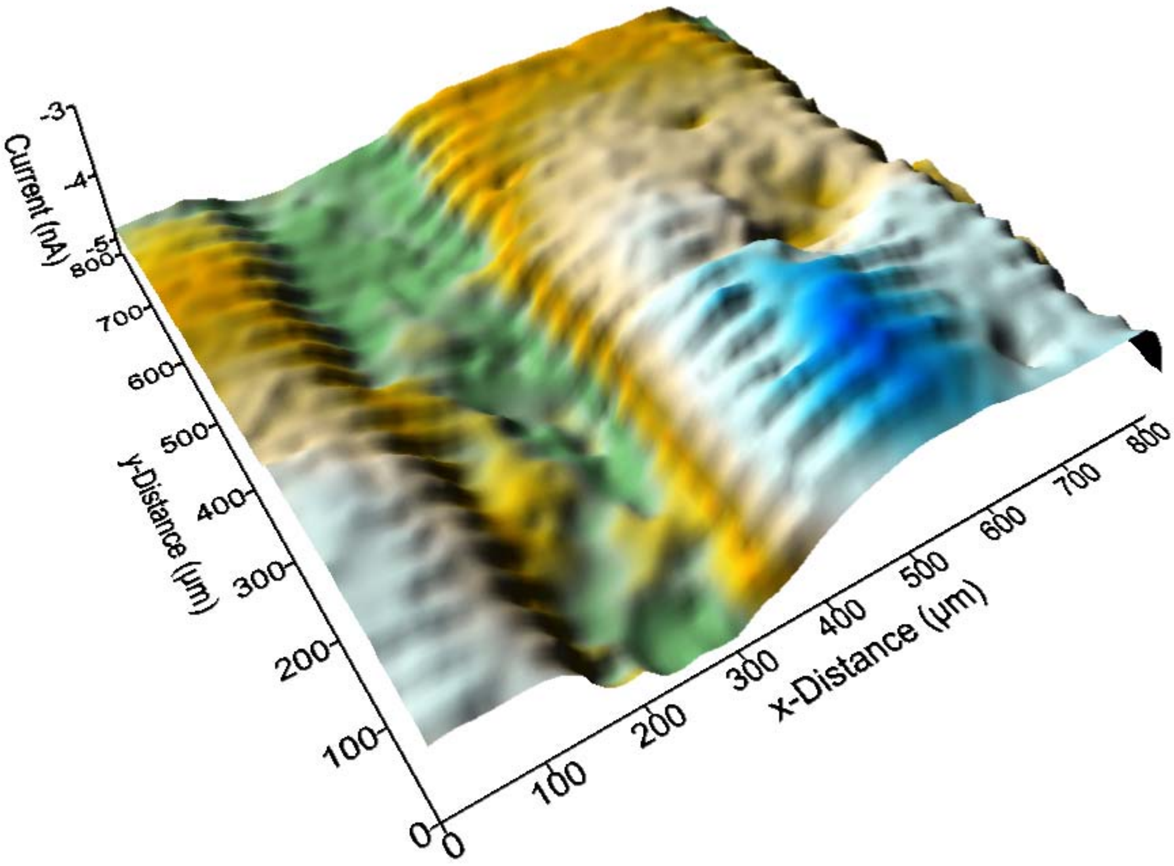

Figure 4.9 SECM image of contact printed *n*-dodecanethiol multi-line pattern on gold. Conditions: 0.005 M $[Fe(CN)_6]^{-4}$ in 0.1 M KCl, Pt bias potential 0.6 V vs. Ag/AgCl, Au bias potential -0.1 V vs. Ag/AgCl.

A detailed image of the domain boundary between unmodified gold and contact printed *n*-dodecanethiol was also imaged by SECM (Figure 4.10). Ruthenium (III) hexaammine was used as the redox probe for this experiment and reduced at the platinum probe. This yields an inverted image from the typical oxidation of ferrocyanide, however the feedback response remains the same. The unmodified gold region yields positive feedback and high current (8 nA), and the contact printed *n*-dodecanethiol domain produces negative feedback and lower current (7.4 nA) The domain boundary appears as a gradual change that extends for roughly 40 µm. The plot in Figure 4.11 follows the current response across the domain boundary in a cross section in the *x*-

direction and clearly identifies each region at the interface. The resolution of the SECM is dependent on the size of the platinum probe which is only 10 μm for our instrument. The pinhole defects at the domain boundaries are too small to image using SECM, a more appropriate measurement would be either atomic force or scanning tunneling microscopy to achieve molecular resolution.

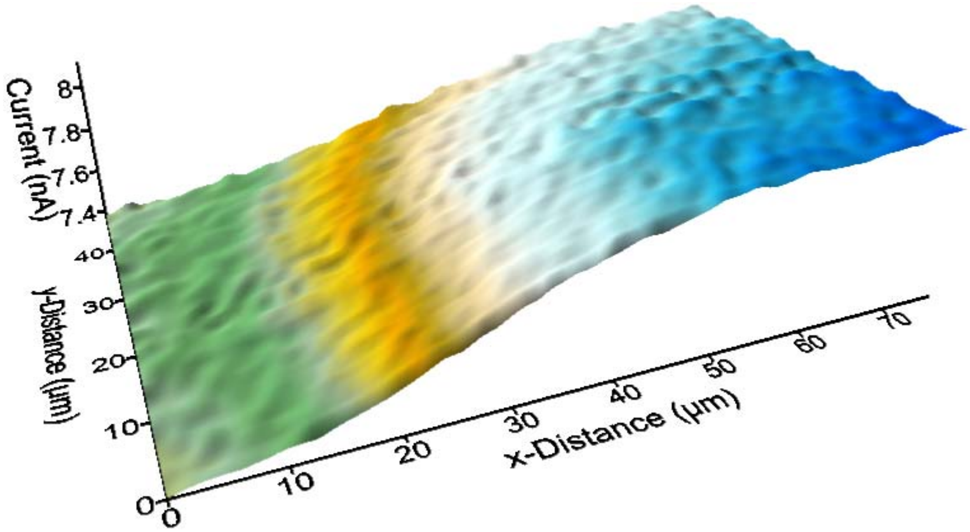

Figure 4.10 Detailed SECM image of domain boundary between contact printed *n*-dodecanethiol and unmodified gold substrate. Conditions: 0.005 M $[Ru(NH_3)_6]^{+3}$ in 0.1 M KCl at pH 7, Pt bias potential -0.5 V vs. Ag/AgCl, Au bias potential 0.0 V vs. Ag/AgCl.

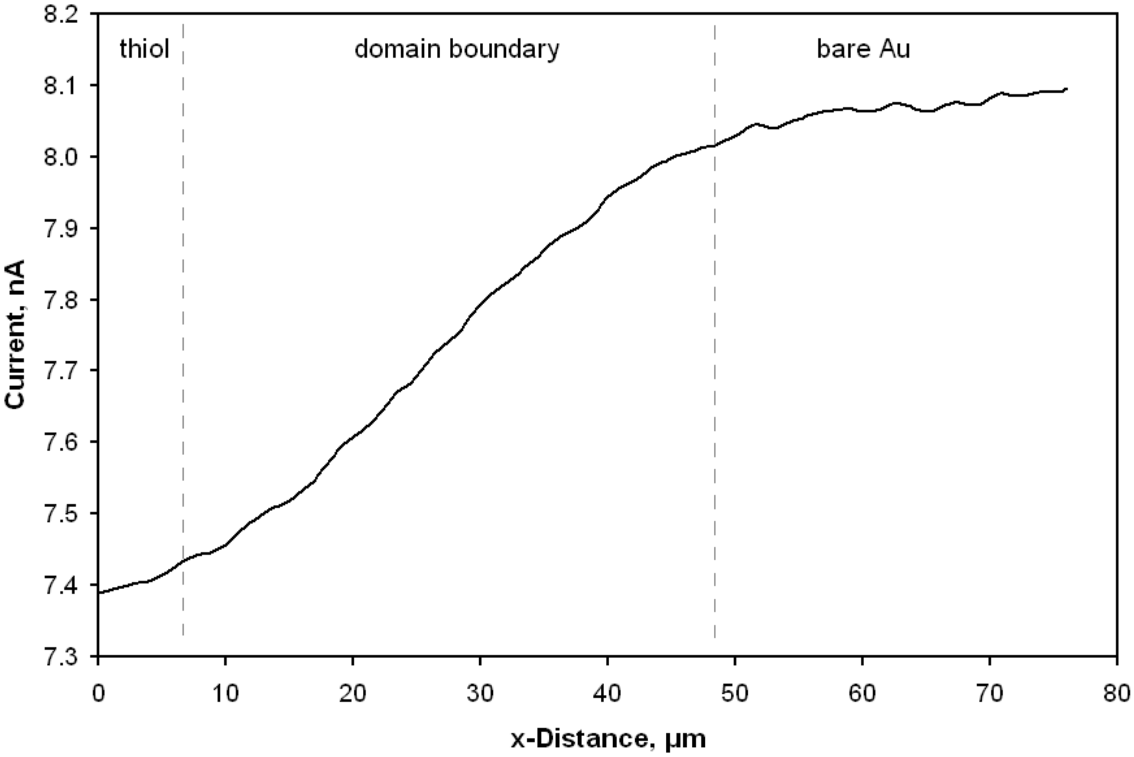

Figure 4.11 Horizontal SECM scan of the domain boundary between *n*-dodecanethiol and unmodified gold substrate.

The SECM measurement maps surface topography by monitoring the change in the electrochemical behavior of a redox probe. We know from earlier discussions that contact printed monolayers have more defects than solution adsorbed monolayers, therefore SECM images of both should reflect this difference. Upon closer examination of Figure 4.9, the contact printed domains appear essentially defect free. This result is due to the limited resolution of the instrument (10 µm), i.e. the defects are too small to image accurately. The difference in electrochemical conductivity between contact printed and solution adsorbed domains of the same monolayer is not significant enough to generate defined regions in a SECM image. However, we were successful in imaging a mixed monolayer using a multi-line pattern of contact printed *n*-dodecanethiol and 11-mercaptoundecanoic acid.

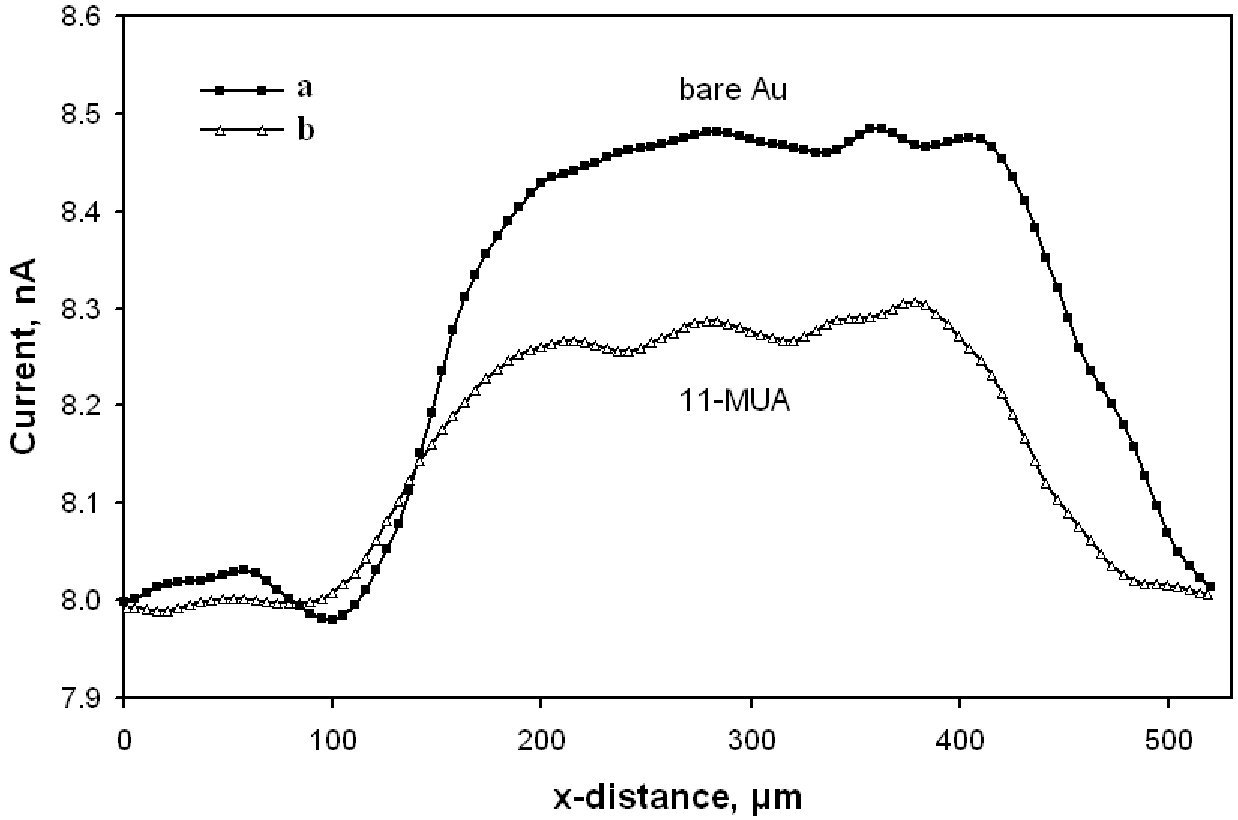

Figure 4.12 Horizontal SECM scan of a multi-line pattern prepared by contact printed *n*-dodecanethiol on gold (a) and then backfilling with 11-MUA (b). Conditions: 0.005 M $[Ru(NH_3)_6]^{+3}$ in 0.1 M KCl at pH 7, Pt bias potential -0.5 V vs. Ag/AgCl, Au bias potential 0.0 V vs. Ag/AgCl.

The mixed monolayer of *n*-dodecanethiol and 11-mercaptoundecanoic acid was imaged before and after backfill. Adsorption of 11-MUA to unmodified gold in the multi-line contact printed *n*-dodecanethiol pattern was confirmed by EIS. The charge transfer resistance of *n*-dodecanethiol lines increased from 7 kΩ to 60 kΩ after backfilling with 11-MUA. Figure 4.12 illustrates that the electronic conductivity of each thiol domain varied sufficiently. As with the other SECM images, negative feedback/low current (8.0 nA) was observed at *n*-dodecanethiol covered regions. High current was observed at both unmodified gold (~8.5 nA) and backfilled 11-MUA (~8.3 nA) regions. Using the favorable electrostatic interaction between the negatively charged carboxylate group of 11-MUA in pH 7 buffer and the positively charged redox probe to our advantage, the electronic conductivity of 11-mercaptoundecanoic acid was greater than *n*-dodecanethiol.

EIS data of homogeneous solution adsorbed 11-mercaptoundecanoic acid monolayers using two oppositely charged redox probes supports this finding and is summarized in Table 4.6. Using ferrocyanide as a redox probe, the impedances of *n*-dodecanethiol and 11-MUA are very high (in the MΩ range). The charge transfer resistance of 11-MUA is slightly higher due to the electrostatic repulsion of the negative redox probe. On the other hand, the impedance varies significantly when using ruthenium (III) hexaammine. The charge transfer resistance of 11-MUA in $[Ru(NH_3)_6]^{3+}$ is only 5.30 kΩ, a difference of two orders of magnitude compared to *n*-dodecanethiol (425 kΩ). A buffered solution of pH 7 is basic enough to deprotonate the carboxylic acid group of 11-MUA, and in turn the positive redox probe is attracted to the negatively charged interface; this electrostatic attraction better facilitates the charge transfer during EIS measurements.[94] These results confirm the electron conductivity of 11-MUA and *n*-dodecanethiol vary depending on the redox probe used during experiments.

Monolayer	**R_{ct} (kΩ)**	
	$[Fe(CN)_6]^{-4}$	$[Ru(NH_3)_6]^{+3}$
n-dodecanethiol	1,490±30	425±3
11-mercaptoundecanoic acid	2,770±110	5.30±0.09

Table 4.6 Charge transfer resistance of solution adsorbed *n*-dodecanethiol and 11-mercaptoundecanoic acid SAMs using ferrocyanide and ruthenium (III) hexaammine as redox probes in pH 7 buffered solutions.

From the EIS findings, we can say for certain that the SECM images did successfully distinguish between phases of the mixed multi-line patterned self-assembled monolayer. After backfilling with 11-MUA, the current at the unmodified gold region decreased about 0.2 nA which describes the slightly insulating character of the adsorbed carboxylate terminated monolayer. Scanning electrochemical microscopy can image mixed monolayers, but only if the electronic conductivity varies significantly between phases.

4.4 Conclusions

Electrochemical impedance measurements of patterned contact printed self-assembled monolayers demonstrate the impact vast domain boundaries have on the overall electrochemical response. Binary patterns with one user-defined domain boundary have intermediate properties of homogeneous contact printed and solution adsorbed monolayers. When the number of user-defined domain boundaries was increased, the defect density rose as evidenced by a decrease in charge transfer resistance. Domain boundaries are inherent in the structure of self-assembled monolayers and are greatly susceptible to charge transfer because of the disorder between neighboring alkane chains. When domain boundaries are created by contact printing a pattern, these defects now extend across the interface on the macroscopic scale. Essentially, designing more complex interfacial patterns generates monolayers with higher defect density, and for electrochemical applications, this could be detrimental.

Another cause for concern is that secondary thiol molecules saturate defects within contact printed portions of patterned SAMs during the backfill process. It was noted that complex impedance plots of binary patterned SAMs appeared more similar to the pure solution adsorbed response rather than the contact printed SAMs. Defect saturation was confirmed by the increase in charge transfer resistance when homogeneous contact printed monolayers were subjected to backfill procedures. There was also an indication of monolayer reorganization and replacement of printed molecules during backfill. Because the contact printed domains are not well-ordered, the backfill molecules penetrate these areas and diminish the distinctly defined regions. The purpose of patterning is to segregate regions with varying properties across the interface in a controlled manner, but the backfill process works against this objective when using defect riddled contact printed patterns of alkanethiols.

Scanning electrochemical microscopy images confirmed the presence of defined regions using the multi-line pattern to contact print *n*-dodecanethiol. Imaged domain boundaries extended over much larger areas than expected but is likely due to the limitations of the instrumentation. Higher resolution is needed to image these defect sites and could be obtained by possibly using a smaller radius platinum probe or with other probe microscopies. SECM was proven to be acceptable to image mixed monolayers, but only if the electronic conductivity between monolayer domains differs significantly.

Chapter 5

Site-Selective Reductive Desorption of Self-Assembled Monolayers

5.1 Introduction

The previous chapter described how user-defined domain boundaries formed by contact printing and backfill affect the electrochemical properties of a modified interface. An increase in the number of macroscopic domain boundaries (1-2 mm in length) had a negative impact on the overall passivation of the substrate. Contact printed monolayers were shown to have more defects than solution adsorbed alkanethiol monolayers, therefore we wanted to begin with a well-ordered self-assembled monolayer and determine how it behaves when large domain boundaries are generated and then replaced. Domain boundaries are generated in a solution adsorbed monolayer by site-selective reductive desorption using a scanning electrochemical microscope.

In the previous two chapters, bulk reductive desorption was accomplished by applying a large negative overpotential to reduce the Au-S bond between the substrate and adsorbed alkanethiol using an auxiliary electrode with a large surface area. However, if the size of the auxiliary electrode is significantly reduced and its height fixed very close to the substrate, the surface will become polarized. The electric field is localized to the region between the auxiliary electrode and substrate; therefore, only thiol directly below the auxiliary electrode will be desorbed (Figure 5.1).[42] This concept is called site-selective reductive desorption (SSRD) which can be performed using a scanning electrochemical microscope (SECM). SSRD uses the Pt ultramicroelectrode probe as the auxiliary electrode while the SECM controls its exact placement. With the lateral mobility of SECM, patterns can be etched into adsorbate-covered Au surfaces using site-selective reductive desorption.[42, 44] The renewed Au substrate can be further functionalized; for example, Wittstock et al. covalently adsorbed glucose oxidase enzymes to amino-derivatized disulfides at SSRD regions.[43]

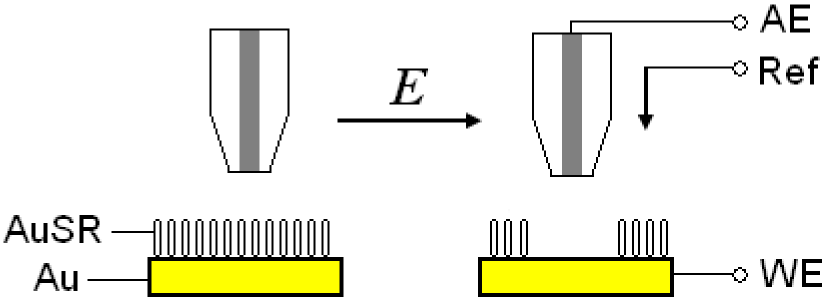

Figure 5.1 Principle of site-selective reductive desorption using scanning electrochemical microscopy. *E*, potential; AE, auxiliary electrode; Ref, reference electrode; WE, working electrode.

Using a scanning electrochemical microscope probe, one can selectively desorb regions within self-assembled monolayers and essentially create large “defects” of exposed Au with domain boundaries less than 500 µm. Site-selective reductive desorption is not only another method to create interfacial patterns within monolayers, but also a means to investigate the impact of user-defined domain boundaries. The desorbed regions are backfilled with alkanethiol, and the impedance changes are used to describe the behavior at each stage of the process.

This chapter describes the behavior of monolayers containing site-selective reductive desorption generated “defects”. Cyclic voltammetry and electrochemical impedance spectroscopy results indicate that small desorbed regions within self-assembled monolayers behave as microelectrodes. Factors such as probe-substrate distance and alkyl chain length which affect the desorbed feature size are investigated. A mixed-monolayer created by SSRD and backfill demonstrates the impact of smaller scale user-defined domain boundaries.

5.2 Experimental Details

5.2.1 Monolayer Preparation

Gold disk electrodes were cleaned according to the procedure in Section 2.3.1.2. Monolayers were prepared on gold disk electrodes by immersion in a 0.001 M *n*-alkanethiol solution for at least 18 hours at 25°C. Alkanethiols used were *n*-octanethiol, *n*-dodecanethiol, or *n*-octadecanethiol. The substrates were then rinsed in ethanol, followed by water, and dried in a stream of nitrogen gas prior to use.

After site-selective reductive desorption, the modified electrodes were rinsed, dried, and placed in 0.001 M *n*-alkanethiol solutions for 15 min in order to backfill the desorbed regions. Backfill alkanethiols include *n*-octanethiol, *n*-dodecanethiol, *n*-octadecanethiol, and 11-mercaptoundecanoic acid.

5.2.2 Experimental Conditions of Electrochemical Measurements

5.2.2.1 Cyclic Voltammetry

Cyclic voltammetry measurements were conducted in solutions of 0.005 M $[Fe(CN)_6]^{-3/-4}$ in 0.1 M KCl buffered to pH 7. The potential was swept between -0.2 V and 0.7 V versus a saturated Ag/AgCl reference electrode at a rate of 0.05 mV/s, unless otherwise noted.

5.2.2.2 Electrochemical Impedance Spectroscopy

Electrochemical impedance measurements were conducted in the same solutions used for cyclic voltammetry, unless otherwise noted. Measurements were performed by applying an AC potential having a 5 mV amplitude that is symmetric about the formal potential of the redox probe (0.2 V vs. Ag/AgCl). The frequency range was 1.0×10^5 Hz to 0.1 Hz. Quantitative estimates of the equivalent circuit elements were obtained by fitting the experimental data to a Randles equivalent circuit using the fitting routines provided by LEVM 7.0.

5.2.2.3 Scanning Electrochemical Microscopy

Images were obtained in aqueous solutions containing either 0.005 M $[Fe(CN)_6]^{-4}$ or 0.005 M $[Ru(NH_3)_6]^{3+}$ in 0.1 M KCl buffered to pH ~8. The bias potentials using ferrocyanide were 0.6 V and -0.1 V vs. Ag/AgCl for the platinum ultramicroelectrode and gold substrate, respectively. For ruthenium hexaammine, the bias potentials were -0.5 V and 0.0 V for the UME and Au working electrodes, respectively. A platinum wire served as the auxiliary electrode and Ag/AgCl as the reference electrode. All images were obtained in feedback mode.

Site-selective reductive desorption was performed by using the platinum ultramicroelectrode as the auxiliary electrode and removing the platinum wire from the sample cell. An overpotential of either -1.0 or -1.4 V vs. Ag/AgCl was applied to the gold substrate for 2 or 10 seconds, respectively. See Section 5.3 for schematic representations of the desorption patterns.

5.3 Results and Discussion

5.3.1 Characterization of Commercial and Generated Au Microelectrodes

The following results compare the electrochemical behavior of a commercially available Au ultramicroelectrode to that of a site-selective reductive desorption (SSRD) generated "microelectrode" within a solution adsorbed *n*-dodecanethiol self-assembled monolayer. Pinhole defects within self-assembled monolayers have been described as an array of microelectrodes.[25] Here, we have essentially created a large defect by desorbing a specific region of alkanethiol molecules and found the behavior to be similar to a microelectrode. It is important to understand how these SSRD-modified interfaces behave before interpreting the impact of user-defined domain boundaries.

First, we consider the typical electrochemical response of a commercially available 10 μm gold ultramicroelectrode (UME). The cyclic voltammogram in Figure 5.1 shows the typical sigmoidal response of a commercial Au UME in which the response approaches a limiting value of 6.9 nA. This is because the UME exhibits hemispherical diffusion, not semi-infinite linear diffusion like macroelectrodes; the limiting current is controlled by the mass transfer rate of the diffusion of electroactive species from the bulk to the electrode surface.[65] This limiting value, also called the steady-state current for a disk electrode, is given by the equation

$$i_{\mathrm{ss}} = 4nFDC^{*}r \qquad \textbf{(5.1)}$$

where n is the number of electrons transferred, F is Faraday's constant, D is the diffusion coefficient of the redox probe, C^{*} is the bulk concentration of the redox probe, and r is the radius of the disk. Solving Equation 5.1 using the steady state current of the Au UME (6.9 nA), the radius of the disk is confirmed at 5 μm for a 10 μm ultramicroelectrode.

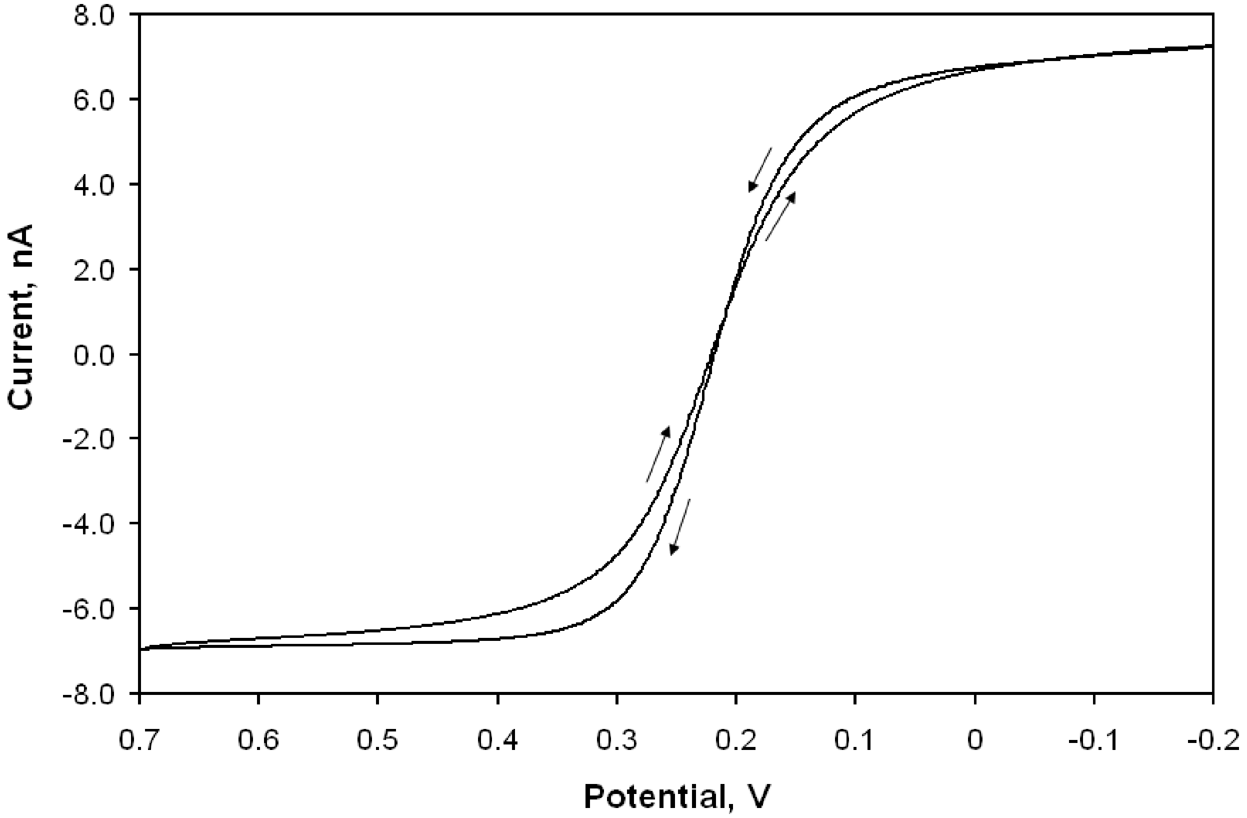

Figure 5.2 Cyclic voltammogram of a 10 μm Au ultramicroelectrode. Conditions: Aqueous solution of 0.005 M $[Fe(CN)_6]^{-4/-3}$ in 0.1 M KCl at pH 7, scan rate 0.05 V/s, potential vs. Ag/AgCl.

Electrochemical impedance was used to characterize the Au ultramicroelectrode. The shape of the complex impedance plot (Figure 5.2) is consistent with previous reports of ultramicroelectrodes.[95-97] The first, small semicircle at high frequency corresponds to the charge transfer resistance of the electrode.[95] As with the cyclic voltammetry results, the effects of diffusion of electroactive species are apparent and are displayed as a second semicircle in the impedance plot.[95] Because of the presence of two semicircles, the simple Randles equivalent circuit model does not apply and cannot be used to estimate element values.

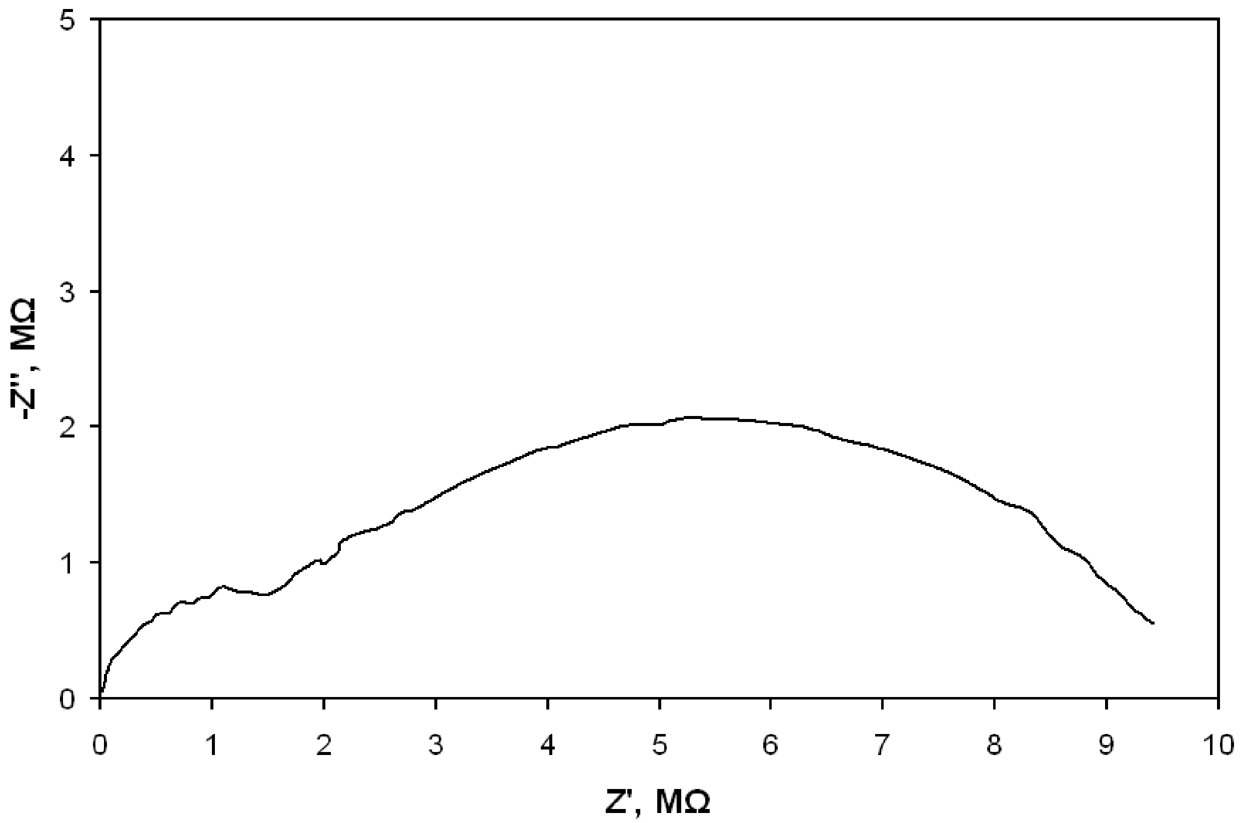

Figure 5.3 Complex impedance plot of a 10 µm Au ultramicroelectrode in an aqueous solution of 0.005 M $[Fe(CN)_6]^{-4/-3}$ in 0.1 M KCl at pH 7.

A gold "microelectrode" was created in a *n*-dodecanethiol self-assembled monolayer by desorbing the adsorbates to form an electroactive Au island surrounded by intact thiol chains. Figure 5.4A is a schematic representation of the desorption process. The points indicate the position of the Pt probe at which it was used as the auxiliary electrode to desorb only thiol located directly below. After desorption, the interface was imaged under normal conditions (Figure 5.4B). The dark (high current) region reflects the newly exposed Au substrate where positive feedback is produced. The low current (i.e. negative feedback) is due to the remaining adsorbed thiol.

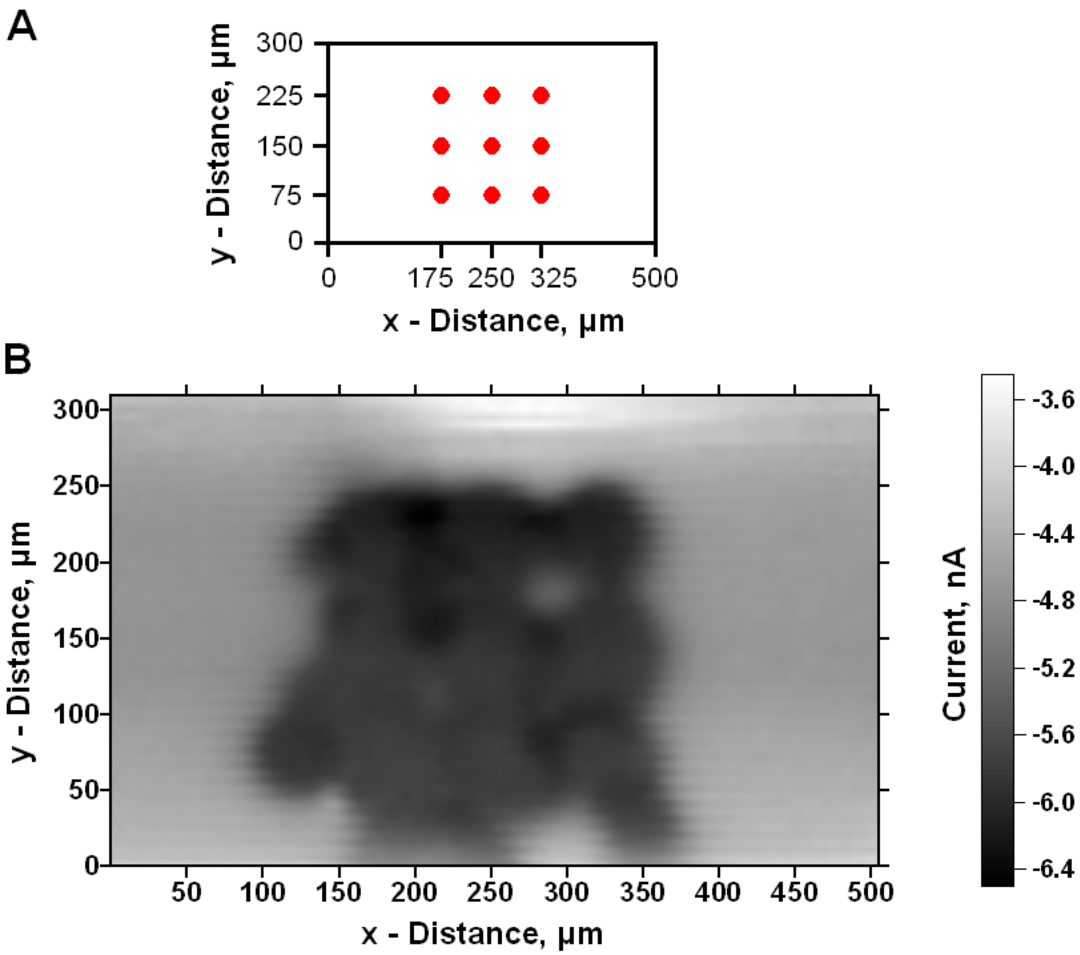

Figure 5.4 Desorption scheme (A) and SECM image (B) of a Au "microelectrode" fabricated within a *n*-dodecanethiol self-assembled monolayer on a gold electrode. Overpotential of -1.0 V vs. Ag/AgCl held for 2 s at designated points in (A). Imaging solution: 0.005 M $[Fe(CN)_6]^{-4}$, 0.1 M KCl, and 0.020 M KOH.

Each of the nine desorption points removes roughly a 50 µm disk area of thiol to produce a 250 µm Au square. However, the desorbed areas are not always disk-shaped. The observed patchy desorption can be attributed to the fact that reductive desorption initiates at defect sites and proceeds domainwise.[98, 99] Even solution adsorbed monolayers prepared from long alkanethiols contain a certain degree of defects, and the lateral interactions between alkane chains at defect sites are weak. The weakened lateral interactions at defects makes these areas more susceptible to be removed by reductive desorption. Thus, it is proposed that when the Pt probe is placed over a region of monolayer with defects, a larger portion of thiol will be removed. This can reasonably explain the observed patchy desorption of Figure 5.4B.

The *n*-dodecanethiol SAM was assessed by cyclic voltammetry before and after fabrication of the “microelectrode”, Figure 5.5. The CV response of the solution adsorbed *n*-dodecanethiol monolayer before SSRD is consistent with previous reports and represents a monolayer with few defects.[100, 101] The voltammogram of the “microelectrode” resembles that of the sigmoidal response of the commercial Au ultramicroelectrode. The steady-state current was estimated at 0.6 μA which yields a disk radius of 400 μm from Equation 5.1. The calculated electroactive area using the disk radius (0.005 cm^2) is roughly equivalent to a 700 μm x 700 μm desorbed grid. This area estimate is significantly larger than the desorbed grid as imaged using SECM but does offer supporting evidence of microelectrode behavior within the same order of magnitude.

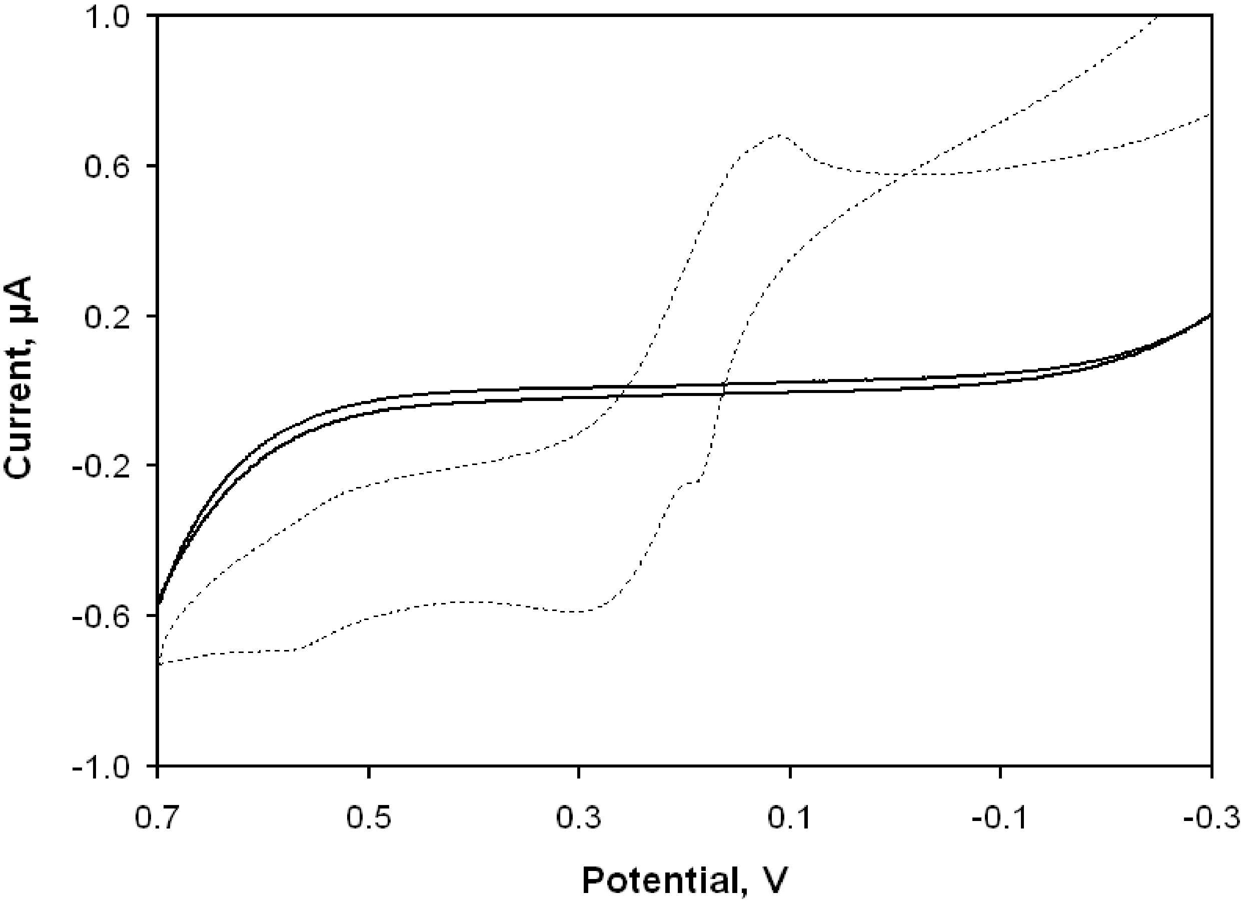

Figure 5.5 Cyclic voltammogram of a solution adsorbed *n*-dodecanethiol monolayer before (—) and after (---) fabrication of a "microelectrode". Conditions: Aqueous solution of 0.005 M $[Fe(CN)_6]^{-4/-3}$ in 0.1 M KCl at pH 7, scan rate 0.05 V/s, potential vs. Ag/AgCl.

Electrochemical impedance data provides confirmation of microelectrode behavior of the desorbed grid within a self-assembled monolayer. The complex impedance plot of the "microelectrode" produced by SSRD is shown as the inset in Figure 5.6. There is a very small semicircle at low frequency like that of the commercial UME; however, the more dominant semicircle is not depressed for the fabricated "microelectrode". The difference may be attributed to the fact that the *n*-dodecanethiol self-assembled monolayer only acts like an insulating material but is still susceptible to charge transfer. The two semicircles present in the complex impedance plot for the "microelectrode" are believed to be the combination of charge transfer at the exposed Au (i.e. "microelectrode") and charge transfer through the *n*-dodecanethiol SAM.

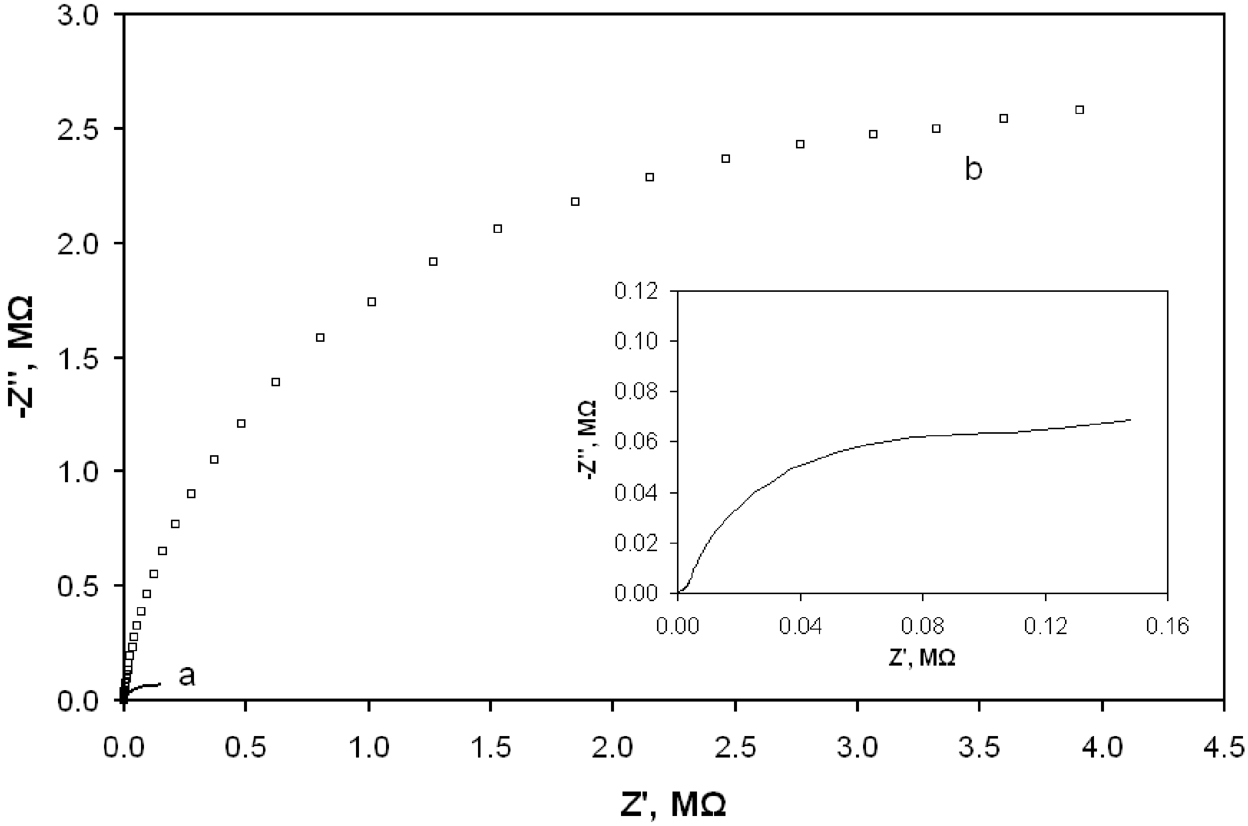

Figure 5.6 Complex impedance plot of a solution adsorbed *n*-dodecanethiol monolayer before (b) and after (a) fabrication of a "microelectrode" in an aqueous solution of 0.005 M $[Fe(CN)_6]^{-4/-3}$ in 0.1 M KCl at pH 7. The inset is a enlarged view of the lower impedance region.

Besides the change in shape of the complex impedance plot, the charge transfer resistance of the modified substrate decreases after desorption of the grid. A sharp decrease in charge transfer resistance is expected because a significantly large area of underlying Au substrate is exposed by site-selective reductive desorption. The created Au island is an area where charge transfer can occur freely thus decreasing the impedance. The microelectrode behavior of the SSRD modified substrate cannot be modeled using the Randles equivalent circuit, therefore direct comparisons of the charge transfer resistance are not available. Upon multiple trials of SSRD of *n*-dodecanethiol, the decrease of charge transfer by an order of magnitude after modification was confirmed.

Site-selective reductive desorption via scanning electrochemical microscopy was used to generate a large "defect" within a well-ordered self-assembled monolayer. This "defect" covered roughly 2% of the geometric area of the macroelectrode and behaved similar to a microelectrode as evidenced by the sigmoidal CV response and the presence of two semicircles in the complex impedance plot. With the current capabilities of our laboratory, SSRD can produce smaller features (i.e. smaller domain boundaries) than using contact printing methods. This fact will be useful in describing the effects of user-defined domain boundaries when the SSRD regions are backfilled. However, we first will consider experimental parameters that affect the size of desorbed features.

5.3.2 Characterization of Feature Size in Site-Selective Reductive Desorption of Alkanethiol Modified Au Substrates

Several factors can affect the size and shape of desorbed regions in alkanethiol monolayers created by site-selective reductive desorption; they include applied overpotential, ionic strength, probe-substrate separation distance, and alkane hydrocarbon chain length. The former two relate to the effective electric field localized between the substrate and probe. These effects were studied by a former group member and results showed that a greater local electric field produced larger features; this included increasing the ionic strength of the supporting electrolyte solution and increasing the applied overpotential.[44] The effect of the latter factors, probe-substrate distance and alkane chain length, on feature size in SSRD modified substrates are presented here.

5.3.2.1 Feature Size as a Function of Probe-Substrate Distance

In site-selective reductive desorption, a Pt ultramicroelectrode is used as an auxiliary electrode to polarize a modified surface so that only thiol located directly below it will be reduced. The size and magnitude of the localized electric field determines the feature size in SSRD. In this study, only the probe-substrate distance varied. The electric field can be expressed by the equation

$$E = V/d \tag{5.2}$$

where E is the magnitude of the electric field between parallel plates, V is the difference in applied potential, and d is the distance between plates.[102] The magnitude of the electric field is indirectly proportional to the separation distance, thus it should decrease as the probe-substrate distance increases and produce smaller features.

A solution adsorbed *n*-dodecanethiol monolayer was imaged by scanning electrochemical microscopy prior to site-selective reductive desorption, Figure 5.7. The Pt UME was rastered in the *xy*-plane at a constant *z*-height. The image should produce negative feedback across the interface indicative of a well-formed, insulating monolayer; however, the feedback current increased in the *y*-direction. This anomaly occurred due to an increase in the probe-substrate separation distance caused by an unlevel substrate. With the existing home built SECM apparatus, it is nearly impossible to level the substrate over large distances (100s of μm). A tilt-rotation stage from Thorlabs (Newton, NJ) was installed to adjust the substrate tilt but unfortunately did not eliminate the problem. The substrate in Figure 5.7 tilts down to the back (y = 200 μm). With a larger probe-substrate distance (y > 100 μm), the diffusion of the electroactive species over an insulating surface is less hindered and the feedback current approaches the steady-state current (-6.5 nA).

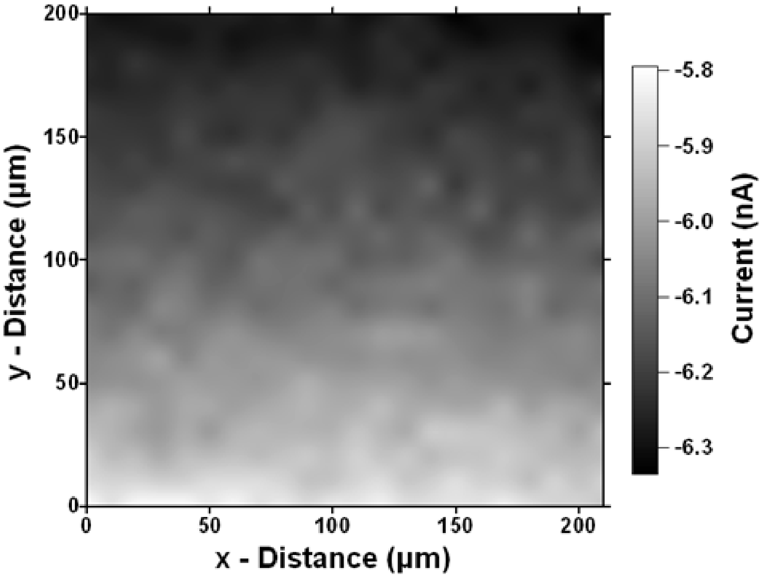

Figure 5.7 SECM image of a solution adsorbed *n*-dodecanethiol self-assembled monolayer on gold. Imaging solution: 0.005 M $[Fe(CN)_6]^{-4}$, 0.1 M KCl, and 0.020 M KOH.

Two Au microdots were generated by site-selective reductive desorption in a solution adsorbed *n*-dodecanethiol self-assembled monolayer by applying -1.4 V vs. Ag/AgCl for 10 seconds at the positions designated in Figure 5.8A. The extreme overpotential and long desorption time were chosen to ensure complete desorption of *n*-dodecanethiol. After site-selective reductive desorption, the newly exposed Au islands were imaged by SECM under normal conditions, Figure 5.8B. As expected, the generated Au microdots produce positive feedback when imaged, while the surrounding intact thiol domains yield negative feedback. The homogeneous current across the microdots verifies complete removal of thiol at the desorption sites.

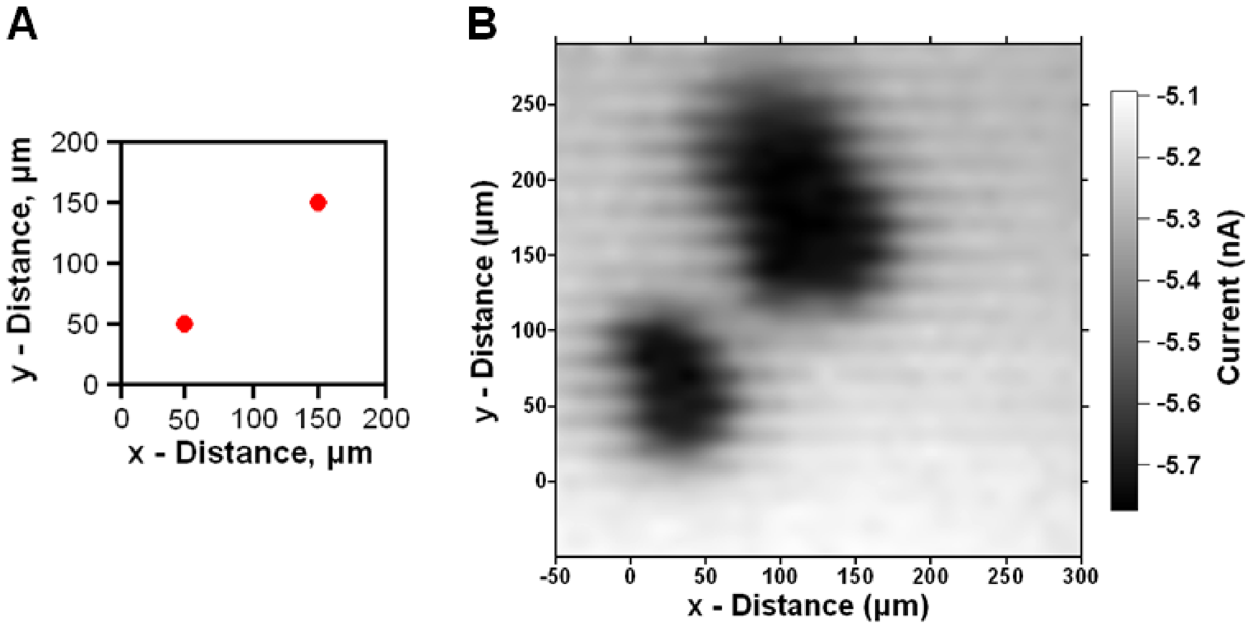

Figure 5.8 Desorption scheme (A) and SECM image (B) of desorbed microdots in a solution adsorbed *n*-dodecanethiol self-assembled monolayer on gold. Overpotential of -1.4 V vs. Ag/AgCl held for 10 s at designated points in (A). Desorption and Imaging solution: 0.005 M $[Fe(CN)_6]^{-4}$, 0.1 M KCl, and 0.020 M KOH.

Taking advantage of the fact that the probe-substrate distance increases in the *y*-direction, different sizes of desorbed microdots were produced. According to Equation 5.2, the magnitude of the localized electric field should decrease proportional to an increase in probe-substrate distance; a smaller localized electric field would then produce a smaller desorbed region. However, the opposite effect is observed—larger desorbed features at increased probe-substrate distances. The lower left Au microdot of Figure 5.8B is roughly 75 µm x 75 µm, while the upper right desorbed region extends 125 µm x 125 µm. When the Pt probe is very close to the substrate (50 µm, 50 µm), the effective electric field is localized over a small area of alkanethiol. As the probe is moved away from the substrate (150 µm, 150 µm), the local electric field extends over a larger area resulting in greater amounts of desorbed thiol. The probe-substrate separation distance was determined to change about 4 µm between desorption sites. The currents recorded at (*x*,*y*) positions (50 µm, 50 µm) and (150 µm, 150 µm) in the unmodified monolayer of Figure

5.7 were compared to the currents from the approach curve generated before desorption to determine the *z*-height at the specific coordinates. Even though the magnitude of the electric field decreases with increasing distance according to Equation 5.2, the negative overpotential here was in excess and desorbed the thiol domains located below the probe.

Wilhelm et al. describes site-selective reductive desorption as self-limiting when the desorbed feature reaches a magnitude relative to the size of the Pt probe.[103] At that time, the current flow cannot be maintained between the Au electrode and the auxiliary Pt probe, and the potential of the Au electrode collapses which in turn ends the desorption process.[103] At higher probe-substrate distances, the current flow can be maintained over a greater portion of the substrate because the size of the auxiliary Pt probe appears larger. This supports why larger features are produced at higher probe-substrate distances.

Another reasonable explanation for the observed difference in feature size is the extent of defects within the adsorbed monolayer. Since desorption initiates at defect sites, it would stand that placement of the Pt probe over a defective region would produce larger features than at a well-ordered domain. In this case, the desorbed Au microdot at (150 µm, 150 µm) is proposed to have had more defects within the *n*-dodecanethiol monolayer than at (50 µm, 50 µm). However, we do not believe this is the case because larger features were consistently produced at greater probe-substrate distances.

This study showed that at large probe-substrate distances using sufficient applied overpotential, greater areas of adsorbed thiol were removed than at small probe-substrate distances. This result is important to consider as it is consistently seen in all images of site-selective reductive desorption modified substrates.

5.3.2.2 Feature Size as a Function of Alkanethiol Chain Length

The size of the thiol domains removed during site-selective reductive desorption also depends on the chain length of adsorbed alkanethiol. Section 2.6 discussed why alkanethiols of varying methylene units desorb at their own unique potential. While the energy required to reduce the Au-S bond is equivalent for all thiol molecules, different monolayers have varying degrees of lateral interactions which must also be overcome for desorption to occur. Short alkanethiols should desorb more completely and have larger features because less energy is required to remove the thiol. Whereas, longer alkanethiols will yield smaller, patchy desorption features because the increased lateral interactions create stability within the monolayer and allow it to sustain the desorption process. This section discusses how desorbed feature size depends on alkanethiol chain length.

Two 150 µm lines were desorbed in solution adsorbed alkanethiol monolayers of *n*-octanethiol, *n*-dodecanethiol, and *n*-octadecanethiol using site-selective reductive desorption. The lines were desorbed at a modest overpotential of -1.0 V vs. Ag/AgCl for 2 seconds at the points designated in Figure 5.9A. The desorption points are separated by a distance of 50 µm which produces a continuous desorbed line; however, the lines were separated by a distance of 220 µm as to remain distinct features. The SECM images of the desorbed lines are in Figure 5.9B-D.

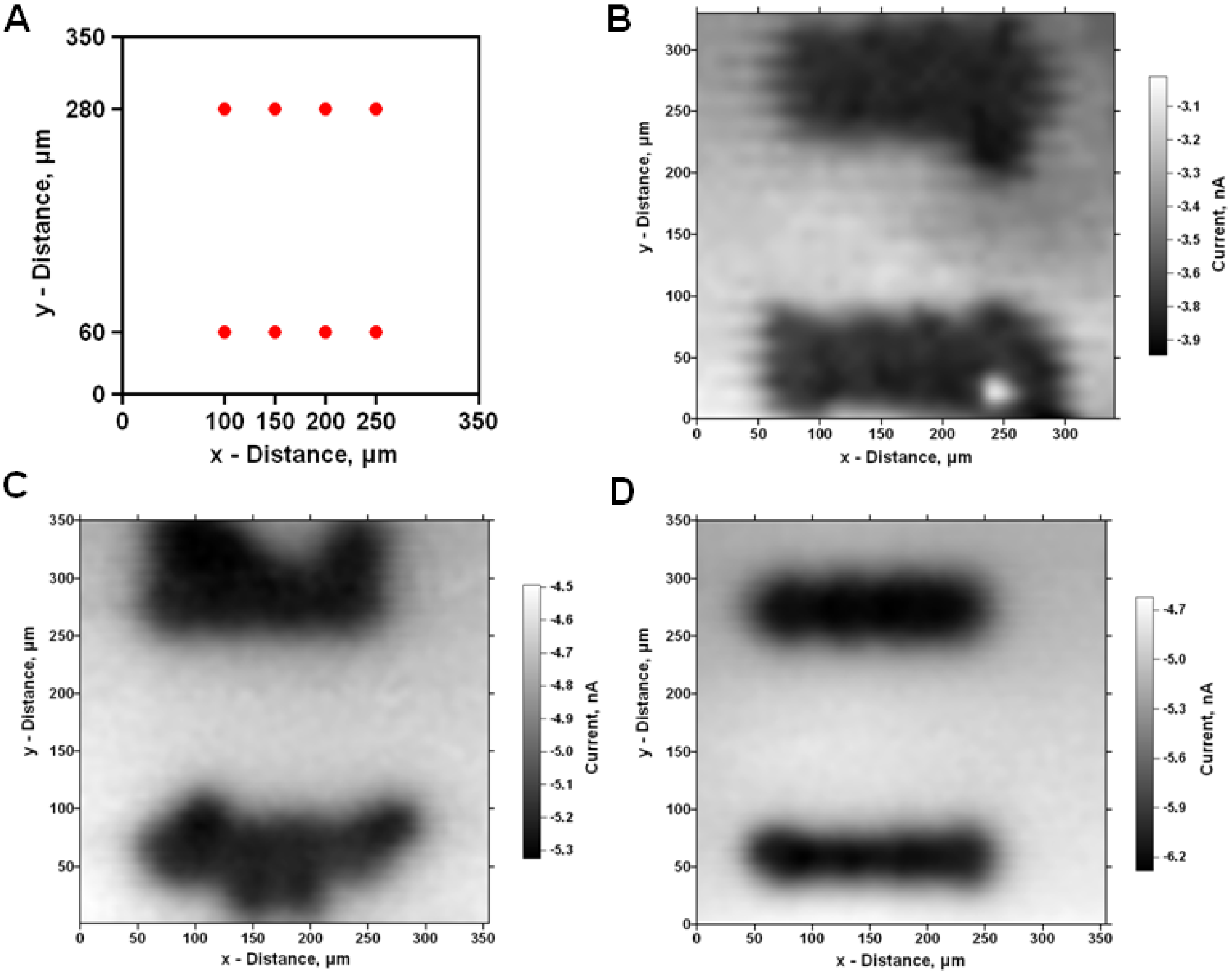

Figure 5.9 Desorption scheme (A) and SECM images of desorbed lines in solution adsorbed *n*-octanethiol (B), *n*-dodecanethiol (C), and *n*-octadecanethiol (D) self-assembled monolayers on gold. Overpotential of -1.0 V vs. Ag/AgCl held for 2 s at designated points in (A). Desorption and Imaging solution: 0.005 M $[Fe(CN)_6]^{-4}$, 0.1 M KCl, and 0.020 M KOH.

The site-selective reductive desorption of 150 µm lines in a monolayer of *n*-octanethiol produces broad features in which large domains of thiol are desorbed, Figure 5.9B. The overpotential of -1.0 V vs. Ag/AgCl reduces the thiol domains beneath the Pt probe used as the auxiliary electrode and is also sufficient to desorb regions well beyond the size of the probe. From Chapter 3, we know that shorter alkanethiol monolayers have higher defect density because of the decreased amount of lateral Van der Waals interactions between alkane chains. Greater defect density causes the monolayer to be more susceptible to desorption because desorption initiates at defects and, therefore, results in larger feature sizes. The localized electric field at -1.0 V is strong enough to desorb large areas of *n*-octanethiol.

With four additional methylene units, the desorbed lines of *n*-dodecanethiol are still broad but appear as patchy desorption sites, Figure 5.9C. *n*-Dodecanethiol has more lateral chain-chain interactions than *n*-octanethiol to stabilize the monolayer structure. This property causes the monolayer to desorb in patchy domains, rather than complete desorption over vast regions. The local electric field is powerful enough to desorb the weakly interacting thiol domains but not the strongly interacting domains. Again, it is the thought that desorption initiates at defect sites which gives the patchy features.

With this understanding, it is interesting that the desorbed regions of *n*-octadecanethiol are not patchy but rather thin, continuous lines. It was expected that the increased lateral interactions of the longest alkanethiol tested would cause very patchy desorption features. It is believed that the localized electric field is only strong enough to desorb the thiol located in a small region below the probe. In bulk reductive desorption, an overpotential of -1.0 V vs. Ag/AgCl is not great enough to desorb *n*-dodecanethiol or *n*-octadecanethiol but is for SSRD because of the close proximity of the auxiliary and working electrodes. The magnitude of the localized electric field is greatest under the center of the probe, and the surface polarization decreases outward. Therefore, a smaller portion of the electric field is able to remove the *n*-octadecanethiol.

Alkanethiol	Peak Widths (µm) at x = 200 µm*	Peak Lengths (µm) at y = 60 µm, and y = 280 µm	Peak Current (nA) of Measured Values
n-Octanethiol	55, 86	189, 189	-3.7
n-Dodecanethiol	43, 41	179, 179	-5.2
n-Octadecanethiol	17, 32	172, 170	-6.1

Table 5.1 Summary of size of desorbed lines as a function of alkanethiol chain length. *The first value is the line at y < 100 µm, the second is the line at y >200 µm.

Table 5.1 summarizes line widths and lengths created from site-selective reductive desorption of solution adsorbed n-alkanethiols. As expected, the line width measured at x = 200 µm decreases with increasing chain length. The smallest lines (17 µm and 32 µm) are produced from the longest hydrocarbon chain n-octadecanethiol, whereas the short chain n-octanethiol had the widest lines at 55 µm and 86 µm. The second line (y > 200 µm) of n-dodecanethiol does not follow the trend due to the patchy desorption. At x = 250 µm, the line width for n-dodecanethiol is 75 µm, which does follow the trend in Table 5.1. The lines for each monolayer at y > 200 µm are larger because of the increased probe-substrate distance as explained in Section 5.3.2.1. The difference in z-height was estimated at 10 µm across ~200 µm in the y-direction. The desorbed line lengths also follow the trend of increasing hydrocarbon chain (189 µm for n-octanethiol, 179 µm for n-dodecanethiol, and 172 µm for n-octadecanethiol), yet oddly remain constant within each monolayer (189 µm at y = 60 and 189 µm at y = 280 for n-octanethiol, etc.).

This study showed that the chain length of an adsorbed alkanethiol affects both the size and shape of site-selective reduction desorption features. It is the degree of lateral interactions between the chains that define feature size in SSRD, just like they do for the determination of the reduction potential in bulk desorption. This study also confirmed the dependence of probe-substrate separation distance on feature size. The effect of these generated user-defined domain boundary defects after backfill are discussed in the following section.

5.3.3 Characterization of Backfilled Site-Selective Reductively Desorbed Monolayers

The previous sections described how scanning electrochemical microscopy can be used to create regions of renewed Au in well-ordered solution adsorbed alkanethiol monolayers by means of site-selective reductive desorption. The renewed Au regions can be considered as gross defects because they are sites where electron transfer can occur freely and lateral interactions between the neighboring chains are weak or completely severed. Electrochemical impedance spectroscopy is sensitive to the changes in charge transfer resistance and was used to follow the transformation before and after site-selective reductive desorption.

5.3.3.1 Backfill SSRD Lines with Same *n*-Alkanethiol

The complex impedance plots of the *n*-octadecanethiol monolayer (Section 5.3.2.2, Figure 5.9D) before and after using site-selective reductive desorption to create two 150 μm lines of renewed Au are compiled in Figure 5.10. The estimated charge transfer resistance using an equivalent circuit model of *n*-octadecanethiol before modification was 5.6 MΩ. After desorbing the two lines by SSRD, the impedance (Figure 5.10b) decreased by an order of magnitude; this is consistent with the impedance change in Section 5.3.1. Similar to the complex impedance plots of the "microelectrode" generated by site-selective reductive desorption, the *n*-octadecanethiol plots show a slight appearance of two semi-circles (inset of Figure 5.10). Again, it is believed the two semicircles are the combined effects of the charge transfer at the exposed Au substrate and the charge transfer through the insulating monolayer at low and high impedance, respectively. Because of the presence of two semicircles in the impedance plot, the simple

Randles equivalent circuit cannot be used to estimate the charge transfer resistance of the SSRD-modified *n*-octadecanethiol monolayer, thus the values were estimated from the complex impedance plots. However, the overall decrease in charge transfer is apparent as thiol domains are removed from the surface.

The SSRD-modified *n*-octadecanethiol monolayer was backfilled with 0.001 M *n*-octadecanethiol for 15 minutes and characterized by EIS. The thought was that because the user-defined domain boundaries created by site-selective reductive desorption were more gradual due to the desorption process than those formed by contact printing, the initial charge transfer resistance would be recaptured during the 15 minute backfill time. The charge transfer resistance of the SSRD-modified *n*-octadecanethiol monolayer increased from ~400 kΩ to ~650 kΩ after the 15 minutes backfill time. The increase in charge transfer confirms the adsorption of *n*-octadecanethiol to the bare Au regions. However, the impedance only increased slightly which indicates that small user-defined domain boundaries (on the order of 200 µm) can also greatly impact the observed electrochemical behavior.

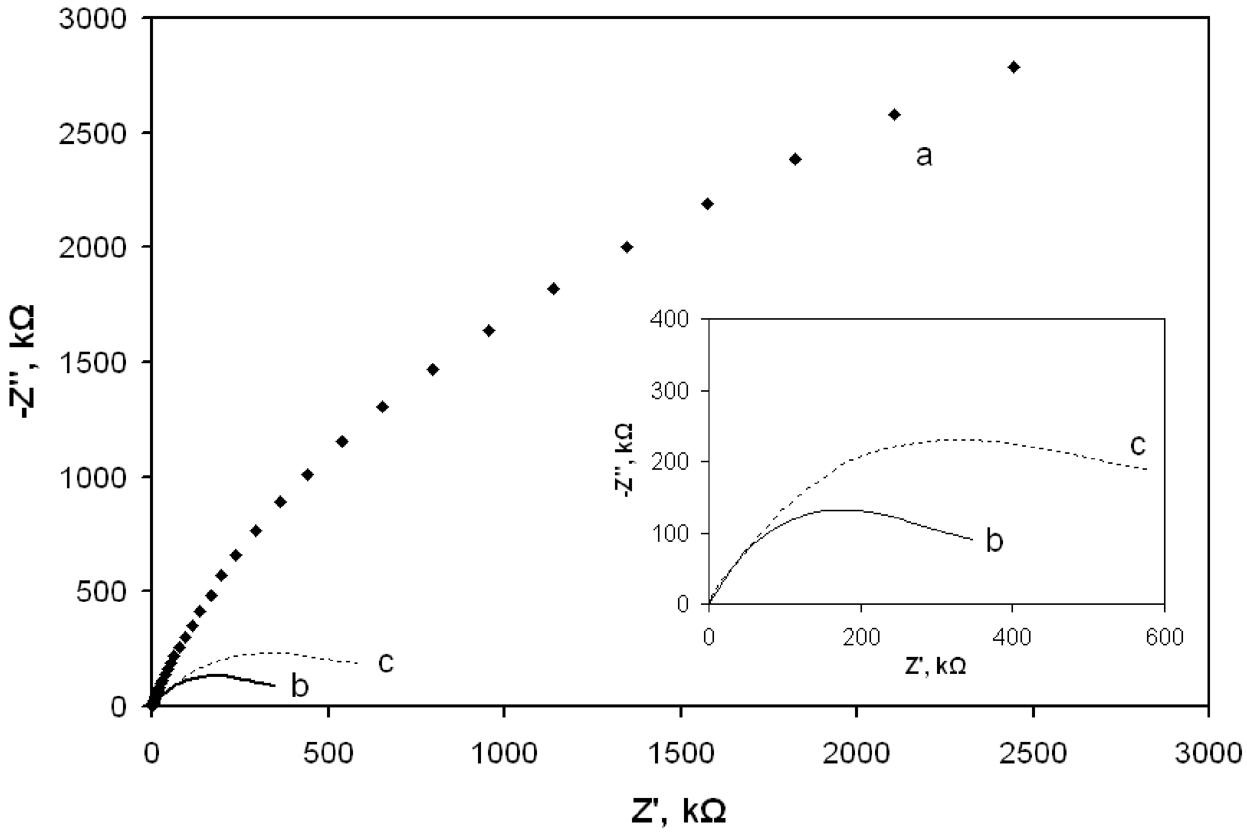

Figure 5.10 Complex impedance plots of a 0.001 M solution adsorbed *n*-octadecanethiol monolayer before (a) and after (b) site-selective reductive desorption. The monolayer was then backfilled in a 0.001 M solution of *n*-octadecanethiol for 15 minutes (c). Conditions: 0.005 M $[Fe(CN)_6]^{-3/-4}$ in 0.1 M KCl at pH 7.

These impedance findings are interesting because they provide evidence that generated gross defects on the microscopic scale can adversely affect the properties of self-assembled monolayers. These results parallel the work of the user-defined domain boundaries introduced by contact printing of Chapter 4. By creating two lines of exposed bare Au within a solution adsorbed *n*-octadecanethiol monolayer, we have essentially introduced four user-defined domain boundaries. Once backfilled, it is believed that these domain boundaries remain as defect sites and are responsible for the decreased impedance. The initial solution adsorbed monolayer is well-ordered and remains so during the desorption process, except at the desorption sites; therefore the impedance is directly related to the desorbed regions. Conversely, the patterned contact printed monolayer is initially disordered in which backfill molecules can saturate defect sites and increase the charge transfer resistance more dramatically; this convolutes the effects of domain boundaries on the electrochemical properties. SSRD provides a method to closely examine the effects of domain boundaries which more closely resemble those inherently formed in self-assembled monolayers.

Similar results were obtained for the backfill of site-selective reductive desorption of lines in *n*-octanethiol and *n*-dodecanethiol monolayers. The charge transfer resistance of solution adsorbed *n*-octanethiol decreased from 170 kΩ to 5 kΩ after SSRD. Following backfill in *n*-octanethiol the charge transfer resistance improved to 14 kΩ. The significant increase in charge transfer resistance after backfill supports adsorption of molecules to the desorbed lines. The *n*-dodecanethiol monolayers follow the same general trend. Charge transfer resistance of the solution adsorbed monolayer was 3.2 MΩ before desorption; it decreased to ~260 kΩ after the two lines were introduced and increased to ~460 kΩ after backfill in *n*-dodecanethiol. The impedance data for each of the three *n*-alkanethiol monolayers indicate that the user-defined domain boundaries introduced by site-selective reductive desorption cannot be fully compensated during backfill procedures.

5.3.3.2 Backfill SSRD Grid with 11-Mercaptoundecanoic Acid

Site-selective reductive desorption via scanning electrochemical microscopy was used produce a mixed-monolayer of *n*-dodecanethiol and 11-mercaptoundecanoic acid. A region was desorbed in a solution adsorbed *n*-dodecanethiol monolayer according to the scheme in Figure 5.11A and imaged by SECM after desorption, Figure 5.11B. Ruthenium hexaammine was used as the imaging redox probe because it was shown in Chapter 4 to image mixed monolayers of *n*-

dodecanethiol and 11-mercaptoundecanoic acid better than ferrocyanide due to the differences in electrochemical conductivity of the two thiol domains. The high current regions (5.7 nA) reflect the bare gold substrate where thiol has been reduced and removed, and the low current regions (4.8 nA) are the intact thiol domains where negative feedback is produced. The desorption scheme and resulting SECM image are slightly offset due to slight variations in the placement of the Pt microelectrode during desorption and imaging.

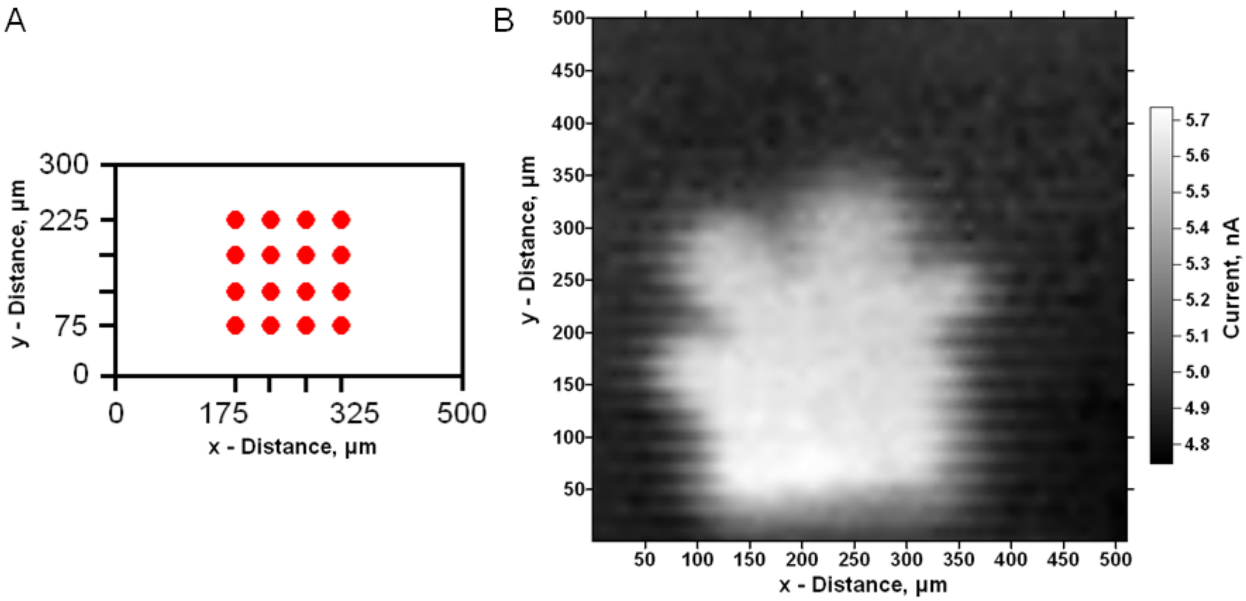

Figure 5.11 Desorption scheme (A) and SECM image of desorbed grid in solution adsorbed *n*-dodecanethiol (B). Overpotential of -1.0 V vs. Ag/AgCl held for 2 s at designated points in (A). Desorption and Imaging solution: 0.005 M $[Ru(NH_3)_6]^{+3}$, 0.1 M KCl, and 0.020 M KOH.

The effect of probe-substrate distance during site-selective reductive desorption is also apparent in Figure 5.11. As discussed previously, the substrate when placed in the SECM apparatus is not exactly level; therefore, the probe-substrate distance increases with increasing *y*-distance even as the *xyz* manipulator keeps the probe at a constant *z*-height. At small probe-substrate distances (*y* <100 µm), the desorbed area is clearly defined around the initial desorption point. At *y*-distances greater than 200 µm, where the probe-substrate distance has increased, patchy desorption exists. This is because at large probe-substrate distances, the local electric field between the Pt auxiliary electrode and Au substrate is effective over an extended area of the modified substrate, thus weakly adsorbed alkanethiol can be desorbed.

Electrochemical impedance spectroscopy was used to evaluate the modified substrate at each stage of the desorption procedure. Complex impedance plots are shown in Figure 5.12, and values of charge transfer resistance are summarized in Table 5.2. The unmodified *n*-dodecanethiol monolayer on Au has a very high charge transfer resistance of 5,900 kΩ, indicating a well-ordered monolayer with little defects. After the desorption of a 300x300 μm grid of *n*-dodecanethiol, the charge transfer resistance decreased by two orders of magnitude to 32 kΩ.

The shape of the complex impedance plot (Figure 5.12b) also differs from the previous results of Section 5.3.1. The two semicircles in the complex impedance plot of the previous generated Au "microelectrode" are not present here. Instead, a Warburg impedance line (with slope of 0.5) is observed at low frequency; this indicates that electron transfer occurs freely at the regenerated Au region where only mass transfer effects the impedance. One explanation for the observed differences in impedance plots of the desorbed grids in *n*-dodecanethiol monolayers is the size of the desorbed area. Here, the desorbed region is slightly larger, thus the exposed Au substrate behaves more like a macroelectrode rather than a microelectrode.

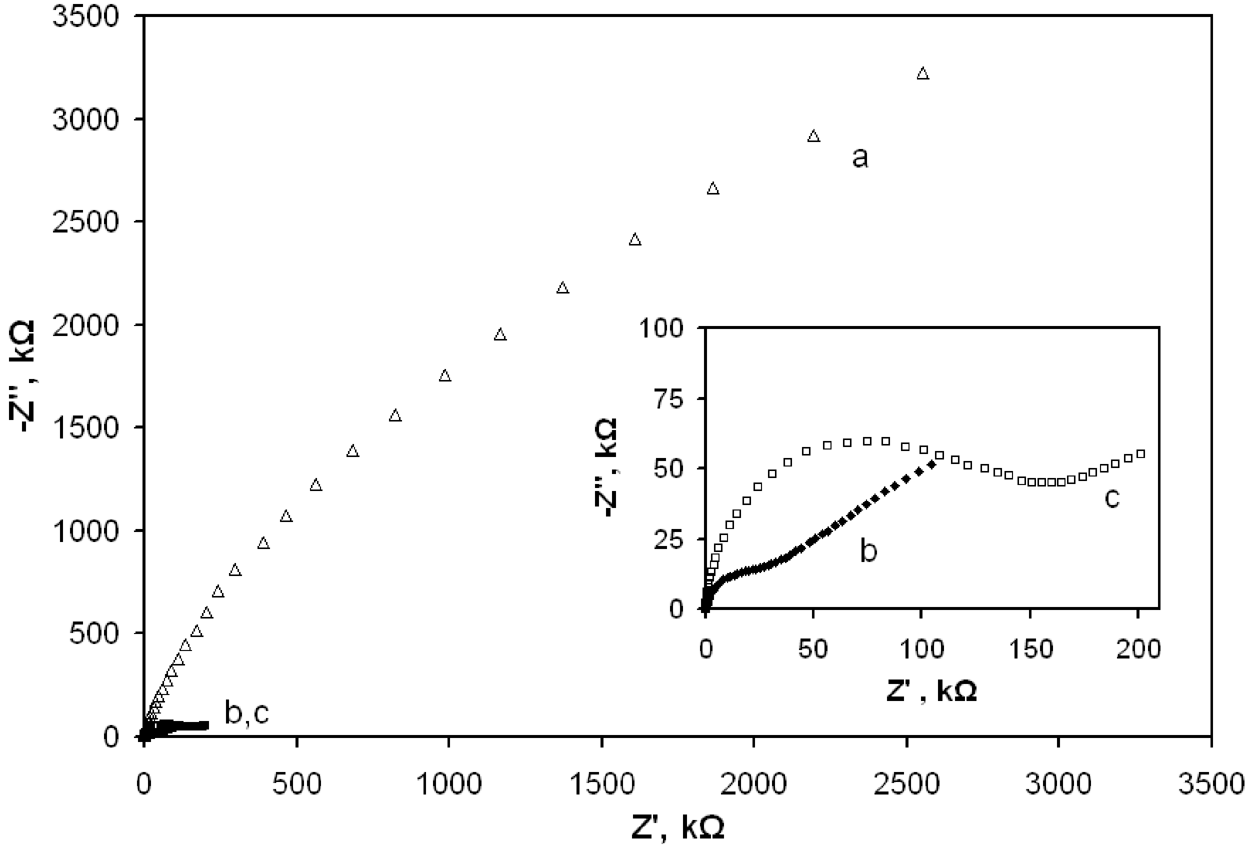

Figure 5.12 Complex impedance plots of solution adsorbed *n*-dodecanethiol prior to SSRD (a), after desorption of grid (b), and after backfill of desorbed grid with 11-mercaptoundecanoic acid (c). Inset shows detail of the lower impedance region. Conditions: 0.005 M $[Fe(CN)_6]^{-3/-4}$ in 0.1 M KCl at pH 7.

After site-selective reductive desorption, the *n*-dodecanethiol monolayer was placed in 0.001 M 11-mercaptoundecanoic acid for 15 minutes in order to backfill the exposed Au substrate. Adsorption of 11-MUA was confirmed by the increase in charge transfer resistance and a change in the shape of the complex impedance plot. The charge transfer resistance increased from 32 kΩ to 140 kΩ after backfill. This indicates that the newly adsorbed 11-MUA effectively blocks charge transfer at the previously desorbed region of *n*-dodecanethiol. The Warburg impedance line is significantly reduced after backfill, another indication that charge transfer is hindered at the desorbed region.

Monolayer	R_{ct} (kΩ)
n-Dodecanethiol	5,900±250
Desorbed Grid in *n*-Dodecanethiol	32±1
Desorbed Grid in n-Dodecanethiol Backfilled with 11-Mercaptoundecanoic Acid	140±3

Table 5.2 Summary of estimated charge transfer resistance values of site-selective reductive desorption and backfill of *n*-dodecanethiol monolayer.

The electrochemical conductivities of *n*-dodecanethiol and 11-mercaptoundecanoic acid differ when using a positive redox probe like ruthenium (III) hexaammine (see Section 4.3.4). This fact allows us to image a mixed-monolayer comprised of the two thiols by scanning electrochemical microscopy while using ruthenium (III) hexaammine as the redox probe. In this case, the mixed-monolayer was created by site-selective reductive desorption to generate an 11-mercaptoundecanoic acid island amid a *n*-dodecanethiol monolayer (Figure 5.13). The shape of the desorbed feature remains even though 11-MUA has been adsorbed to the exposed Au substrate. This result is consistent with the images of the multi-line *n*-dodecanethiol/11-mercaptoundecanoic acid pattern from Chapter 4 due to the differences in the electrochemical conductivity. The positive redox probe is attracted to the carboxylate terminal groups of 11-MUA regions and facilitates charge transfer readily. The high current region (6.1 nA) is due to positive feedback at 11-MUA covered domains. Negative feedback (4.0 nA) corresponds to *n*-dodecanethiol domains as described earlier. The observed current difference between *n*-dodecanethiol and 11-mercaptoundecanoic acid regions (~2.0 nA) is larger than that of the current difference between *n*-dodecanethiol and bare Au (~1.0 nA). The current difference was attributed to a change in the *z*-height of the Pt probe when the substrate was replaced after backfill. From the images, the *z*-height was determined to be smaller in Figure 5.13 because of the increased positive feedback over 11-MUA domains.

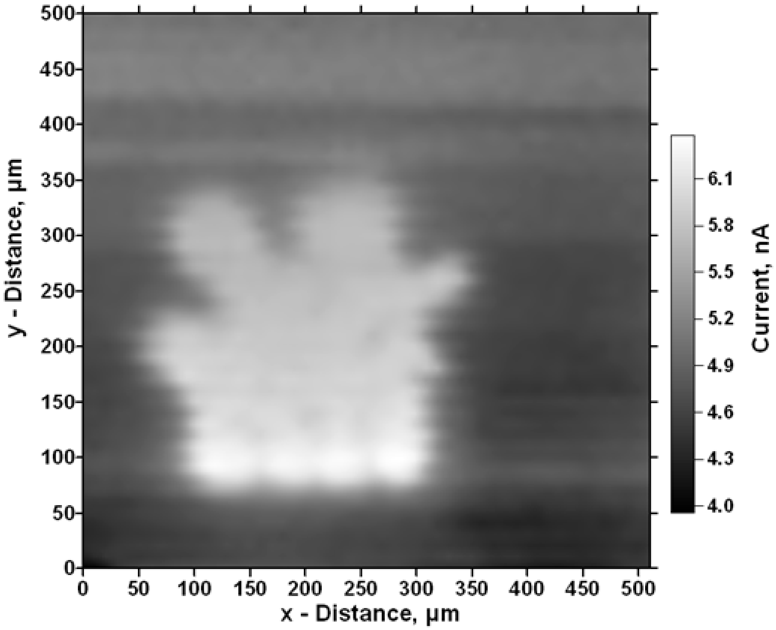

Figure 5.13 SECM image of desorbed grid in solution adsorbed *n*-dodecanethiol backfilled with 11-mercaptoundecanoic acid. Imaging solution: 0.005 M $[Ru(NH_3)_6]^{+3}$, 0.1 M KCl, and 0.020 M KOH.

The domain boundary perimeter of the 11-mercaptoundecanoic island in the *n*-dodecanethiol monolayer was estimated at 1.2 mm from the SECM image; this is similar to the estimated 2 mm user-defined domain boundary of the binary pattern of contact printed *n*-dodecanethiol and backfilled 11-mercaptoundecanioc acid (the diameter of the Au electrode is 2 mm), Section 4.3.1.1. Because the user-defined domain boundaries are within the same length range, we can compare the two studies. Both mixed-monolayers have an order of magnitude lower charge transfer resistance than pure solution adsorbed monolayers: R_{ct} = 772 kΩ for binary pattern of *n*-dodecanethiol/11-mercaptoundecanoic acid and R_{ct} = 2,000 kΩ for solution adsorbed 11-MUA from Section 4.3.1.1; R_{ct} = 140 kΩ for SSRD grid of *n*-dodecanethiol/11-MUA and R_{ct} = 5,900 kΩ for immersion formed *n*-dodecanethiol. From these results, it can be concluded that user-defined domain boundaries of 1-2 mm in length adversely affect the electrochemical properties of the modified substrate and decrease the charge transfer resistance by an order of magnitude.

Essentially, by introducing a pattern, we have introduced large defects into the interfacial structure which impact the properties.

5.4 Conclusions

Scanning electrochemical microscopy can be used to create patterns in self-assembled monolayers by site-selective reductive desorption. Impedance and CV measurements confirm that the renewed Au regions created by SSRD behave as microelectrodes if the desorbed region is small. The size and shape of the desorbed features depends on factors such as probe-substrate distance and hydrocarbon chain length of adsorbed alkanethiol. These variables as well as desorption potential and ionic strength can be adjusted to generate the desired feature size. The most fascinating result was that generated “defects” of micrometer lengths negatively impact the impedance.

The site-selective reductive desorption generated user-defined domain boundaries decrease the observed charge transfer resistance of homo- and heterogeneous patterned self-assembled monolayers compared to solution adsorbed monolayers. The impedance of a monolayer with SSRD features decreased from the initial value as expected. During the backfill step, thiol molecules adsorb to the bare Au regions renewed during SSRD; however, the impedance does not return to its prior value because user-defined domain boundaries are present. These defects allow charge transfer to occur more readily than at the initial well-ordered domains, in turn decreasing the charge transfer resistance. The extent of user-defined domain boundaries must be considered when patterning interfaces by scanning electrochemical microscopy.

SECM as an interfacial patterning method does have disadvantages. Because SECM is a scanning lithography method, it does require extensive time to fabricate patterns. Like any patterning method, SSRD generates user-defined domain boundaries which cannot be recovered fully during backfill procedures. Yet again, we find that patterning introduces more interfacial defects and compromises the quality of the resulting monolayer.

Chapter 6

Summary and Future Work

6.1 Summary

The main goal of this dissertation was to determine the effects of introducing interfacial patterns in self-assembled monolayer-modified substrates on their electrochemical properties. The presented work considered the patterning methods of contact printing and site-selective reductive desorption by scanning electrochemical microscopy. By patterning a surface, domain boundary defects are formed where two patterned thiol domains converge. We find that it is these user-defined domain boundary defects that adversely affect the electrochemical behavior of monolayer-modified substrates.

The structure and properties of homogeneous contact printed self-assembled monolayers were investigated before patterning the surface. Contact printed *n*-octadecanethiol monolayers appeared to have similar structure to solution adsorbed *n*-octadecanethiol as evidenced from infrared spectroscopy and cyclic voltammetry; however, the electrochemical impedance results differed significantly between preparation methods. Low charge transfer resistance values were obtained for contact printed monolayers compared to immersion formed SAMs even when using high thiol ink concentrations during printing. Similar results were found with other thiols, like *n*-dodecanethiol, *n*-pentanethiol, and 11-mercaptoundecanoic acid. The impedance results indicate that contact printed monolayers contain more interfacial defects than monolayers prepared from solution. The defect density was estimated based on the model which considers the defects as an array of microelectrodes. The difference in defect density between the preparation methods was considered for the *n*-pentanethiol system. It was shown that contact printed *n*-pentanethiol monolayers do have more defects than immersion formed *n*-pentanethiol monolayers. In a sense, without any structural pattern, contact printing introduces more defects in the prepared monolayer.

When creating binary patterned monolayers by contact printing followed by backfill in solution, two key observations were noted: 1) user-defined domain boundaries negatively impact the electrochemical impedance, and 2) the backfill molecules saturate the defects present in the contact printed monolayers. Binary patterned monolayers produced charge transfer resistance values intermediate of homogeneous standard contact printed and immersion monolayers. These results were expected because the binary pattern is a combination of the two preparation methods; however, the impedance of the binary patterned monolayers were more similar to the immersion formed SAM. This detail was investigated by backfill of homogeneous contact printed monolayers. Charge transfer resistance increased when contact printed *n*-dodecanethiol monolayers were backfilled with either *n*-dodecanethiol or 11-mercaptoundecanoic acid, indicating that defects were saturated by the backfill molecules. With this knowledge, it can be assumed that when patterned contact printed monolayers are placed into solution to complete the interfacial structure, backfill molecules will taint the distinctly defined regions which negates the initial reason for patterning. The charge transfer resistance of the binary pattern did not approach the value of the standard solution adsorbed monolayer which implicated that the user-defined domain boundary remained a defect where charge transfer occurs readily.

Scanning electrochemical microscopy was used to both image and pattern self-assembled monolayers. We found that defects within self-assembled monolayers and at domain boundaries are not apparent in SECM images due to the limited resolution of the instrument. Mixed monolayers of *n*-dodecanethiol and 11-mercaptoundecanoic acid were successfully imaged using a positive redox probe because of the difference in electrochemical conductivity between thiol domains. Patterning self-assembled monolayers was accomplished by site-selective reductive desorption.

Using site-selective reductive desorption, small areas of adsorbed thiol are removed, and the regions of renewed Au substrate can be considered as vast defects within the monolayer. From electrochemical results, it was shown that SSRD generated "defects" behave like microelectrodes, according to the sigmoidal cyclic voltammetry response and the two semicircles present in the complex impedance plot. The desorption is self-limiting and depends on the size of the probe and the probe-substrate separation distance. Feature size and shape also depends on the alkanethiol chain length. Larger features were produced consistently at greater probe-substrate distances and for shorter alkanethiol chain lengths.

The backfill of site-selective reductive desorption modified monolayers gave insight into the backfill of patterned monolayers formed by contact printing. The impedance of monolayers with "defects" created by SSRD increased only slightly after backfill in solution. The initial solution adsorbed monolayer was essentially defect-free prior to modification, thus the change in impedance is directly related to the desorption and backfill. However, patterned contact printed monolayers are not defect-free and the large change in charge transfer resistance after backfill is attributed mostly to the saturation of defect sites within the contact printed monolayer. Unless the defects in contact printed monolayers can be minimized, site-selective desorption is the better method to investigate the impact of domain boundaries on electrochemical properties of the monolayers.

Domain boundary defects were created by patterning methods to exaggerate their impact on overall monolayer properties. From the presented work, domain boundary defects were shown to negatively affect the characteristic electron blocking behavior of self-assembled monolayers. Increasing the number of user-defined domain boundaries decreases the impedance of the patterned monolayer. These domain boundary defects remain after backfill procedures to modify remaining exposed Au substrate. Any interfacial pattern will have user-defined domain boundaries, thus the resulting monolayer will have greater amounts of defects.

6.2 Future Work

One area of the research worth considering is the role of the elastomeric stamp in the formation of defects in contact printed self-assembled monolayers. During stamp preparation, the poly(dimethyl siloxane) elastomer does not cure completely. This leaves low molecular weight polymers that could potentially leach out of the stamp during the ink process and be transferred to the substrate. The elastomeric residues could compete with the adsorption of thiol molecules and result in disordered, low surface coverage monolayers. A systematic study of using different rinsing procedures to expel any low molecular weight polymer from the stamp prior to printing is needed. Surface sensitive spectroscopy methods could be used to detect the presence of silicon species on the surface, like reflection-absorption infrared spectroscopy and X-ray photoelectron spectroscopy.

Another area to expand this research would be to fabricate more complex stamp masters with smaller features (i.e. in the micrometer range). Patterned monolayers made from these stamp masters could then be directly compared to monolayers formed by site-selective reductive desorption (which can also create patterns at micrometer scales). It would be interesting to compare the electrochemical impedance as a function of the number of user-defined domain boundaries in a systematic study. This task was accomplished in the dissertation, but because high resolution stamp master fabrication was beyond our means at the time, a maximum of only four user-defined domain boundaries was obtained for contact printing. Conventional lithographic methods could be used to fabricate stamp masters with more user-defined domain boundaries. Complex patterns would be additional support of the findings presented for the effects of user-defined domain boundaries.

Scanning electrochemical microscopy proved to be insufficient in imaging defects and domain boundaries within patterned self-assembled monolayers because of the small size of the defects. Other techniques like atomic force microscopy and scanning tunneling microscopy would provide greater resolution to study the pattern-generated defects. One could determine if the user-defined domain boundaries are larger than the inherent domain boundaries formed during adsorption. The system would have to be transitioned from preparing monolayers on Au disk electrodes to Au on mica in order to image the monolayer structures with clarity.

References

1. Love, J. C.; Estroff, L. A.; Kriebel, J. K.; Nuzzo, R. G.; Whitesides, G. M., Self-Assembled Monolayers of Thiolates on Metals as a Form of Nanotechnology. *Chem. Rev.* **2005,** 105, (4), 1103-1170.
2. Kumar, A.; Whitesides, G. M., Features of gold having micrometer to centimeter dimensions can be formed through a combination of stamping with an elastomeric stamp and an alkanethiol \"ink\" followed by chemical etching. *Applied Physics Letters* **1993,** 63, (14), 2002-4.
3. Nix, R. M. An Introduction to Surface Chemistry. http://www.chem.qmul.ac.uk/surfaces/scc/ (October 16),
4. Ulman, A.; Eilers, J. E.; Tillman, N., Packing and molecular orientation of alkanethiol monolayers on gold surfaces. *Langmuir* **1989,** 5, (5), 1147-52.
5. Swalen, J. D.; Allara, D. L.; Andrade, J. D.; Chandross, E. A.; Garoff, S.; Israelachvili, J.; McCarthy, T. J.; Murray, R.; Pease, R. F.; et al., Molecular monolayers and films. A panel report for the Materials Sciences Division of the Department of Energy. *Langmuir* **1987,** 3, (6), 932-50.
6. Vericat, C.; Vela, M. E.; Salvarezza, R. C., Self-assembled monolayers of alkanethiols on Au(111): surface structures, defects and dynamics. *Physical Chemistry Chemical Physics* **2005,** 7, (18), 3258-3268.
7. Widrig, C. A.; Chung, C.; Porter, M. D., The electrochemical desorption of n-alkanethiol monolayers from polycrystalline Au and Ag electrodes. *J. Electroanal. Chem.* **1991,** 310, 335-359.
8. Walczak, M. M.; Popenoe, D. D.; Deinhammer, R. S.; Lamp, B. D.; Chung, C.; Porter, M. D., Reductive Desorption of Alkanethiolate Monolayers at Gold: A Measure of Surface Coverage. *Langmuir* **1991,** 7, 2687-2693.
9. Sanders, W.; Anderson, M. R., Electrostatic deposition of polycations and polyanions onto cysteine monolayers. *Journal of Colloid and Interface Science* **2009,** 331, (2), 318-321.
10. Tian, Y.; Mao, L.; Okajima, T.; Ohsaka, T., Electrochemistry and Electrocatalytic Activities of Superoxide Dismutases at Gold Electrodes Modified with a Self-Assembled Monolayer. *Analytical Chemistry* **2004,** 76, (14), 4162-4168.
11. Ge, B.; Scheller, F. W.; Lisdat, F., Electrochemistry of immobilized CuZnSOD and FeSOD and their interaction with superoxide radicals. *Biosensors & Bioelectronics* **2003,** 18, (2-3), 295-302.
12. Fragoso, A.; Laboria, N.; Latta, D.; O'Sullivan, C. K., Electron Permeable Self-Assembled Monolayers of Dithiolated Aromatic Scaffolds on Gold for Biosensor Applications. *Analytical Chemistry* **2008,** 80, (7), 2556-2563.
13. Bard, A. J.; Faulkner, L. R., *Electrochemical Methods: Fundamentals and Applications*. Second ed.; John Wiley and Sons, Inc.: New York, 2001; p 833.
14. Honeychurch, M. J.; Rechnitz, G. A., Voltammetry of adsorbed molecules. Part 1: Reversible redox systems. *Electroanalysis* **1998,** 10, (5), 285-293.
15. Porter, M. D.; Bright, T. B.; Allara, D. L.; Chidsey, C. E. D., Spontaneously organized molecular assemblies. 4. Structural characterization of n-alkyl thiol monolayers on gold by optical ellipsometry, infrared spectroscopy, and electrochemistry. *Journal of the American Chemical Society* **1987,** 109, (12), 3559-68.
16. Nuzzo, R. G.; Dubois, L. H.; Allara, D. L., Fundamental studies of microscopic wetting on organic surfaces. 1. Formation and structural characterization of a self-consistent series of

polyfunctional organic monolayers. *Journal of the American Chemical Society* **1990,** 112, (2), 558-69.

17. Finklea, H. O.; Avery, S.; Lynch, M.; Furtsch, T., Blocking oriented monolayers of alkyl mercaptans on gold electrodes. *Langmuir* **1987,** 3, (3), 409-13.

18. Poirier, G., Characterization of Organosulfur Molecular Monolayers on Au(111) using Scanning Tunneling Microscopy. *Chem. Rev.* **1997,** 97, (4), 1117-1128.

19. Poirier, G. E.; Pylant, E. D., The self-assembly mechanism of alkanethiols on Au(111). *Science (Washington, D. C.)* **1996,** 272, (5265), 1145-1148.

20. Finklea, H. O., Electrochemistry of Organized Monolayers of Thiols and Related Molecules on Electrodes. In *Electroanalytical Chemistry*, Bard, A. J.; Rubinstein, I., Eds. Marcel Dekker: New York, 1996; Vol. 19, pp 109-335.

21. Lewis, P. A.; Smith, R. K.; Kelly, K. F.; Bumm, L. A.; Reed, S. M.; Clegg, R. S.; Gunderson, J. D.; Hutchison, J. E.; Weiss, P. S., The role of buried hydrogen bonds in self-assembled mixed composition thiols on Au{111}. *Journal of Physical Chemistry B* **2001,** 105, (43), 10630-10636.

22. Smith, R. K.; Reed, S. M.; Lewis, P. A.; Monnell, J. D.; Clegg, R. S.; Kelly, K. F.; Bumm, L. A.; Hutchison, J. E.; Weiss, P. S., Phase separation within a binary self-assembled monolayer on Au{111} driven by an amide-containing alkanethiol. *Journal of Physical Chemistry B* **2001,** 105, (6), 1119-1122.

23. Clegg, R. S.; Reed, S. M.; Smith, R. K.; Barron, B. L.; Rear, J. A.; Hutchison, J. E., The interplay of lateral and tiered interactions in stratified self-organized molecular assemblies. *Langmuir* **1999,** 15, (26), 8876-8883.

24. Clegg, R. S.; Reed, S. M.; Hutchison, J. E., Self-assembled monolayers stabilized by three-dimensional networks of hydrogen bonds. *Journal of the American Chemical Society* **1998,** 120, (10), 2486-2487.

25. Finklea, H. O.; Snider, D. A.; Fedyk, J.; Sabatani, E.; Gafni, Y.; Rubinstein, I., Characterization of octadecanethiol-coated gold electrodes as microarray electrodes by cyclic voltammetry and ac impedance spectroscopy. *Langmuir* **1993,** 9, (12), 3660-3667.

26. Diao, P.; Guo, M.; Jiang, D.; Jia, Z.; Cui, X.; Gu, D.; Tong, R.; Zhong, B., Fractional coverage of defects in self-assembled thiol monolayers on gold. *Journal of Electroanalytical Chemistry* **2000,** 480, (1,2), 59-63.

27. Boubour, E.; Lennox, R. B., Insulating Properties of Self-Assembled Monolayers Monitored by Impedance Spectroscopy. *Langmuir* **2000,** 16, (9), 4222-4228.

28. Munakata, H.; Kuwabata, S.; Ohko, Y.; Yoneyama, H., Spatial distribution of domains in binary self-assembled monolayers of thiols having different lengths. *Journal of Electroanalytical Chemistry* **2001,** 496, (1-2), 29-36.

29. Brewer, N. J.; Leggett, G. J., Chemical Force Microscopy of Mixed Self-Assembled Monolayers of Alkanethiols on Gold: Evidence for Phase Separation. *Langmuir* **2004,** 20, (10), 4109-4115.

30. Nelles, G.; Schonherr, H.; Jaschke, M.; Wolf, H.; Schaub, M.; Kuther, J.; Tremel, W.; Bamberg, E.; Ringsdorf, H.; Butt, H. J., Two-dimensional structure of disulfides and thiols on gold(111). *Langmuir* **1998,** 14, (4), 808-815.

31. Chen, S. F.; Li, L. Y.; Boozer, C. L.; Jiang, S. Y., Controlled chemical and structural properties of mixed self-assembled monolayers by coadsorption of symmetric and asymmetric disulfides on Au(111). *Journal of Physical Chemistry B* **2001,** 105, (15), 2975-2980.

32. Bumm, L. A.; Arnold, J. J.; Charles, L. F.; Dunbar, T. D.; Allara, D. L.; Weiss, P. S., Directed self-assembly to create molecular terraces with molecularly sharp boundaries in organic monolayers. *Journal of the American Chemical Society* **1999,** 121, (35), 8017-8021.

33. Laibinis, P. E.; Fox, M. A.; Folkers, J. P.; Whitesides, G. M., Comparisons of Self-Assembled Monolayers on Silver and Gold - Mixed Monolayers Derived from $HS(CH_2)_{21}X$ and $HS(CH_2)_{10}Y$ (X, Y = CH_3, CH_2OH) Have Similar Properties. *Langmuir* **1991,** 7, (12), 3167-3173.

34. Bain, C. D.; Whitesides, G. M., Correlations between Wettability and Structure in Monolayers of Alkanethiols Adsorbed on Gold. *Journal of the American Chemical Society* **1988,** 110, (11), 3665-3666.

35. Kakiuchi, T.; Sato, K.; Iida, M.; Hobara, D.; Imabayashi, S.-i.; Niki, K., Phase Separation of Alkanethiol Self-Assembled Monolayers during the Replacement of Adsorbed Thiolates on Au(111) with Thiols in Solution. *Langmuir* **2000,** 16, (18), 7238-7244.

36. Chidsey, C. E. D.; Bertozzi, C. R.; Putvinski, T. M.; Mujsce, A. M., Coadsorption of ferrocene-terminated and unsubstituted alkanethiols on gold: electroactive self-assembled monolayers. *Journal of the American Chemical Society* **1990,** 112, (11), 4301-6.

37. Bain, C. D.; Whitesides, G. M., Molecular-Level Control over Surface Order in Self-Assembled Monolayer Films of Thiols on Gold. *Science* **1988,** 240, (4848), 62-63.

38. Piner, R. D.; Zhu, J.; Xu, F.; Hong, S. H.; Mirkin, C. A., "Dip-pen" nanolithography. *Science* **1999,** 283, (5402), 661-663.

39. Kumar, A.; Abbott, N. L.; Biebuyck, H. A.; Kim, E.; Whitesides, G. M., Patterned Self-Assembled Monolayers and Meso-Scale Phenomena. *Accounts of Chemical Research* **1995,** 28, (5), 219-26.

40. Kumar, A.; Biebuyck, H. A.; Whitesides, G. M., Patterning Self-Assembled Monolayers: Applications in Materials Science. *Langmuir* **1994,** 10, 1498-1511.

41. Wilhelm, T.; Wittstock, G., Patterns of functional proteins formed by local electrochemical desorption of self-assembled monolayers. *Electrochimica Acta* **2001,** 47, (1-2), 275-281.

42. Wittstock, G.; Hesse, R.; Schuhmann, W., Patterned self-assembled alkanethiolate monolayers on gold. Patterning and imaging by means of scanning electrochemical microscopy. *Electroanalysis* **1997,** 9, (10), 746-750.

43. Wittstock, G.; Schuhmann, W., Formation and Imaging of Microscopic Enzymically Active Spots on an Alkanethiolate-Covered Gold Electrode by Scanning Electrochemical Microscopy. *Analytical Chemistry* **1997,** 69, (24), 5059-5066.

44. Roach, D. M. Novel Applications of Scanning Electrochemical Microscopy. Virginia Polytechnic Institute and State University, Blacksburg, 2005.

45. Xia, Y. N.; Whitesides, G. M., Extending microcontact printing as a microlithographic technique. *Langmuir* **1997,** 13, (7), 2059-2067.

46. Bohm, I.; Lampert, A.; Buck, M.; Eisert, F.; Grunze, M., A spectroscopic study of thiol layers prepared by contact printing. *Applied Surface Science* **1999,** 141, (3-4), 237-243.

47. Delamarche, E.; Schmid, H.; Bietsch, A.; Larsen, N. B.; Rothuizen, H.; Michel, B.; Biebuyck, H., Transport Mechanisms of Alkanethiols during Microcontact Printing on Gold. *Journal of Physical Chemistry B* **1998,** 102, (18), 3324-3334.

48. Larsen, N. B.; Biebuyck, H.; Delamarche, E.; Michel, B., Order in Microcontact Printed Self-Assembled Monolayers. *Journal of the American Chemical Society* **1997,** 119, (13), 3017-3026.

49. Fischer, D.; Marti, A.; Hahner, G., Orientation and order in microcontact-printed, self-assembled monolayers of alkanethiols on gold investigated with near edge x-ray absorption fine structure spectroscopy. *Journal of Vacuum Science & Technology, A: Vacuum, Surfaces, and Films* **1997,** 15, (4), 2173-2180.

50. Eberhardt, A. S.; Nyquist, R. M.; Parikh, A. N.; Zawodzinski, T.; Swanson, B. I., Defects in Microcontact-Printed and Solution-Grown Self-Assembled Monolayers. *Langmuir* **1999,** 15, (5), 1595-1598.

51. Losic, D.; Shapter, J. G.; Gooding, J. J., Influence of surface topography on alkanethiol SAMs assembled from solution and by microcontact printing. *Langmuir* **2001,** 17, (11), 3307-3316.

52. Losic, D.; Shapter, J. G.; Gooding, J. J., Mapping of defects in self-assembled monolayers by polymer decoration. *Journal of Solid State Electrochemistry* **2005,** 9, (7), 512-519.

53. Losic, D.; Shapter, J. G.; Gooding, J. J., Concentration dependence in microcontact printing of self-assembled monolayers (SAMs) of alkanethiols. *Electrochemistry Communications* **2001,** 3, (12), 722-726.

54. Zhang, Y.; Salaita, K.; Lim, J. H.; Mirkin, C. A., Electrochemical whittling of organic nanostructures. *Nano Letters* **2002,** 2, (12), 1389-1392.

55. Zhang, Y.; Salaita, K.; Lim, J. H.; Lee, K. B.; Mirkin, C. A., A massively parallel electrochemical approach to the miniaturization of organic micro- and nanostructures on surfaces. In *Langmuir*, 2004; Vol. 20, pp 962-968.

56. Lee, S. W.; Oh, B.-K.; Sanedrin, R. G.; Salaita, K.; Fujigaya, T.; Mirkin, C. A., Biologically active protein nanoarrays generated using parallel dip-pen nanolithography. *Advanced Materials (Weinheim, Germany)* **2006,** 18, (9), 1133-1136.

57. Degenhart, G. H.; Dordi, B.; Schonherr, H.; Vancso, G. J., Micro- and nanofabrication of robust reactive arrays based on the covalent coupling of dendrimers to activated monolayers. *Langmuir* **2004,** 20, (15), 6216-6224.

58. Chidsey, C. E. D.; Loiacono, D. N., Chemical functionality in self-assembled monolayers: structural and electrochemical properties. *Langmuir* **1990,** 6, (3), 682-91.

59. Hollas, J. M., *Modern Spectroscopy*. Third ed.; John Wiley & Sons: Chichester, 1996; p 391.

60. Atre, S. V.; Liedberg, B.; Allara, D. L., Chain-Length Dependence of the Structure and Wetting Properties in Binary Composition Monolayers of OH-Terminated and CH_3-Terminated Alkanethiolates on Gold. *Langmuir* **1995,** 11, (10), 3882-3893.

61. Basics of Electrochemical Impedance Spectroscopy. In Princeton Applied Research.

62. Loveday, D.; Peterson, P.; Rodgers, B., Evaluation of organic coatings with electrochemical impedance spectroscopy. Part 1: fundamentals of electrochemical impedance spectroscpy. *JCT CoatingsTech* **2004,** 1, (8), 46-52.

63. Gabrielli, C., Electrochemical Impedance Spectroscopy: Principles, Instrumentation, and Applications. In *Physical Electrochemistry*, Rubinstein, I., Ed. Marcel Dekker, Inc.: New York, 1995; p 583.

64. Bard, A. J.; Fan, F. R. F.; Kwak, J.; Lev, O., Scanning electrochemical microscopy. Introduction and principles. *Analytical Chemistry* **1989,** 61, (2), 132-8.

65. Bard, A. J.; Mirkin, M. V., *Scanning Electrochemical Microscopy*. Marcel Dekker, Inc.: New York, NY, 2001; p 638.

66. Roach, D. M.; Hooper, S. E.; Anderson, M. R., Optimization of electrode alignment for electrochemical detection in capillary electrophoresis using a scanning electrochemical microscope. *Electroanalysis* **2005,** 17, (24), 2254-2259.

67. Greenler, R. G., Infrared study of adsorbed molecules on metal surfaces by reflection techniques. *Journal of Chemical Physics* **1966,** 44, (1), 310-15.

68. Janek, R. P.; Fawcett, W. R.; Ulman, A., Impedance Spectroscopy of Self-Assembled Monolayers on Au(111): Sodium Ferrocyanide Charge Transfer at Modified Electrodes. *Langmuir* **1998,** 14, (11), 3011-3018.

69. Diao, P.; Guo, M.; Tong, R., Characterization of defects in the formation process of self-assembled thiol monolayers by electrochemical impedance spectroscopy. *Journal of Electroanalytical Chemistry* **2001,** 495, (2), 98-105.

70. Bensebaa, F.; L'Ecuyer, P.; Faid, K.; Py, C.; Tague, T. J.; Jackson, R. S., Grazing angle infrared microspectroscopy of micropatterned self-assembled monolayers. *Applied Surface Science* **2005,** 243, (1-4), 238-244.

71. Campuzano, S.; Pedrero, M.; Montemayor, C.; Fatas, E.; Pingarron, J. M., Characterization of alkanethiol-self-assembled monolayers-modified gold electrodes by electrochemical impedance spectroscopy. *Journal of Electroanalytical Chemistry* **2006,** 586, (1), 112-121.

72. Sanders, W.; Anderson, M. R., Potential Driven Deposition of Poly(diallyldimethylammonium chloride) onto the Surface of 3-Mercaptopropionic Acid Monolayers Assembled on Gold. *Langmuir* **2008,** 24, (22), 12766-12770.

73. Sanders, W.; Vargas, R.; Anderson, M. R., Characterization of Carboxylic Acid-Terminated Self-Assembled Monolayers by Electrochemical Impedance Spectroscopy and Scanning Electrochemical Microscopy. *Langmuir* **2008,** 24, (12), 6133-6139.

74. Douglass Jr, E. F.; Driscoll, P. F.; Liu, D.; Burnham, N. A.; Lambert, C. R.; McGimpsey, W. G., Effect of Electrode Roughness On the Capacitive Behavior of Self-Assembled Monolayers. **2008,** 80, (20), 7670-7677.

75. Imabayashi, S.-i.; Iida, M.; Hobara, D.; Feng, Z. Q.; Niki, K.; Kakiuchi, T., Reductive desorption of carboxylic-acid-terminated alkanethiol monolayers from Au(111) surfaces. *Journal of Electroanalytical Chemistry* **1997,** 428, (1-2), 33-38.

76. Gorman, C. B.; He, Y.; Carroll, R. L., The Influence of Headgroup on the Structure of Self-Assembled Monolayers As Viewed by Scanning Tunneling Microscopy. *Langmuir* **2001,** 17, (17), 5324-5328.

77. Sprik, M.; Delamarche, E.; Michel, B.; Roethlisberger, U.; Klein, M. L.; Wolf, H.; Ringsdorf, H., Structure of Hydrophilic Self-Assembled Monolayers: A Combined Scanning Tunneling Microscopy and Computer Simulation Study. *Langmuir FIELD Full Journal Title:Langmuir* **1994,** 10, (11), 4116-30.

78. Amatore, C.; Saveant, J. M.; Tessier, D., Charge transfer at partially blocked surfaces. A model for the case of microscopic active and inactive sites. *Journal of Electroanalytical Chemistry and Interfacial Electrochemistry* **1983,** 147, (1-2), 39-51.

79. Campina, J. M.; Martins, A.; Silva, F., Selective Permeation of a Liquidlike Self-Assembled Monolayer of 11-Amino-1-undecanethiol on Polycrystalline Gold by Highly Charged Electroactive Probes. *J. Phys. Chem. C* **2007,** 111, (14), 5351-5362.

80. Stackelberg, M. V.; Pilgram, M.; Toome, V., Determination of diffusion coefficients of several ions in aqueous solution in the presence of foreign electrolytes. I. *Zeitschrift fuer Elektrochemie und Angewandte Physikalische Chemie* **1953,** 57, 342-50.

81. Bain, C. D.; Troughton, E. B.; Tao, Y. T.; Evall, J.; Whitesides, G. M.; Nuzzo, R. G., Formation of monolayer films by the spontaneous assembly of organic thiols from solution onto gold. *Journal of the American Chemical Society* **1989,** 111, (1), 321-335.

82. Mullen, T. J.; Zhang, P.; Srinivasan, C.; Horn, M. W.; Weiss, P. S., Combining electrochemical desorption and metal deposition on patterned self-assembled monolayers. *Journal of Electroanalytical Chemistry* **2008,** 621, (2), 229-237.

83. Vergheese, T. M.; Berchmans, S., Evaluation of monolayers and mixed monolayers formed from mercaptobenzothiazole and decanethiol as sensing platforms. *Materials Chemistry and Physics* **2004,** 83, (2-3), 229-238.

84. Sawaguchi, T.; Sato, Y.; Mizutani, F., In situ STM imaging of individual molecules in two-component self-assembled monolayers of 3-mercaptopropionic acid and 1-decanethiol on Au(111). *Journal of Electroanalytical Chemistry* **2001,** 496, (1-2), 50-60.

85. Folkers, J. P.; Laibinis, P. E.; Whitesides, G. M.; Deutch, J., Phase behavior of two-component self-assembled monolayers of alkanethiolates on gold. *Journal of Physical Chemistry* **1994,** 98, (2), 563-71.

86. Hobara, D.; Sasaki, T.; Imabayashi, S.-i.; Kakiuchi, T., Surface Structure of Binary Self-Assembled Monolayers Formed by Electrochemical Selective Replacement of Adsorbed Thiols. *Langmuir* **1999,** 15, (15), 5073-5078.

87. Kakiuchi, T.; Iida, M.; Gon, N.; Hobara, D.; Imabayashi, S.-i.; Niki, K., Miscibility of adsorbed 1-undecanethiol and 11-mercaptoundecanoic acid species in binary self-assembled monolayers on Au(111). *Langmuir* **2001,** 17, (5), 1599-1603.

88. Arnold, S.; Feng, Z. Q.; Kakiuchi, T.; Knoll, W.; Niki, K., Investigation of the electrode reaction of cytochrome c through mixed self-assembled monolayers of alkanethiols on gold(111) surfaces. *Journal of Electroanalytical Chemistry* **1997,** 438, (1-2), 91-97.

89. Xing, Y. F.; Li, S. F. Y.; Lau, A. K. H.; O'Shea, S. J., Electrochemical impedance spectroscopy study of mixed thiol monolayers on gold. *Journal of Electroanalytical Chemistry* **2005,** 583, (1), 124-132.

90. Cimatu, K.; Baldelli, S., Sum Frequency Generation Microscopy of Microcontact-Printed Mixed Self-Assembled Monolayers. *Journal of Physical Chemistry B* **2006,** 110, (4), 1807-1813.

91. Cimatu, K.; Moore, H. J.; Lee, T. R.; Baldelli, S., Sum Frequency Generation Imaging of Microcontact-Printed Monolayers Derived from Aliphatic Dithiocarboxylic Acids: Contrast Based on Terminal-Group Orientation. *Journal of Physical Chemistry C* **2007,** 111, (32), 11751-11755.

92. Cimatu, K.; Moore, H. J.; Barriet, D.; Chinwangso, P.; Lee, T. R.; Baldelli, S., Sum Frequency Generation Imaging Microscopy of Patterned Self-Assembled Monolayers with Terminal -CH3, -OCH3, -CF2CF3, -C=C, -Phenyl, and -Cyclopropyl Groups. *Journal of Physical Chemistry C* **2008,** 112, (37), 14529-14537.

93. Cui, X.; Jiang, D.; Diao, P.; Li, J.; Tong, R.; Wang, X., Assessing the apparent effective thickness of alkanethiol self-assembled monolayers in different concentrations of Fe(CN)63-/Fe(CN)64- by ac impedance spectroscopy. *Journal of Electroanalytical Chemistry* **1999,** 470, (1), 9-13.

94. Sanders, W. C. Examining the Effects of Applied Potential on the Surface Charge of Functionalized Monolayers for Site-Directed Ionic Self Assembly. Dissertation, Virginia Polytechnic Institute and State University, Blacksburg, 2008.

95. Sheffer, M.; Vivier, V.; Mandler, D., Self-assembled monolayers on Au microelectrodes. *Electrochemistry Communications* **2007,** 9, (12), 2827-2832.

96. Fleischmann, M.; Pons, S.; Daschbach, J., The a.c. impedance of spherical, cylindrical, disk, and ring microelectrodes. *Journal of Electroanalytical Chemistry and Interfacial Electrochemistry* **1991,** 317, (1-2), 1-26.

97. de Levie, R., Electrochemical Response of Porous and Rough Electrodes. In *Advances in Electrochemistry and Electrochemical Engineering*, Delahaye, P., Ed. Interscience: New York, 1967; Vol. VI, p 458.

98. Yang, D. F.; Morin, M., Chronoamperometric study of the reduction of chemisorbed thiols on Au(111). *Journal of Electroanalytical Chemistry* **1997,** 429, (1-2), 1-5.

99. Yang, D. F.; Morin, M., Chronoamperometric study of the reductive desorption of alkanethiol self-assembled monolayers. *Journal of Electroanalytical Chemistry* **1998,** 441, (1-2), 173-181.

100. Diao, P.; Jiang, D.; Cui, X.; Gu, D.; Tong, R.; Zhong, B., Studies of structural disorder of self-assembled thiol monolayers on gold by cyclic voltammetry and ac impedance. *Journal of Electroanalytical Chemistry* **1999,** 464, (1), 61-67.

101. Adamczyk, L. A.; Anderson, M. R., Impedance differences found with n-alkanethiol monolayers prepared by contact printing and solution adsorption. *Journal of Colloid and Interface Science* **2009,** In Press.

102. Sears, F. W.; Zemansky, M. W.; Young, H. G., *University Physics*. 7th ed.; Addison-Wesley: Reading, MA, 1987; p 1096.

103. Wilhelm, T.; Wittstock, G., Localised electrochemical desorption of gold alkanethiolate monolayers by means of scanning electrochemical microscopy (SECM). *Mikrochimica Acta* **2000,** 133, (1-4), 1-9.